PONTIFÍCIA UNIVERSIDADE CATÓLICA
DO RIO DE JANEIRO

Ana Carolina Constâncio Trindade

A study on the mixture design and mechanical performance of strain-hardening geopolymer composites (SHGC) under extreme conditions

Tese de Doutorado

Thesis presented to the Programa de Pós-Graduação em Engenharia Civil e Ambiental from the department of Engenharia Civil of PUC-Rio in partial fullfilments of the requirements for the degree of Doutor em Ciência – Engenharia Civil.

Advisor: Prof. Flávio de Andrade Silva

Rio de Janeiro
August 2021

PONTIFÍCIA UNIVERSIDADE CATÓLICA
DO RIO DE JANEIRO

Ana Carolina Constâncio Trindade

A study on the mixture design and mechanical performance of strain-hardening geopolymer composites (SHGC) under extreme conditions

Thesis presented to the Programa de Pós-Graduação em Engenharia Civil e Ambiental from the department of Engenharia Civil of PUC-Rio in partial fullfilments of the requirements for the degree of Doutor em Ciência – Engenharia Civil.

Prof. Flávio de Andrade Silva
Advisor
Civil and Environmental Eng. Dept. – PUC-Rio

Prof. Daniel Carlos Taissum Cardoso
Civil and Environmental Eng. Dept. – PUC-Rio

Prof. José Roberto Moraes d'Almeida
Chemical and Materials Eng. Dept. – PUC-Rio

Prof. Waltraud M. Kriven
Materials Science and Eng. Dept. – UIUC

Prof. Rafael Giuliano Pileggi
Civil Construction Eng. Dept. – USP

Rio de Janeiro, August 12th, 2021

Ana Carolina Constâncio Trindade

Undergrad in Civil Engineering at Universidade Católica de Petrópolis in 2013 and obtained her M.Sc. Degree in Civil Engineering from the Pontifícia Universidade Católica do Rio de Janeiro in 2017.

Bibliographic data

Trindade, Ana Carolina Constâncio

A study on the mixture design and mechanical performance of strain-hardening geopolymer composites (SHGC) under extreme conditions / Ana Carolina Constâncio Trindade ; advisor: Flávio de Andrade Silva. – 2021.

187 f. : il. color. ; 30 cm

Tese (doutorado)–Pontifícia Universidade Católica do Rio de Janeiro, Departamento de Engenharia Civil e Ambiental, 2021.

Inclui bibliografia

1. Engenharia Civil e Ambiental - Teses. 2. Geopolimeros. 3. Metacaulim. 4. Compósitos. 5. Fibras. 6. Impacto. I. Silva, Flávio de Andrade. II. Pontifícia Universidade Católica do Rio de Janeiro. Departamento de Engenharia Civil e Ambiental. III. Título.

CDD: 624

Acknowledgments

This study was financed in part by the Coordenação de Aperfeiçoamento de Pessoal de Nível Superior - Brasil (CAPES) - Finance Code 001, and also with the financial support of CNPq.

I here express my gratitude to Prof. Flávio de Andrade Silva, advisor of this research, for all his support during each step of this work. Thank you for encouraging my ideas, my individual scientific vision, and experiences. Through my participation in national and international conferences and working in partnership with other research groups in Brazil and abroad, I was able to acquire diverse experiences that today allow me to adapt to varied research methodologies, which is a result of the full support provided by Prof. Flavio. I am sure that this partnership will continue throughout my professional career.

This research was partially conducted at the Laboratory of Structures and Materials (LEM-DEC) at PUC-Rio, where I could count on the technical and always positive support of Euclides, José Nilson, Rogério, Jhansen, Bruno, and Anderson. They all spent a considerable amount of time helping me to assemble equipment, to purchase varied materials, teaching me a little bit of their functions, especially Euclides, who was a great teacher in the calibration and modification of testing setups. I also thank the encouragement of Prof. Daniel Cardoso, always available for questions in the laboratory since the beginning of my experimental work. In addition, I thank the support of all my lab colleagues, with whom I was able to share the achievements and anxieties during this journey. Fortunately, there are many of you, and you will always have a special place with me. I would like to write a special thank you to Daiana, Leticia, Raylane, Rebecca and Tathiana. Together we have discovered a world of scientific possibilities, celebrating the publication of our papers, finding support and motivation to continue when things were not going so well, knowing that we could always count on each other, no matter our geographic location. I am proud to say that you are now part of my family.

I would like to thank Prof. Waltraud M. Kriven for hosting me in her group at UIUC (USA) for a few months so that I could learn the basic chemistry involved in geopolymerization and other variations. It was an experience of great fundamental learning, which made it possible to carry out my doctoral research. Special thanks to Ph.D. students Kaushik Sankar, Gregory P. Kutyla, and Vimanyu Chadha.

Part of the experimental studies were conducted at TU Dresden (Germany), under the supervision of Prof. Viktor Mechtcherine, through the CAPES/DAAD project, allowing me to learn more about the SHCC technology from his team, and adapt it to geopolymer matrices, performing well-established tests in extreme conditions. Therefore, I am grateful for the technical-scientific support of the researchers Marco Liebscher and Iurie Curosu, and the members of the laboratory staff, especially Kai-Uwe Mehlisch, Tilo Günzel and Christian Stahn. I also thank the doctorate students Ali Heravi and Jitong Zhao for the joint research that we conducted from shared setups and ideas. A special thanks to doctorate student Renata Lorenzoni who shared this experience with me and who was my Brazilian support in Germany.

Other partnerships were made with Brazilian University groups, allowing the use of different equipment in varied chemical-experimental analyses. I thank Prof. José Adilson de Castro and Bonifácio de Oliveira, for carrying out the dilatometry tests at the Mechanical Engineering department at UFF campus in Volta Redonda. I also thank Prof. Roberto Avillez and Dr. Sonia Letichevsky for carrying out the XRD analysis in the Department of Chemical and Materials Engineering (DEQM) at PUC-Rio. Furthermore, I am grateful for the use of the microscopy techniques coordinated by Prof. Sidnei Parciornik, with the help of students Camila and Thalita, who are also members of the DEQM.

I would also like to thank the presence of the Professors members of this thesis committee, for their availability and careful reading of this study.

And finally, I dedicate this work to my parents, my siblings, and my love. You have all supported me unconditionally, and I am extremely grateful to have you in my life.

Abstract

Constâncio Trindade, Ana Carolina; de Andrade Silva, Flávio (Advisor). **A study on the mixture design and mechanical performance of strain-hardening geopolymer composites (SHGC) under extreme conditions.** Rio de Janeiro, 2021. 187 p. Tese de Doutorado – Departamento de Engenharia Civil e Ambiental, Pontifícia Universidade Católica do Rio de Janeiro.

Geopolymers possess a chemical plurality in their design that allow the achievement of varied properties depending on demand, both in terms of high-tech ceramic materials and development of constructive solutions. They are obtained from the combination of aluminosilicate precursors and alkaline solutions, with different hardening processes, depending on the curing conditions and chemical balance. In the hardened state, they present a fragile behavior, being then usually reinforced with fibers and aggregates aiming to improve their mechanical performance. As they are relatively new materials, there is a need to accurately assess their capacity under usual and extreme conditions to meet several specific market demands. Such extreme conditions include static and dynamic loading, as well as exposure to high temperatures, which are the major points of analysis in this study. For this, different precursors, such as metakaolin and fly ash, and alkaline solutions, based on sodium and potassium, were studied regarding rheology in the fresh state, and evolution of strength gain according to the curing process used. These were fundamental parameters in the selection of matrices able to achieve an adequate balance between fluidity and viscosity to incorporate 2% by volume of synthetic PVA and PE short fibers. The strain-hardening geopolymer composites (SHGC) were then characterized through typical mechanical tests, such as compression, flexural, tensile, pull-out, in quasi-static and impact loadings, and under regular and high temperature exposures (up to 200 ºC), being further analyzed through imaging and analytical procedures. In general, high reactivity metakaolin combined with Na-based alkaline solutions demonstrated a superior SHGC performance, with and without aggregate incorporation, reaching stress gains and multiple cracking formation when reinforced with both PVA and PE short fibers, the latter being responsible for greater mechanical efficiency when exposed to quasi-static and impact loading. This behavior, however, was not reiterated when exposed to high temperatures, with higher residual strength reductions due to the melting point of PE (at 150 ºC), opposed to an increased performance of PVA (240 ºC), being thus more effective at such extreme application. When compared to typical SHCC behavior, SHGC reached greater efficiency both mechanically and thermally, showing unprecedented results in impact loading, thus demonstrating varied application potential.

Keywords

Geopolymers; Metakaolin; Composites; Fibers; PVA; PE.

Resumo

Constâncio Trindade; Ana Carolina; de Andrade Silva, Flávio (Orientador). **Um estudo sobre a dosagem e o desempenho mecânico de compósitos geopoliméricos do tipo strain-hardening (SHGC) sob condições extremas.** Rio de Janeiro, 2021. 187 p. Tese de Doutorado - Departamento de Engenharia Civil, Pontifícia Universidade Católica do Rio de Janeiro.

Geopolímeros possuem uma pluralidade química em seu design que permite a obtenção de propriedades variadas dependendo da demanda, tanto em termos de materiais cerâmicos de alta tecnologia quanto no desenvolvimento de soluções construtivas. São obtidos a partir da combinação de precursores alumino silicatos e soluções alcalinas, com diferentes processos de endurecimento, dependendo das condições de cura e equilíbrio químico. No estado endurecido, apresentam um comportamento frágil, sendo geralmente reforçados com fibras e agregados na melhoria do desempenho mecânico. Por serem materiais relativamente novos, é necessário avaliar com precisão sua capacidade em condições usuais e extremas para atender a diversas demandas específicas do mercado. Tais condições incluem solicitações estáticas e dinâmicas, bem como a exposição a altas temperaturas, que são os principais pontos de análise deste estudo. Para isso, diferentes precursores, como metacaulim e cinzas volantes, e soluções alcalinas, à base de sódio e potássio, foram estudados quanto à reologia e ganho de resistência de acordo com o processo de cura utilizado. Esses foram parâmetros fundamentais na seleção de matrizes capazes de incorporar 2% em vol. de fibras curtas de PVA e PE sintéticas. Os compósitos do tipo *strain-hardening* (SHGC) foram então caracterizados através de ensaios mecânicos típicos, tais como compressão, flexão, tração, arrancamento, em carregamentos estáticos e dinâmicos, e sob exposições regulares e de alta temperatura (até 200 ºC), sendo analisados posteriormente por meio de procedimentos típicos analíticos e de imagem. No geral, a combinação de metacaulim de alta reatividade com soluções alcalinas a base de sódio apresentou melhores performances em SHGC, com e sem a incorporação de agregados, atingindo ganhos de resistência e múltipla fissuração quando reforçado com ambas as fibras curtas de PVA e PE, sendo a última responsável pela maior efetividade mecânica do compósito quando exposto a carregamento quase-estáticos em de impacto. Esse comportamento, no entanto, não se repetiu ao ser exposto a temperaturas elevadas, com maiores reduções na resistência residual devido ao ponto de fusão do PE (150 ºC), em comparação a um maior valor para PVA (240 ºC), sendo então este mais efetivo em aplicações extremas deste tipo. Quando comparado a comportamentos típicos de SHCC, SHGC demonstrou uma maior eficiência tanto mecânica quanto térmica, apresentando resultados inéditos em carregamentos de impacto, gerando assim uma enorme quantidade de aplicações potenciais.

Palavras – chave

Geopolímeros; Metacaulim; Compósitos; Fibras; PVA; PE.

Table of contents

List of figures

List of tables

1 Introduction

1.1. Motivation

Geopolymer materials have been increasingly explored in the civil construction field for the last decades, due to their sustainable properties and comparable-to-concrete mechanical efficiency. Amid the urban pollution and its unstoppable growth since the 19th century, it is necessary to evaluate new green-friendly materials that may be able to partially replace the conventional consumption, since Portland cement production is responsible for at least 5% of the carbon emissions in the atmosphere [1].

However, for decades, geopolymer related studies were mainly focused on its chemical development for high-tech ceramics and use as refractory material [2,3]. Despite enormous advances, distinctions on the use of different precursors and activators, as well as uncomplicated production processes appear as major challenges to be demystified. More recently, advances in the fiber-reinforced composite materials field brought attention to the geopolymer use, mainly due to distinct interfacial mechanisms [4] and benefits related to the structure's durability [5]. Varied types of fibers have been used so far, into several matrix combinations, with major emphasis on their quasi-static behavior under regular temperature conditions. Their dynamic efficiency and their use under degrading environments remain little explored.

Thus, this research aims to fill in some of these knowledge gaps, designing strain hardening geopolymer composites (SHGC) capable of bearing both quasi-static and dynamic loading, in addition to predict their degradation mechanisms under thermal exposures.

1.2. Goals

This research aims to develop and characterize geopolymer composites that may present high mechanical and durability performance under distinct solicitations (static and dynamic) and materials combinations (precursors and fibers). The geopolymer matrix characterization was performed, followed by the manufacturing and evaluation of strain-hardening geopolymer composites (SHGC) reinforced with synthetic short fibers (PVA and PE) under quasi-static and dynamic loading regimes, followed by a thermal durability analysis, where the composites were exposed to elevated temperatures, allowing newfound results to be presented.

1.3. Thesis organization

The thesis is composed of this introduction, a literature review, followed by four chapters structured as individual full papers, conclusions, and future work suggestions. The literature review presents an overview of the geopolymers synthesis, properties, its use and effectivity in composites manufacturing, and previous studies on thermal durability. At this point, the knowledge gap is highlighted showing the importance of this research. Thereafter, four papers are presented in individual chapters, some of which have already been published in indexed international journals, while the others are under review for publication. Each paper deals with a specific geopolymer property, presenting the methodologies used and the results obtained in each experimental study, in the following order:

- Chapter 3: Influence of precursor materials on the rheological and thermo-chemo-mechanical properties of sodium-based geopolymers.
- Chapter 4: Mechanical behavior of K- and Na-based, strain-hardening geopolymer composites (SHGC) reinforced with PVA fibers [6].
- Chapter 5: Tensile behavior of strain-hardening geopolymer composites (SHGC) under impact loading [7].
- Chapter 6: Influence of elevated temperatures on the residual and quasi in-situ flexural strength of strain-hardening geopolymer composites (SHGC) reinforced with PVA and PE fibers.

A conclusion with the most relevant results of the papers is presented in the last chapter, followed by future works suggestions.

1.4. References

[1] Chen, C., Habert, G., Bouzidi, Y., & Jullien, A. (2010). Environmental impact of cement production: detail of the different processes and cement plant variability evaluation. Journal of Cleaner Production, 18(5), 478-485.

[2] Davidovits, J. (2002, October). years of successes and failures in geopolymer applications. Market trends and potential breakthroughs. In Geopolymer 2002 conference (Vol. 28, p. 29). Saint-Quentin, France; Melbourne, Australia: Geopolymer Institute.

[2,3] Kriven, W. M., Bell, J., & Gordon, M. (2004, January). Geopolymer Refractories for the Glass Manufacturing Industry. In Ceramic Engineering and Science Proceedings (Vol. 25, No. 1, pp. 57-79).

[4] Trindade, A. C. C., Borges, P. H. R., & de Andrade Silva, F. (2019). Evaluation of Fiber–Matrix Bond in the Mechanical Behavior of Geopolymer Composites Reinforced with Natural Fibers. Advances in Civil Engineering Materials, 8(3), 361-375.

[5] Trindade, A. C. C., Alcamand, H. A., Borges, P. H. R., & Silva, F. A. (2017). On the durability behavior of natural fiber reinforced geopolymers. Ceramic and Science Proceedings, 38(3), 215-228.

[6] Trindade, A. C. C., Curosu, I., Liebscher, M., Mechtcherine, V., & de Andrade Silva, F. (2020). On the mechanical performance of K-and Na-based strain-hardening geopolymer composites (SHGC) reinforced with PVA fibers. Construction and Building Materials, 248, 118558.

[7] Trindade, A. C. C., Heravi, A. A., Curosu, I., Liebscher, M., de Andrade Silva, F., & Mechtcherine, V. (2020). Tensile behavior of strain-hardening geopolymer composites (SHGC) under impact loading. Cement and Concrete Composites, 113, 103703.

2 Literature review

2.1. An overview on geopolymers

2.1.1. Introduction

The search for innovative materials has always been an important aspect of the evolution of our society. In the beginning, it was a matter of survival. Then it became a crucial factor in knowledge spreading and development of modern solutions. Nowadays, the environmental issue has been attracting more attention, resulting in a demand for new constructive green-friendly materials. Geopolymers appear for quite some time as an interesting solution, capable of reaching similar or even superior properties to that of conventional cementitious materials, despite presenting manufacturing challenges that can compromise their use on a large scale, thus being subject to specific market applications.

The studies with geopolymers initiated with Prof. Joseph Davidovits [1,2] in the ’70s in France. His team developed research in the ceramic field intending to produce a suitable material to withstand the increasing occurrence of fires in the country at the time. The inorganic geopolymer showed enormous potential when exposed to elevated temperatures [1,3,4] allowing it great visibility. The number of papers related to the subject has been increasing gradually since then [5-8], due to a variety of characteristics that may be achieved according to modifications in its formulations and incorporation of reinforcements (particulate and fibers). The primary areas of application of this material in civil construction are related to the development of precast elements, pavements, and repair technology [2]; and in minor scale to auto-nailed cellular concrete, encapsulation of chemicals and nuclear waste [2], thermal protection in natural-based materials [9], and monolithic refractories [7].

Geopolymers are a class of inorganic, pervious, amorphous, nanoparticulate, and nano porous structures, where the precursor materials are exclusively highly coordinated aluminosilicates [10]. In general, geopolymers can be obtained by different combinations, being the most common ones based on metakaolin and fly ash, soluble in high pH potassium or sodium-based solutions [11]. The raw materials, molar ratios, and processing conditions are critical points on the mechanical, physical, and chemical properties of the final product [8,11]. The water content and the curing regime may also contribute to its variations [2,8].

Geopolymers present the typical characteristics of ceramic materials in general, with low tensile strength and low deformation capacity [11]. Although exhibiting higher deformability in its pure form when compared to cementitious sources [12], geopolymers are still brittle, reaching maximum Young's modulus of 14 GPa [13]. Reinforcements of varied sizes, morphologies, and arrangements [14-18] can be incorporated into these matrices, similar to the processes performed with cementitious binders, to increase its ductility and even ultimate strength [2] in both static and dynamic loading. Throughout this review some of the particularities on geopolymer binders and their composites will be discussed, as well as the main modern research on the topic.

2.1.2. History and terminology

Varied structural materials used in ancient constructions have proven to be extremely durable, mostly due to their mineral and pozzolanic origin, being thus the historical precursors of both Portland-cement and geopolymer manufacturing technologies [12,13]. Ancient communities, such as Greeks and Romans, used ceramic materials based on lime and pozzolans, such as volcanic ash and clay, to build their giant structures [2] in a time where knowledge was not so intensely disseminated. However, only many centuries later, in the 1940s, the German researcher Purdon produced the first scientific evidence regarding the use of alkali solutions in the hardening process of ceramic materials [2,3]. His team measured the reactivity of slag and analyzed its mechanical behavior using potassium and sodium hydroxide solutions, reaching compressive strengths of 25 MPa [14]. In the 1950s, the researchers Glukhovsky [15] and Krivenko [4] began to develop the so-called "alkali-activated materials" due to the shortage of Portland cement in East Europe, as a consequence of the war. Glukhovsky [15] found that he could replicate the natural process of transforming volcanic rocks into zeolites to obtain suitable building products. He studied mortars developed by Egyptians and Romans and then developed his material, based on aluminosilicate slags, called "soil cement", also known as a Me_2O-MeO-Me_2O_3-SiO_2-H_2O system [3].

Two decades later, the researcher Joseph Davidovits [1] introduced the concept behind his main work, based on inorganic stable aluminosilicate polymers, due to the catastrophic fires that occurred in France during that period. The goal was to develop a material capable of withstanding elevated temperatures while maintaining a suitable mechanical performance [10]. Throughout the process, Davidovits and his team [1] faced the theories related to the application of aluminosilicates in ancient societies and developed several types of research relating such theories to the recent developments of the material [13,16]. His team developed a fabrication method based on geosynthesis to obtain high-performance materials by the reaction of pure aluminosilicates in a stable alkaline environment [17,18]. He was the first to describe this class of materials as "geopolymers" [19]. The polymer-like network consists of SiO_4 and AlO_4 tetrahedra linked alternately in a range from amorphous to semi-crystalline [19], requiring positive ions to balance the negativity of Al^{3+} in IV-fold coordination [17,19]. Its empirical formula can be described as $M_2O \bullet Al_2O_3 \bullet xSiO_2 \bullet 11H_2O$, where M = Na, K, or Cs; and x represents the Si/Al ratio used [19]. Although generally specified as a subclass of alkali-activated materials due to their similarities, geopolymers require distinct mixing and reaction processes [7,19-21]. Throughout this text, only the term "geopolymer" will be used, and the differences between alkali-activation and geopolymerization will be explored.

Since the 1990s, several researchers around the world began to demystify geopolymer reactions and kinetics. Palomo [5,6] in Spain, Rahier [22] in Belgium, the group of the University of Melbourne-Australia [3], Kriven in Illinois-USA [7], besides Davidovits [2] himself in France, can be presented as pioneers in this development. Pacheco-Torgal in Portugal [20], Van Riessen at Curtin University [2], and Sanjayan at Swinburne University [12] (both in Australia) are also leading important research groups.

In Brazil, geopolymer research was first explored by the researcher Thaumaturgo [23] in 1999 at IME (Military Engineering Institute), allowing greater visibility to this technology in the country. Nowadays, several groups have explored the material in distinct manners, such as Borges at CEFET-MG [8]; Kirchheim at Federal University of Rio Grande do Sul, in collaboration with Provis [24]; Ribeiro at National Institute for Amazonian Research, in collaboration with Kriven [17,18]; and Silva, at PUC-Rio, in collaboration with Kriven [13,17,18], with each research group focusing on different applications that may contribute to a greater understanding and dissemination of this technology.

2.2. Geopolymer synthesis and processing

2.2.1. Geopolymerization

Geopolymers are produced by mixing an aluminosilicate source with amorphous silica dissolved in alkaline solutions (MOH), where M corresponds to the alkali cation used in the mixture (Na, K or even Cs) [1,2]. They can be fabricated through the combination shown in Figure 2.1, for example [2].

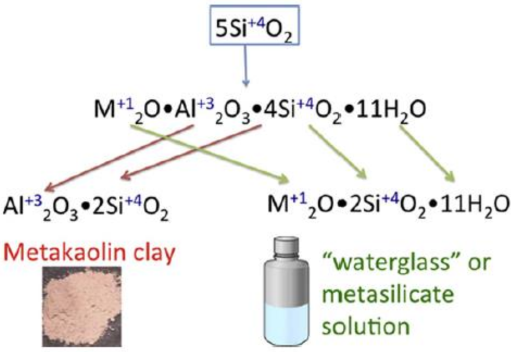

Figure 2.1 – Schematic synthesis of a metakaolin based geopolymer [2].

The raw material is chosen, in this case a crystalline clay ($Al_2O_3 \cdot 2SiO_2 \cdot 2H_2O$), that is previously heated for 1 hour at 700ºC, forming the amorphous powdered metakaolin ($Al_2O_3 \cdot 2SiO_2$). The alkali solution, or "water glass", containing NaOH or KOH, is dissolved in yH_2O, to which is added $xSiO_2$. This class of materials is centered on the following chemical balance: $M_2O \cdot Al_2O_3 \cdot xSiO_2 \cdot yH_2O$; where x = 2-6, and y = 7-13, depending mainly on the aluminosilicate particle size, specific surface area, and alkali concentration [1,2,3]. The amount of water is controlled due to porosity issues, that may compromise its final mechanical performance and durability [2,3,4].

During the geopolymerization process, the mixtures undergo (i) dissolution of the aluminosilicate source, (ii) polycondensation, and (iii) precipitation under ambient or high temperature [1,2,3]. The essence of this process is due to the highly strained AlO_5^{-2} coordination polyhedral in the amorphous metakaolin, forming a double bond with one Al atom, being susceptible to dissolution by the "water glass" [2], where the Al^{3+} forms the AlO_4^- tetrahedra. These attract charge-balancing group I cations, reacting with SiO_2 tetrahedra to form the amorphous 3D network, presented in Figure 2.2 [2].

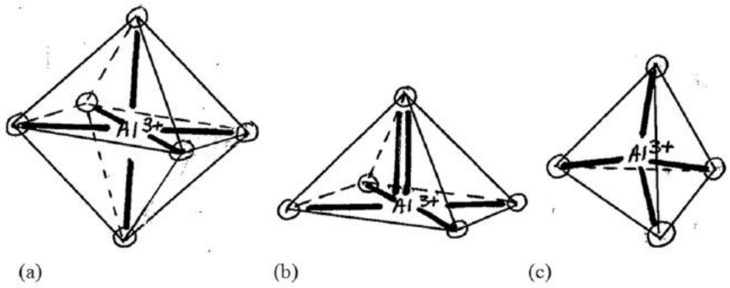

Figure 2.2 – (a) Crystalline kaolinite decomposes into (b) amorphous metakaolin after being treated for 1 hour at 700ºC, arising as a (c) stable geopolymer in presence of soluble alkali [2].

The amorphous atomic structure contains SiO_2 and AlO_4^- corner-shared, tetrahedral units, as presented in Figure 2.3. Its microstructure is usually nanoparticulate (~20-40 nm) and nano porous (~6.8 nm in diameter) [1,4]. The mixture process comprises the following steps: (i) powder and liquid are mixed under high shear (to obtain a highly reacted mixture); (ii) the fresh mix is poured into a plastic mold and covered to prevent early dehydration (the water entrapped in the nanopores results in great extents of pressure); (iii) the mix is left to set at room temperature, or curing at moderate temperatures (used to guarantee a faster reaction) [1, 2]. To properly define the chemistry in the process of geopolymerization, Davidovits [1] established a specific terminology to categorize the different classes of inorganic polymers based on distinct Si/Al ratios.

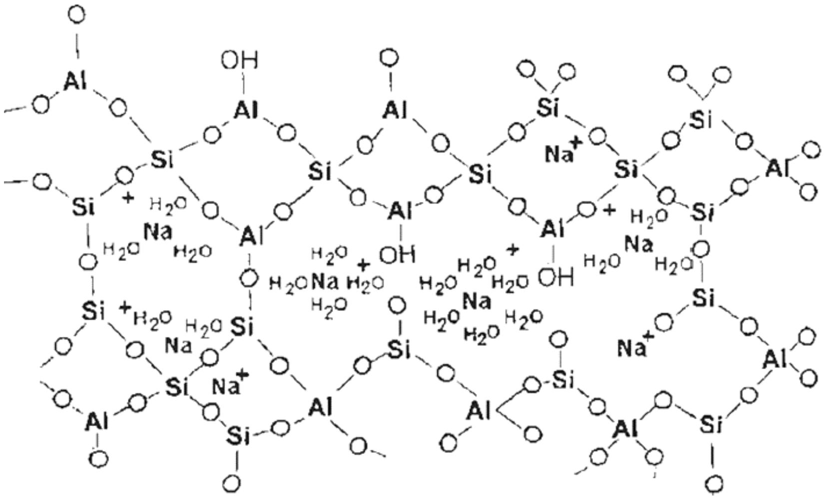

Figure 2.3 – Atomic model of a Na-based geopolymer structure [1].

For the designation of geopolymers based on aluminates and silicates, he suggested the term “poly(sialate)” [25], representing an abbreviation for silicon-oxo-aluminate. He [1,25] also mentioned that the amorphous to semi-crystalline Si-Al structures can be divided into four types, which are presented in Figure 2.4, produced for different applications. Low Si/Al ratios are presented as useful for brick ceramics (rigid), and fire protection, while higher ratios (3-4), are used to produce high tech geopolymer materials (stable, more flexible, and nano porous) [1,2].

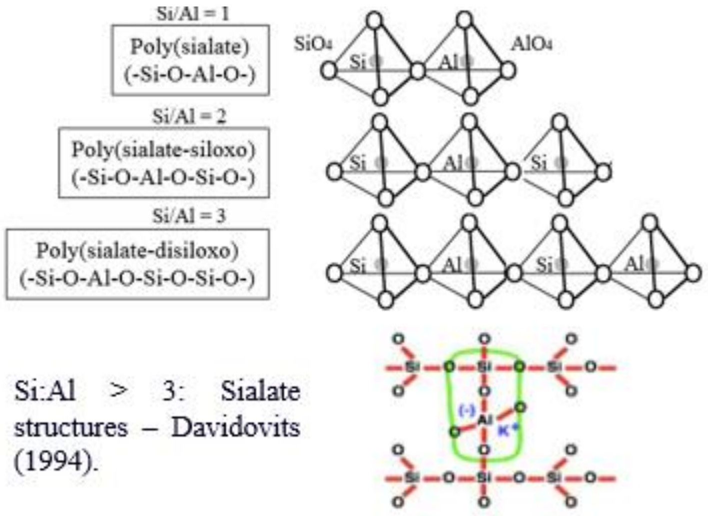

Figure 2.4 – Distinct sialate structures proposed by Davidovits [25].

2.2.2. Aluminosilicate sources

Several aluminosilicate sources can be used as raw materials, single or combined, in the manufacture of geopolymers, being the most commonly ones based on the synthesis of metakaolin (obtained through clay calcination processes), and fly ash (byproduct of coal combustion). The materials properties, such as strength and hardening characteristics, supply, demand, and cost are the main parameters to be considered in the geopolymer design. The global metakaolin production is approximately 37 million metric tons/year, with top producers in US, China, India and Germany, while fly ash production is approximately 2.8 billion metric tons/year, with top producers in China, India, US, and Russia [26]. The increased availability of fly ash makes this a cheaper precursor, even though reaching different properties when synthesized.

Metakaolin (calcined clay) presents an amorphous structure with a high-water demand in geopolymer production [3]. It is a complex material, resulting from the calcination of kaolinite clay at high temperatures, and consisting of alternating layers of silicates and aluminates, that may present at some point crystallinity disorder (amorphous material) [2]. The chemical and physical characteristics of different metakaolin (MK) sources may vary greatly, as presented in Table 1, as well as their particle size, crystallinity, and presence of impurities [3], due to distinct compositions in varied regions of the world. HP *Metacaulim do Brasil*, for example, presents higher iron oxide (Fe_2O_3) contents, when compared to all the other variations, being dominant in the color determination and mechanical evolution of the final material. MK-ZK_2 has a high content of silicon dioxide (SiO_2), thus being an influential factor in the SiO_2 demand in the WG (water glass), modifying the rheology and hardening process of its geopolymer. Such chemical differences may also be dominant in the degradation processes under several environments. The formulations and chemical structures described previously in the geopolymerization synthesis section were mostly established based on well-reacted and stable metakaolin’s, with proportions similar to that of *Metamax* in Table 2.1.

The microstructure of geopolymers based on metakaolin has been well explored by several researchers in the last decades [7,8,10,13]. The mechanical capacity of the final material depends mainly on its morphology, chemical composition, alkali ratios, and formation of a nanoporous and nanoparticulate network (determinant in durability) [8,10,13]. The porosity of the MK-based geopolymers remains under discussion, due to relative complications in obtaining reliable data on such a complex material through the widely known techniques available. However, it is possible to observe in SEM and TEM analyzes (Figure 2.5) the nanoparticulate nature of the MK-based geopolymer (Metamax), which on a macroscopic level is impervious and structurally robust [2,13]. Metakaolin's are also commonly used as supplementary materials in Portland cement concrete mixtures up to 20% in weight, mostly due to its higher reactivity, when compared to other pozzolan sources [26].

Table 2.1 – Variability of chemical composition of distinct metakaolin precursors.

Composition [%]	Country	SiO_2	Al_2O_3	Fe_2O_3	K_2O	Other oxides	Source
HP Metacaulim do Brasil	Brazil	51.57	40.50	2.80	0.18	4.95	[27]
Metamax BASF	Germany	53.00	43.80	0.43	0.19	2.58	[7]
MKA76	Brazil	67.80	29.60	0.70	0.24	1.66	[28]
Mefisto K05	Czech Republic	55.01	40.94	0.55	0.60	2.90	[29]
MK-ZK_2	Iran	73.00	14.50	0.70	0.20	11.6	[30]

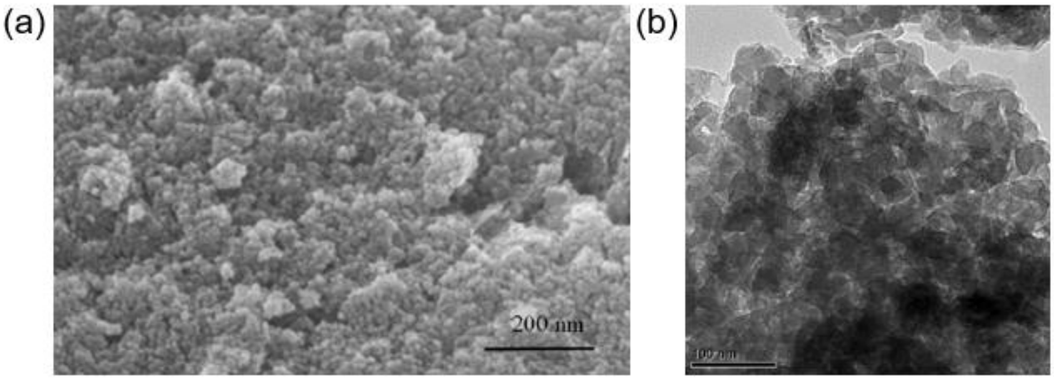

Figure 2.5 – (a) SEM and (b) TEM of a fully reacted region of geopolymer showing its nanoparticulate microstructure [2,3].

For geopolymerization, fly ash class F is preferred than calcium containing variations, since it can modify the geopolymer microstructure [31]. The precursor is obtained during the burning of coal in electrical production, consisting mostly of silt and clay-sized glassy spheres [26], being a risk to human health, thus increasingly used in civil construction. Its chemical composition depends mainly on the mineral composition of the coal gangue, presenting enormous variability, as shown in Table 2.2. It is mostly an aluminosilicate, with varied iron contents and alkalis. The higher the SiO_2/Al_2O_3, the slower it is the reaction, leading to an increasing curing period [33]. As raw material in geopolymer synthesis, it presents a great feasibility [2,3,10], despite reaching important structural differences from the metakaolin-based ones, due to its chemical and physical properties. Geopolymers based on fly ash require water/binder ratios much smaller than the ones indicated by the previous system, related to the difference in particle morphologies and water absorption, thus reducing the permeability of the system [2,3]. Their hardening period depending on each precursor variation and their rheology is yet to be completely understood.

Table 2.2 – Variability of chemical composition of distinct fly ash precursors.

Composition [%]	Country	SiO_2	Al_2O_3	Fe_2O_3	K_2O	Other oxides	Source
Fly ash F	Czech Republic	53.79	32.97	5.51	1.76	5.97	[32]
Fly ash F - Gladstone	Australia	47.87	28.0	14.09	0.62	9.42	[33]
Fly ash F - Tarong	Australia	75.66	19.0	1.38	0.63	3.33	[33]

Alternative precursors have also been widely evaluated in literature, such as silica fume [34], red mud and rice husk-ash [35], illite clay [36], and blast furnace slag [37]. The latter, however, results in a microstructure differentiated from traditional geopolymers [1,2], being thus classified as alkali activated, resulting in varied mechanical properties. This occurs due to the joint presence of calcium silicate hydrate (Ca-A-S-H), potassium aluminate hydrate (K-A-S-H), or sodium aluminosilicate hydrate (N-A-S-H) phases, similar to the hydration products in cement [2,3]. The main difference between alkali-activated materials and geopolymers is that the first group corresponds to hydrated, crystalline precipitates, while geopolymers are amorphous, inorganic polymeric precipitates that contain a minimum amount of chemically bound H_2O other than the entrapped water [2,3]. In the 1950s, Glukhovsky [38] proposed a theoretical model for alkali activation. In the last decades, several researchers have been working on the development of more precise theories that could reflect the entire process [3,7,24]. However, a great number of published papers of the “geopolymer community” refer to alkali-activated materials as geopolymers, causing great confusion in the field.

Therefore, to obtain geopolymers with elevated mechanical properties, and still present environmental and durability advantages, compatibilization of such mixtures must exist.

2.2.3. Alkali solutions

The geopolymer dissolution media is predominantly comprised of sodium (Na) and/or potassium (K) hydroxides and/or silicates [2,13]. In general, alkali hydroxides and silicates at pH greater than 10 are required for geopolymer synthesis [39]. The most important properties to be considered in the use of hydroxides as activators are (i) high corrosivity; (ii) viscosity; and (iii) heat of dissolution [3]. NaOH appears as the most common activator used in geopolymer synthesis since it presents a wide availability and low costs [2,3]. Its use also provides the formation of zeolitic-like structures, mostly after extended periods of curing [3,10]. This mechanism also occurs for KOH activators, although its crystallization occurs more slowly [10, 39], which may be dependent on the curing regime (use of temperature). Nevertheless, its corrosive nature may induce difficulties in future large-scale processing [3]. However, they present lower viscosity and demonstrate greater stability through the geopolymerization process [2,10].

Alkali solutions formed by combinations of silicates and hydroxides are also common since they result in the exploitation of both characteristics in the synthesis of aluminosilicates materials and demonstrate a lower cost demand [8,13,18,40]. More recently, anhydrous metasilicates [41,42] and the use of acidic medium (phosphoric acid) [43] have been proposed to be used in the geopolymer synthesis, as a new generation of geopolymers, reaching suitable mechanical performances, with durable long term and thermal responses yet to be understood.

2.2.4. Processing conditions

As evidenced previously, geopolymers usually appear as an amorphous ceramic material. However, some authors have noted the formation of semi-crystalline phases on several occasions [1,25,44]. These crystalline phases are generally zeolitic and are more predominant when synthesis is carried out under hydrothermal environments with 50 wt% of water, depending on the reaction conditions [44]. Although the speciation of silicate and aluminate is largely determined by the concentration of alkali, temperature of dissolution, and Si/Al ratio, the process of dilution also allows an improved solution-phase transport and reorganization [45]. Several studies also imply that the synthesis temperature and aging are critical in determining the structure of the reaction products [45]. An increase in synthesis temperature can improve the ordering mechanisms in geopolymer binders [7]. The higher the temperature, the greater the strength development in the early ages, due to a faster dissolution, by enhancing the reactivity of the particles, up to a limit of 100 ºC [7,45]. It is worth noticing, however, that the curing temperature must not reach the H_2O evaporation range (100 ºC), since it may result in early dehydration issues [46]. As previously discussed, geopolymers are nano porous, meaning that when a water loss occurs, it tends to create internal pressures that can lead to undesired crack formation. The use of plastic packaging has shown to be effective in keeping water loss under control, even at curing regimes exposed to temperature. Furthermore, it is important to carefully choose the material used in mold manufacturing since geopolymer matrices demonstrate an enhanced adhesion on metals [47]. Therefore, for proper demolding, polymeric parts are considered more suitable.

2.3. Geopolymer composites

2.3.1. Overview and historical perspective

The incorporation of reinforcements in ceramic mixtures, such as cementitious and geopolymer binders, may present mechanical favorable modifications. Ceramic materials are typically characterized by low tensile strength and low deformation capacities [11]. Although exhibiting greater results in its pure form when compared to cementitious materials [12], geopolymers are still brittle. Reinforcements of varied sizes and morphologies can be incorporated into these matrices to overcome this issue [2]. Such modifications can result in gains in tensile strength, ductility, toughness, and even durability [48]. For example, particulate reinforcements, such as chamotte and sand, when incorporated with adequate particle sizes, appear as suitable modifications due to the additional difficulty presented by cracking formation and propagation in the microstructure of the material, as presented in Figure 2.6 [2].

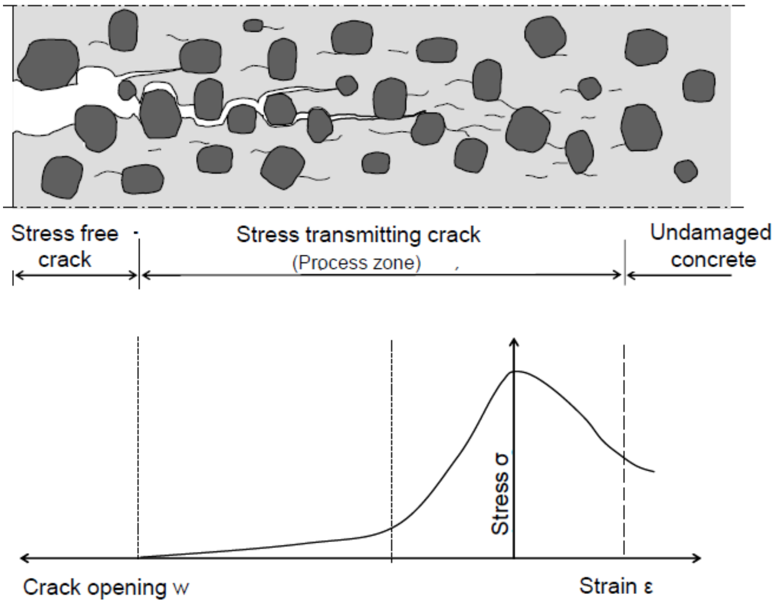

Figure 2.6 – Crack propagation in a brittle material reinforced with particulate reinforcement [2].

The incorporation of reinforcements into brittle matrices go back to ancient times, with the use of straws and reeds in bricks, and also animal hair in plaster [3,4]. Approximately 3,500 years ago, sunbaked bricks were reinforced with straws in the construction of a 57.0 m tall hill in Baghdad [48]. The most widely used composite in modern times, developed in the 1900s, was the asbestos cement [49]. In recent times, several types of fibers have been incorporated into cementitious and geopolymer matrices [2,3,48]. Conventional steel and glass fibers were used in early studies developed in the 1950s [50] and remain to this day as viable and widely manufactured solutions. Synthetic fibers, such as carbon, kevlar, and polypropylene were developed more recently, as new high-performance alternatives in ceramic composites [16]. Natural fibers, such as jute, sisal, and *curauá*, are being pointed out as green-friendly solutions [51-53] with high mechanical potential.

Recent studies demonstrate great improvements in the mechanical behavior of fiber-reinforced materials reinforced with high-performance short synthetic fibers, such as short polyvinyl alcohol (PVA) [54] and polyethylene (PE) [55]. It is interesting, however, to notice that despite presenting distinct microstructural properties, it is possible to correlate the mechanisms related to adhesion and stress development of geopolymer and cementitious composite materials.

2.3.2. Particulate reinforcements

Particulate reinforcements have been added to geopolymers to act as fine aggregates, fillers, or to provide high-temperature strength. The first two functions result in the microstructural development of the fine-grained ceramics, reaching improvements in strength and toughness through the addition of chemically and morphologically compatible particles [56]. In general, for geopolymer binders, it was found that most of the studies containing particulate reinforcements use fine river or artificial sand, as occurs for cementitious binders, providing enough adhesion to the system. The third function is related to the thermal compatibility of both matrix and particles, where refractory, alumina-based and glass particles are mostly used, resulting in enhanced volumetric stability during the geopolymer phase changes at high temperatures [57]. Also, dolomite [58], bone ash [59], and fine glass [60] have been recently explored, melting after reaching 1000 ºC and flowing into the cracks caused by dehydration, acting as a type of synthetic crack healing method, showing thus a trending application for the particulate reinforcements.

2.3.3. Fiber reinforcements

From a historical point of view, it is possible to affirm that the reinforcement of ceramic matrices has always been largely carried out through continuous metal bars, in favorable arrangements to increase its mechanical behavior [48].

Alternative classes of reinforcements, however, may present different morphologies, arrangements, physical, chemical, and mechanical properties [3]. Table 2.3 presents the mechanical characteristics of different fibers, in addition to the brittle behavior of both representative matrices already mentioned previously, cement- and geopolymer-based. It is possible to notice small distinctions regarding their mechanical behavior. Geopolymers may present greater values of strength, lower modulus of elasticity, and greater capacity of deformation [61]. However, it still presents a brittle behavior, and the incorporation of fibers appears to be as a useful solution as occurs for cement binders.

Table 2.3 – Mechanical properties of geopolymer and cementitious materials, and various types of fibers.

Material	Tensile strength (MPa)	Young's modulus (GPa)	Elongation at break (%)	Source
Geopolymer matrix	2.17	12.23	0.020	[61]
Cement matrix	1.66	17.26	0.012	[51]
Steel	1500	200	3.5	[49]
Glass	3,500	76	4.0	[49]
Carbon	4000	380	1.5	[49]
Aramid	3400	74	4.5	[49]
PVA	1600	41	6.0	[54]
PE	2500	80	3.5	[55]
PBO	5800	270	2.4	[62]
Jute	104	5.68	2.1	[61]
Sisal	392	10.4	3.8	[51]
Curauá	1250	27.8	4.3	[53]

The reinforcement types indicated in this Table demonstrate a great variability in mechanical capacities, since they may be presented in different forms, arrangements, chemical, and physical compositions. Two classifications should be considered in advance: (i) the shape of the fibers individually; and (ii) its dispersion into the matrix [63]. Regarding their form, they can be distinguished in two groups:

(i.a) discrete monofilaments (i.e. steel); and (i.b) bundles of filaments (i.e. glass, jute, and carbon) [64]. As for its array: (ii.a) discrete short fibers (i.e. steel); (ii.b) continuous reinforcement in the form of long fibers (i.e. sisal); and (ii.c) 2D and 3D arrangements (i.e. jute, carbon). Figure 2.7 presents a classification of shape and dispersion of fibers. This variability allows the creation of a range of potential applications, to improve not only the mechanical capacity of its incorporating materials, but also their durability and functionality, i.e., short fiber reinforcement may contribute to reduce the crack widths in multiple cracking formation during damage, avoiding the penetration of degrading agents.

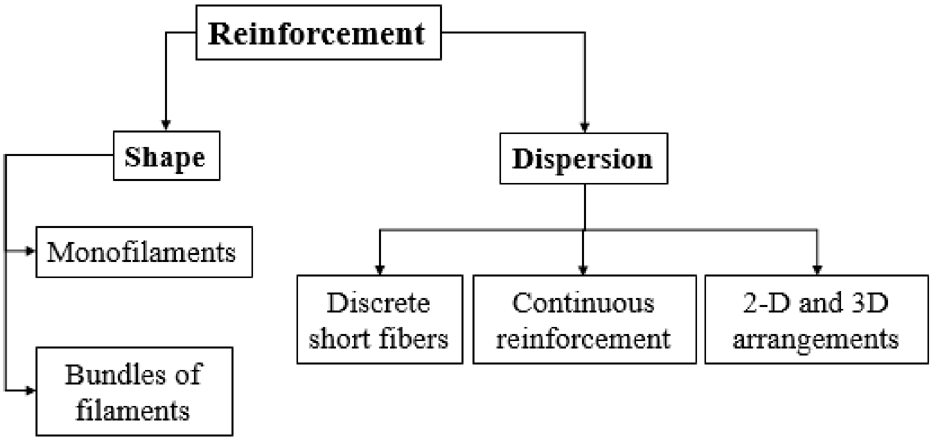

Figure 2.7 – Classification regarding shape and dispersion of fibers.

2.3.4. Mechanical analysis

The effect of fiber incorporation on fragile ceramic matrices can be distinguished in two levels: micro and macrostructural [65]. The first one corresponds to the stage just after the culmination of the elastic phase, where micro cracks begin to form in the matrix [2,66]. As the load increases, the length of microcracks also increases, creating coalescence and they finally become macro-cracks [39,66]. Depending on the volume fraction of fibers incorporated into the matrix, justified by a minimum size, they tend to cross the microcracks, restricting their propagation into the matrix [39,67]. To obtain an effective behavior, Naaman [50] suggests that fibers must present the following properties: (i) tensile strength at least 2/3 times greater than the one presented by the matrix; (ii) bond strength of the same order or higher than the tensile strength of the matrix; (iii) elastic modulus higher than the one presented by the matrix.

A typical mechanical analysis of a fiber-reinforced ceramic material (FRCM) can be performed through distribution in 5 different zones of loading [61,65], as presented in Figure 2.8. Zone I correspond to the elastic phase, where both matrix and fiber behave linearly. Due to low fractions of fibers, the stiffness of the composite is governed by the matrix properties. This zone exhibits the greatest stiffness. Then it is interrupted by the formation of the first crack, or the so-called bending over point (BOP). At the end of zone I, no crack completely crosses the thickness of the composite, opposite to the end of zone II. Immediately after the appearance of other cracks, they begin to propagate in a distributed manner in Zone III. As the deformation increases, more cracks are formed and the spacing between them decreases. Zone IV corresponds to the end of the cracking phase and the beginning of the detachment/pulling out of the fibers. As the crack opening becomes saturated, progressive damage occurs. The post-peak behavior takes place in zone V, where residual stresses are identified.

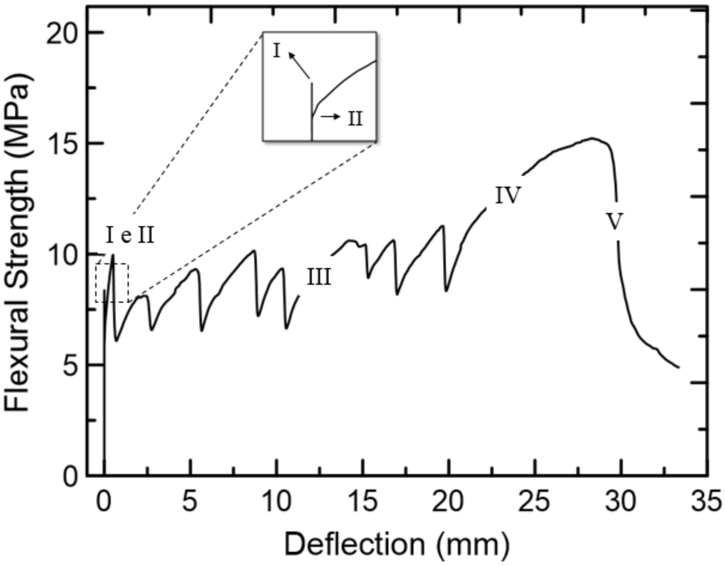

Figure 2.8 – Cracking mechanisms of jute fiber-reinforced composites [61].

Superior mechanical behavior can be achieved by using specific processes, as fiber treatments and coatings [2,3,39]. The fiber-matrix interactions interfere in the effectiveness of the material [39] and can be distinguished into three categories: (i) physical and chemical adhesion; (ii) frictional adhesion; and (iii) mechanical anchorage. The chemical composition of the fiber contributes not only to the adhesion but also to adsorption [39,41]. Figure 2.9 presents a classical pull-out debonding behavior [61]. The mechanisms occur in three regions, based on levels of distribution of shear stresses in the fiber. Region I correspond to the elastic phase, with increased load at a high rate. With the increase of load, at a certain point in the curve, the response becomes non-linear (region II), defining the initial range of fiber decohesion [61]. The maximum peak occurs in region II, under conditions of partial decohesion, where the pull-out force reaches its maximum value (P_{max}). Then, in region III, gradual detachment occurs until complete loss of adhesion.

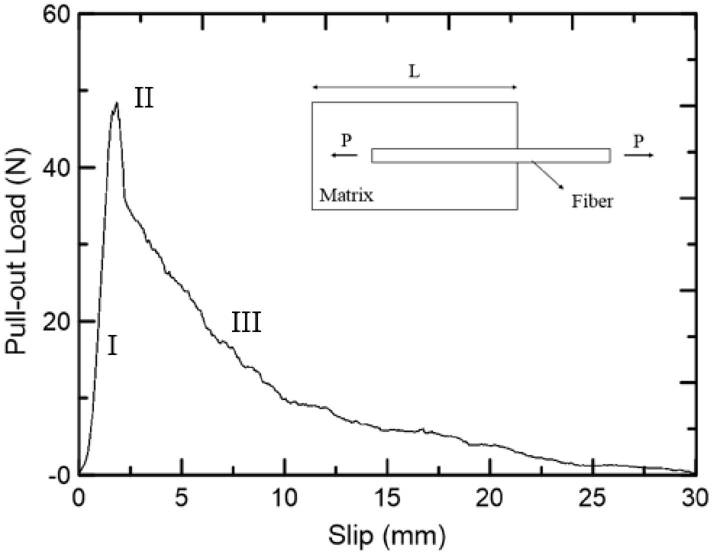

Figure 2.9 – Pull-out debonding mechanisms [66].

Results found in literature present a variety of mechanical responses regarding types of reinforcements. Ahmed *et al.* [67] observed that the use of hybrid short fibers reinforcements (steel and polypropylene) significantly improved tensile and flexural strengths of fly-ash-based geopolymers when compared to OPC materials, due to the latter diminished fiber-matrix bond, affecting its cracking mechanisms. In an additional study, Shaikh [68] also demonstrated improvements for the same GP mixture with hook ends steel fibers reinforcements. The use of short carbon fibers [15,69], in different lengths, demonstrated that the use of 7 mm fibers led to superior mechanical behavior, even when exposed to temperature, reaching fiber deterioration only after 1300 °C, as a result of the fiber efficiency up to high temperatures. The response of geopolymer composites based on silica fume and metakaolin, reinforced with short basalt fibers [17], presented 50% superior responses in tensile and flexural loading when compared to OPC based ones.

Sankar and Kriven [70] investigated the processing, microstructure, and mechanical properties of K-geopolymer composites reinforced with fique fibers using pressurized plates. The results showed high flexural strength values and low fiber-matrix adhesion. Also, they studied the incorporation of jute fabrics in a Na-based medium [71], where they found superior mechanical behavior, even without the use of pressurization methods on the plates.

The increasing demand of newfound applications with geopolymer composites generates an expectation for materials able to maintain the high quality throughout its service life [72]. To eliminate and repair eventual problems, innovative composites with enhanced properties are expected to arise. The so-called high-performance short fiber reinforced ceramic materials (HPFRCM), appear as an interesting solution [68,72,73]. Its fundamentals are largely related to cementitious materials but may be considered in geopolymer formulations with some modifications. This class can be distinguished into two groups, regarding tensile ductility and strength: strain-hardening ceramic composites (SHCC) and ultra-high-performance fiber-reinforced ceramic composites (UHPFRCC) [65]. Table 2.4 presents the properties and distinctions of both groups [65]. Figure 2.10 presents the typical tensile curves of SHCC and UHPFRC [73,74].

SHCC achieves moderate tensile strength, and ultra-ductility, with moderate fiber content [72-74]. UHPFRCC presents extreme high strengths, but at low strain ranges [73,74]. To overcome long-term issues, related to crack opening and penetration of aggressive agents, the SHCC model appears to be the most suitable, and its design criteria should be followed when developing such technology.

Table 2.4 – Classification and properties of HPFRCC [74]: SHCC and UHPFRCC.

Properties	SHCC	UHPFRCC
Mechanics	Moderate tensile strength (3–8 MPa)	High tensile and flexural (25-60 MPa) strengths
Fiber content	Moderate (1% < Vf < 3%)	
Strain capacity	Ultra-ductility	Moderate ductility
Crack patterns	Multiple finely spaced cracks of tight widths	Fine cracks in the pre-peak region, usually localized in points of weakness
Matrix design	Fine-grained engineered matrix developed with the use of micromechanically based formulations	
Durability	Long-term and chloride diffusion resistance, due to fine crack control	Denser matrix, highly resistant to capillary suction

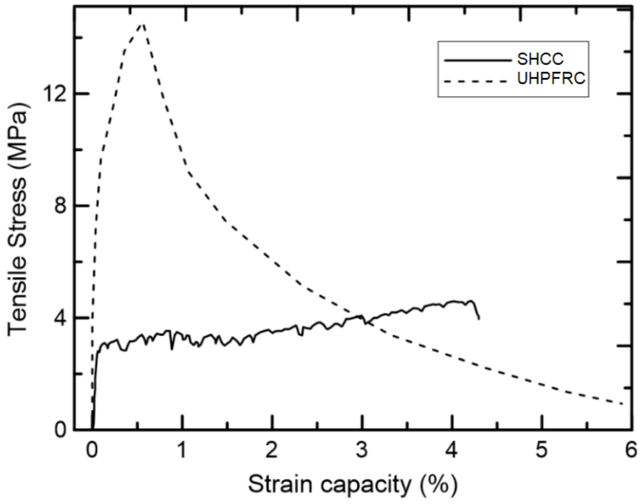

Figure 2.10 – Typical tensile curves of SHCC and UHPFRCC [74].

Geopolymer materials were mechanically exploited in this sense, although with few variations, generating great potential in the development for suitable applications of strain-hardening geopolymer composites (SHGC), or, also commonly described engineered geopolymer composites (EGC). A previous study [54] produced geopolymer composites reinforced with 2% of PVA and PE fibers. The matrix corresponded to the dissolution of fly ash with sodium hydroxide in adequate proportions. In contrast, [75] produced a cementitious material (Type I OPC) incorporated with the same amount of PVA fibers (REC15), with distinctions in use/or not of coatings (1.2%). An additional study was performed by [76]. A 42.5R-HS cementitious material was used, with equal proportions of reinforcement. Figure 2.11 presents the results obtained by each variation.

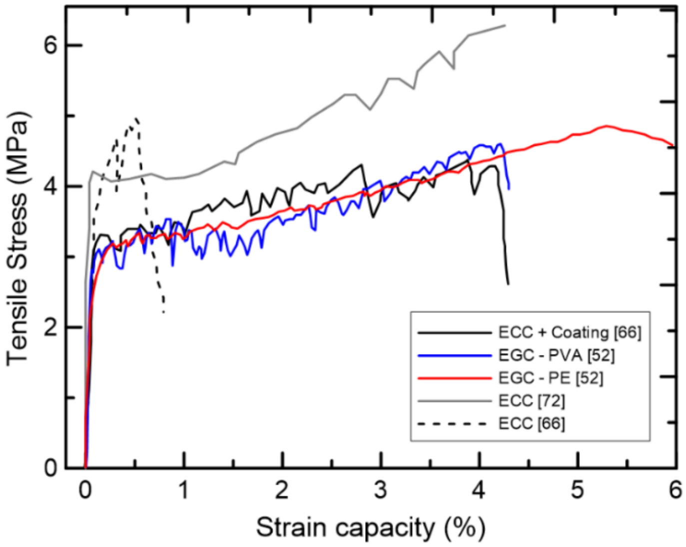

Figure 2.11 – EGC x ECC comparison under direct tensile loading [47,75,76].

It is possible to observe that from all the studied materials, the cementitious composite without the presence of coating [75] achieved the smaller capacity of deformation, whereas the one that used 42.5R-HS [76] presented greater stress at first cracking and failure. However, the PE-based geopolymer composite [55] showed the better deformation capacity of them all, reinforcing the viability of the geopolymer material as an alternative to the well-know SHCC technology. A previous study [55] also investigated the mechanical response of this reinforcement by using different fly-ash based mixtures. Distinct geopolymer formulations reinforced with 2% content of PVA fibers were produced, with solutions made of (i) $NaOH^1$; (ii) $NaOH^2$; (iii) KOH; and (iv) lime. The composite produced with the $NaOH^1$ solution - type 1 achieved the best results, in ultimate stress and deformation capacity, since it presented the higher stress-performance index (σ_0/σ_{fc}; characteristic stress/first-crack stress) compared to that of the other EGC and ECC composites. This is a result of an optimum balance of alkalis in the solution, reaching proper amounts of SiO_2, that influence on the rheology and fiber dispersion. The composite produced with the NaOH solution - type 2, did not present multiple cracking behavior, a factor influenced by lower workability accompanied by an extremely low tensile strength. The composites produced with K and lime solutions showed intermediate stresses and deformations.

It is important to note that all previous analyzes were made based on quasi-static loading tests. Few studies have discussed the geopolymer compressive behavior under dynamic loadings. Xin *et al*. [77] evaluated the use of two alkali solutions based on NaOH and Na_2CO_3 on a fly ash-based geopolymer concrete, and the first one showed improved mechanical capacities when compared to the same strength obtained at quasi-static testing. However, so far, little is understood about the geopolymers behavior at high loading rates, with even less focus on geopolymer composites.

2.4. Geopolymers durability

2.4.1. Extreme exposure conditions

The degradation process of any material presents considerable influence on its service life and safety [78]. Geopolymer deterioration may occur through a variety of physical and chemical processes, especially when exposed to aggressive environments [2,3,10]. Previous studies [1,20] affirm that ceramic materials dated more than 3,000 years ago have presented greater durability and mechanical properties than newly formed products by ordinary Portland cement (OPC), since a material ability to withstand time is predominantly related to its composition and microstructure [1,2,20,79]. Intrinsic properties of products based on OPCs generate high permeability, allowing the passage of water and other aggressive agents that may result in chemical reactions that will accelerate its deterioration process, particularly by the presence of calcium hydroxide (C-S-H) in the matrix [2,79]. Geopolymers, as presented before, are nanoparticle, nano porous, amorphous based materials with minimum or no calcium content. Thus, it is expected that the degradation processes occur in a different form, presenting higher vulnerability in materials with higher calcium amounts, as in the case of alkali-activated ones [8,10].

The geopolymer degradation may occur mainly through chemical modifications/attacks, aging, damage caused by swelling and temperature exposure. The chemical durability can most commonly be evaluated through sulfate and seawater attack [3,10]; and acid attack. Several studies indicate a particularly good resistance to conventional sulfate attacks due to the absence of hydrate-calcium products [3,72]. An interesting behavior can also be observed for geopolymers exposed to an acid media [3,10], proven to be far superior to the ones presented by OPC materials [1,3,10]. The material long-term behavior is usually predicted through accelerated degradation tests, as wetting/drying (w/d) and freezing/thawing (f/t) cycles. Albitar *et al* [80] investigated the durability performance of both fly-ash based geopolymer and ordinary Portland-cement concrete (OPC) after 10 w/d cycles. The geopolymer material showed superior durability, reflecting the stability of the formulation and the deterioration susceptibility of the OPC. Several other studies have found significant higher performances under accelerated aging processes [81-82], showing great potential in the durability of geopolymers when compared to traditional construction materials.

However, the greatest potential of this technology has been explored since its first development, that is its performance when subjected to high temperatures, which will be further discussed in the following sections.

2.4.2. Thermal behavior of plain geopolymers

In its plain form, thermal expansions can result in destructive internal stresses when structural elements are exposed to elevated temperatures [2]. However, the amorphous and inorganic structure of geopolymers generates satisfactory performance regarding thermal durability, resulting in potential applications as refractories or fire-resistant materials [10]. Previous studies [83,84] analyzed such effects showing distinct characteristics, depending on the alkali solution and precursors, according to the dehydration, densification, and crystallization phases.

Fillers and aggregates may be incorporated to reduce thermal expansion, such as chamotte, vermiculite, and glass powders [13,84]. However, it is important to observe possible distinctions in the thermal expansion coefficient of each component, and its chemical composition [10]. Studies developed by Davidovits [1,16] mention a high resistance under extreme temperature regarding geopolymers composed of sodium silicate and metakaolin up to 1200 °C. This result is related to the recrystallization of ceramics at elevated temperatures. Barbosa *et al.* [85] showed that higher contents of water and/or sodium silicate may reduce the thermal resistance of the material. Geopolymers based on potassium silicate also demonstrated high thermal stability up to 1300 ºC [85]. The results presented in several studies [13,83-85] indicate that the mode of decomposition of geopolymers corresponds to deterioration of its structure, usually in the range of 900 ºC in mixtures based on metakaolin, and between 500 ºC and 700 °C in mixtures containing fly ash, with recrystallization and recovery of mechanical performance around 1200 ºC for both materials.

In an additional study, Barbosa *et al.* [86] demonstrated that the same fly ash matrix, when incorporated with natural river aggregates (particulate reinforcement), presented gradual decreases in strength as the exposure to temperature increased. This mechanism occurs due to the thermal expansion of the natural aggregates, resulting in a material incompatibility. It is important to notice, however, that most of the studies did not use aggregates in their formulations. This occurs since part of the research involving geopolymers aims to investigate the material’s adhesive behavior and as a high-performance ceramic [13]. It is fundamental, however, to select an aggregate that will not react with the precursors during the mixing and curing processes.

Few studies have also reported improved behavior regarding the exposure to elevated temperatures of geopolymers based on aluminosilicate materials from lateritic soils [87]. Lateritic soils are found in regions with a tropical climate [88], from climatic processes favoring the formation of iron, aluminum, magnesium, and titanium oxides. Results show excellent thermal and chemical durability for this class of materials in extreme conditions up to 1500 ºC [89].

2.4.3. Thermal behavior of fiber-reinforced geopolymers

The composites behavior under temperature exposure can be distinguished into two temperature ranges: (i) elevated temperatures (up to 300 ºC); and (ii) high temperatures (above 300 ºC).

Samal *et al.* [90] studied the influence of high temperature on the degradation of carbon, glass, and basalt textile reinforced geopolymers. The study stated that composites made of carbon fibers presented increases in residual strength after 600 ºC, as opposed to a continuous degradation found for the other two reinforcements, due to the fiber's intrinsic thermal resistance, thus suggesting applications as thermal barrier coatings and panels for the carbon reinforced geopolymer. Aygörmez *et al.* [91] found that the polypropylene reinforcement can be efficiently used in fly-ash-based geopolymers up to 900 ºC, compared to the same unreinforced binders, due to their melting and occupation of pores microstructure defects.

Trindade *et al.* [92] studied the influence of elevated temperatures on the mechanical behavior of jute-fiber reinforced geopolymers made of metakaolin and found that composites made with the chamotte refractory aggregate were more effective than those manufactured with sand, due to the thermal expansion of the latter. In such refractory combination, jute textiles were effective up to 200 ºC.

Only a few studies have discussed the temperature effects on 1% by volume of short synthetic fibers, such as PVA, polypropylene (PP), and modified polyamide and polyolefin [93-95]. When exposed to elevated temperatures, PVA and especially PP fiber reinforced specimens showed a strength reduction lower than those of polyamide and polyolefin specimens up to 300 ºC, due to melting and decomposition of the fibers. The efficiency of the synthetic reinforcements, such as PVA and PE still needs to be properly demystified, to establish their service temperature limit, especially regarding its use in strain-hardening geopolymer composites (SHGC) technologies since no literature on the subject was found up to date.

2.5. References

[1] Davidovits, J., Davidovics, M., & Davidovits, N. (1998). U.S. Patent No. 5,798,307. Washington, DC: U.S. Patent and Trademark Office.

[2] Kriven, W. M. (2017). Geopolymer-based composites. In Comprehensive composite materials II (pp. 269-280). Elsevier.

[3] Vickers, L., Van Riessen, A., & Rickard, W. D. (2015). Fire-resistant geopolymers: role of fibres and fillers to enhance thermal properties. Springer Singapore.

[4] Provis, J. L., & Van Deventer, J. S. J. (Eds.). (2009). Geopolymers: structures, processing, properties and industrial applications. Elsevier.

[5] Fernández-Jiménez, A., & Palomo, A. (2005). Composition and microstructure of alkali activated fly ash binder: Effect of the activator. Cement and concrete research, 35(10), 1984-1992.

[6] Fernandez-Jimenez, A. M., Palomo, A., & Lopez-Hombrados, C. (2006). Engineering properties of alkali-activated fly ash concrete. ACI Materials Journal, 103(2), 106.

[7] Kriven, W. M., Bell, J. L., & Gordon, M. (2003). Microstructure and microchemistry of fully-reacted geopolymers and geopolymer matrix composites. Ceramic Transactions, 153(1994), 227-250.

[8] Borges, P. H., Banthia, N., Alcamand, H. A., Vasconcelos, W. L., & Nunes, E. H. (2016). Performance of blended metakaolin/blastfurnace slag alkali-activated mortars. Cement and Concrete Composites, 71, 42-52.

[9] Giancaspro, J., Balaguru, P. N., & Lyon, R. E. (2006). Use of inorganic polymer to improve the fire response of balsa sandwich structures. Journal of materials in civil engineering, 18(3), 390-397.

[10] Provis, J. L., & Van Deventer, J. S. (Eds.). (2013). Alkali activated materials: state-of-the-art report, RILEM TC 224-AAM (Vol. 13). Springer Science & Business Media.

[11] Duxson, P., Fernández-Jiménez, A., Provis, J. L., Lukey, G. C., Palomo, A., & van Deventer, J. S. (2007). Geopolymer technology: the current state of the art. Journal of materials science, 42(9), 2917-2933.

[12] Pacheco-Torgal, F., Castro-Gomes, J., & Jalali, S. (2008). Alkali-activated binders: A review: Part 1. Historical background, terminology, reaction mechanisms and hydration products. Construction and Building Materials, 22(7), 1305-1314.

[13] Davidovits, J. (2008). Geopolymer chemistry and applications. Geopolymer Institute.

[14] Purdon, A. O. (1940). The action of alkalis on blast-furnace slag. Journal of the Society of Chemical Industry, 59(9), 191-202.

[15] Glukhovsky, V. D., & Pakhomov, V. A. (1978). Slag-alkali cements and concretes. Budivelnik Kiev.

[16] Davidovits, J. (1999, June). Chemistry of geopolymeric systems, terminology. In Geopolymer (Vol. 99, No. 292, pp. 9-39). sn.

[17] Davidovits, J. (1991). Geopolymers: inorganic polymeric new materials.

Journal of Thermal Analysis and calorimetry, 37(8), 1633-1656.

[18] Lyon, R. E., Balaguru, P. N., Foden, A., Sorathia, U., Davidovits, J., & Davidovics, M. (1997). Fire-resistant aluminosilicate composites. Fire and materials, 21(2), 67-73.

[19] Davidovits, J. (1994). Geopolymers: man-made rock geosynthesis and the resulting development of very early high strength cement. Journal of Materials education, 16, 91-91.

[20] Sankar, K., Stynoski, P., Al-Chaar, G. K., & Kriven, W. M. (2018). Sodium silicate activated slag-fly ash binders: Part I–Processing, microstructure, and mechanical properties. Journal of the American Ceramic Society, 101(6), 2228-2244.

[21] Fletcher, R. A., MacKenzie, K. J., Nicholson, C. L., & Shimada, S. (2005). The composition range of aluminosilicate geopolymers. Journal of the European Ceramic Society, 25(9), 1471-1477.

[22] Rahier, H., Simons, W., Van Mele, B., & Biesemans, M. (1997). Low-temperature synthesized aluminosilicate glasses: Part III Influence of the composition of the silicate solution on production, structure and properties. Journal of Materials Science, 32(9), 2237-2247.

[23] Barbosa, V. F. F., Mackenzie, K. J., & Thaumaturgo, C. (1999). Synthesis and characterisation of sodium polysialate inorganic polymer based on alumina and silica. In Geopolymer'99 International Conference, France.

[24] Bernal, S. A., Rodríguez, E. D., Kirchheim, A. P., & Provis, J. L. (2016). Management and valorisation of wastes through use in producing alkali-activated cement materials. Journal of Chemical Technology & Biotechnology, 91(9), 2365-2388.

[25] Davidovits, J. (1994). Geopolymers: man-made rock geosynthesis and the resulting development of very early high strength cement. Journal of Materials education, 16, 91-91.

[26] Assi, L. N., Carter, K., Deaver, E., & Ziehl, P. (2020). Review of availability of source materials for geopolymer/sustainable concrete. Journal of Cleaner Production, 263, 121477.

[27] Trindade, A. C. C., Silva, F. D. A., Alcamand, H. A., & Borges, P. H. R. (2017). On the mechanical behavior of metakaolin based geopolymers under elevated temperatures. Materials Research, 20, 265-272.

[28] Ribeiro, R. A. S., Ribeiro, M. G. S., Sankar, K., & Kriven, W. M. (2016). Geopolymer-bamboo composite–A novel sustainable construction material. Construction and Building Materials, 123, 501-507.

[29] Rovnaník, P., & Šafránková, K. (2016). Thermal behaviour of metakaolin/fly ash geopolymers with chamotte aggregate. Materials, 9(7), 535.

[30] Abbasi, S. M., Ahmadi, H., Khalaj, G., & Ghasemi, B. (2016). Microstructure and mechanical properties of a metakaolinite-based geopolymer nanocomposite reinforced with carbon nanotubes. Ceramics International, 42(14), 15171-15176.

[31] Wattimena, O. K., Antoni, & Hardjito, D. (2017, September). A review on the effect of fly ash characteristics and their variations on the synthesis of fly ash based geopolymer. In AIP Conference Proceedings (Vol. 1887, No. 1, p. 020041). AIP Publishing LLC.

[32] Škvára, F., Jílek, T., & Kopecký, L. (2005). Geopolymer materials based on fly ash. Ceram.-Silik, 49(3), 195-204.

[33] Gunasekara, C., Law, D. W., & Setunge, S. (2016). Long term permeation properties of different fly ash geopolymer concretes. Construction and Building Materials, 124, 352-362.

[34] Khater, H. M. (2013). Effect of silica fume on the characterization of the geopolymer materials. International Journal of Advanced Structural Engineering, 5(1), 1-10.

[35] He, J., Jie, Y., Zhang, J., Yu, Y., & Zhang, G. (2013). Synthesis and characterization of red mud and rice husk ash-based geopolymer composites. Cement and Concrete Composites, 37, 108-118.

[36] Eliche-Quesada, D., Bonet-Martínez, E., Pérez-Villarejo, L., Castro, E., & Sánchez-Soto, P. J. (2021). Effects of an Illite Clay Substitution on Geopolymer Synthesis as an Alternative to Metakaolin. Journal of Materials in Civil Engineering, 33(5), 04021072.

[37] Puligilla, S., & Mondal, P. (2013). Role of slag in microstructural development and hardening of fly ash-slag geopolymer. Cement and Concrete Research, 43, 70-80.

[38] Roy, D. M. (1999). Alkali-activated cements opportunities and challenges. Cement and concrete research, 29(2), 249-254.

[39] Lloyd, R. R. (2009). Accelerated ageing of geopolymers. In Geopolymers (pp. 139-166). Woodhead Publishing.

[40] Alcamand, H. A., Borges, P. H., Silva, F. A., & Trindade, A. C. C. (2018). The effect of matrix composition and calcium content on the sulfate durability of metakaolin and metakaolin/slag alkali-activated mortars. Ceramics International, 44(5), 5037-5044.

[41] Yu, J., Chen, Y., Chen, G., & Wang, L. (2020). Experimental study of the feasibility of using anhydrous sodium metasilicate as a geopolymer activator for soil stabilization. Engineering Geology, 264, 105316.

[42] Nematollahi, B., Sanjayan, J., & Shaikh, F. U. A. (2015). Synthesis of heat and ambient cured one-part geopolymer mixes with different grades of sodium silicate. Ceramics International, 41(4), 5696-5704.

[43] Zhang, B., Guo, H., Deng, L., Fan, W., Yu, T., & Wang, Q. (2020). Undehydrated kaolinite as materials for the preparation of geopolymer through phosphoric acid-activation. Applied Clay Science, 199, 105887.

[44] Davidovits, J. (1999, June). Chemistry of geopolymeric systems, terminology. In Geopolymer (Vol. 99, No. 292, pp. 9-39).

[45] Swaddle, T. W., Salerno, J., & Tregloan, P. A. (1994). Aqueous aluminates, silicates, and aluminosilicates. Chemical Society Reviews, 23(5), 319-325.

[46] Li, W., Lemougna, P. N., Wang, K., He, Y., Tong, Z., & Cui, X. (2017). Effect of vacuum dehydration on gel structure and properties of metakaolin-based geopolymers. Ceramics International, 43(16), 14340-14346.

[47] Temuujin, J., Minjigmaa, A., Rickard, W., Lee, M., Williams, I., & Van Riessen, A. (2009). Preparation of metakaolin based geopolymer coatings on metal substrates as thermal barriers. Applied clay science, 46(3), 265-270.

[48] Bentur, A., & Mindess, S. (2006). Fibre reinforced cementitious composites. Crc Press.

[49] Hannant, P. J. (1978). Fibre cements and fibre concretes (No. Monograph).

[50] Naaman, A. E. (2003). Engineered steel fibers with optimal properties for reinforcement of cement composites. Journal of advanced concrete technology, 1(3), 241-252.

[51] Silva, F. D., & Chawla, N. (2008). Tensile behavior of high performance natural (sisal) fibers. Composites Science and Technology, 68(15), 3438-3443.

[52] Fidelis, M. E. A., Pereira, T. V. C., Gomes, O. D. F. M., de Andrade Silva, F., & Toledo Filho, R. D. (2013). The effect of fiber morphology on the tensile strength of natural fibers. Journal of Materials Research and Technology, 2(2), 149-157.

[53] Ferreira, S. R., de Andrade Silva, F., Lima, P. R. L., & Toledo Filho, R. D. (2017). Effect of hornification on the structure, tensile behavior and fiber matrix bond of sisal, jute and curauá fiber cement based composite systems. Construction and Building Materials, 139, 551-561.

[54] Nematollahi, B., Sanjayan, J., & Ahmed Shaikh, F. U. (2015). Tensile strain hardening behavior of PVA fiber-reinforced engineered geopolymer composite. Journal of Materials in Civil Engineering, 27(10), 04015001.

[55] Lu, Z., Yao, J., & Leung, C. K. (2019). Using graphene oxide to strengthen the bond between PE fiber and matrix to improve the strain hardening behavior of SHCC. Cement and Concrete Research, 126, 105899.

[56] Low, I. M. (Ed.). (2006). Ceramic-matrix composites: Microstructure, properties and applications. Woodhead Publishing.

[57] Bernal, S. A., Bejarano, J., Garzón, C., de Gutiérrez, R. M., Delvasto, S., & Rodríguez, E. D. (2012). Performance of refractory aluminosilicate particle/fiber-reinforced geopolymer composites. Composites Part B: Engineering, 43(4), 1919-1928.

[58] Keane, P. F., & Kriven, W. M. (2019). Microstructure and flexure strengths of dolomite particulate-reinforced geopolymer composites. In Proceedings of the 42nd International Conference on Advanced Ceramics and Composites: Ceramic Engineering and Science Proceedings Volume 39, Issue 3 (pp. 171-181). Hoboken, NJ, USA: John Wiley & Sons, Inc.

[59] Bhuiya, A. W., Hu, M., Sankar, K., Keane, P. F., Ribero, D., & Kriven, W. M. (2021). Bone ash reinforced geopolymer composites. Journal of the American Ceramic Society, 104(6), 2767-2779.

[60] Keane, P. F., Foltz, J. S., Chadha, V., Marsh, C. P., & Kriven, W. M. (2021). Amorphous self-healed, chopped basalt fiber-reinforced, geopolymer composites. Journal of the American Ceramic Society, 104(7), 3443-3451.

[61] Trindade, A. C. C., Alcamand, H. A., Borges, P. H. R., & Silva, F. A. (2017). On the durability behavior of natural fiber reinforced geopolymers. Ceramic and Science Proceedings, 38(3), 215-228.

[62] Curosu, I., Liebscher, M., Mechtcherine, V., Bellmann, C., & Michel, S. (2017). Tensile behavior of high-strength strain-hardening cement-based composites (HS-SHCC) made with high-performance polyethylene, aramid and PBO fibers. Cement and Concrete Research, 98, 71-81.

[63] Allen, H. G. (1971). The purpose and methods of fibre reinforcement. In Prospects of fibre reinforced construction materials. Proc Int Building Exhibition Conference. Building Research Station, UK (pp. 3-14).

[64] Jones, R. M. (1998). Mechanics of composite materials. CRC press.

[65] Persson, M. (2008). Fibres in reinforced concrete structures–analysis, experiments and design. Chalmers Tekniska Hogskola (Sweden).

[66] de Andrade Silva, F., Mobasher, B., & Toledo Filho, R. D. (2009). Cracking mechanisms in durable sisal fiber reinforced cement composites. Cement and concrete composites, 31(10), 721-730.

[67] Ahmed, S. F. U., Maalej, M., & Paramasivam, P. (2007). Flexural responses of hybrid steel–polyethylene fiber reinforced cement composites containing high volume fly ash. Construction and building materials, 21(5), 1088-1097.

[68] Shaikh, F. U. A. (2019). Pullout Behavior of Hook End Steel Fibers in Geopolymers. Journal of Materials in Civil Engineering, 31(6), 04019068.

[69] He, P., Jia, D., Lin, T., Wang, M., & Zhou, Y. (2010). Effects of high-temperature heat treatment on the mechanical properties of unidirectional carbon fiber reinforced geopolymer composites. Ceramics International, 36(4), 1447-1453.

[70] Sankar, K., & Kriven, W. M. (2015). Potassium geopolymer reinforced alkali-treated fique. Developments in Strategic Materials and Computational Design V, edited by WM Kriven, D. Zhou, K. Moon, T. Hwang, J. Wang, C. Lewinssohn and Y. Zhou, Cer. Engr. Sci. Proc, 38(10), 61-78.

[71] Sankar, K., & Kriven, W. M. (2015). Sodium geopolymer reinforced with jute weave. Developments in Strategic Materials and Computational Design V, edited by WM Kriven, D. Zhou, K. Moon, T. Hwang, J. Wang, C. Lewinssohn and Y. Zhou, Cer. Engr. Sci. Proc, 38(10), 39-60.

[72] Mechtcherine, V. (2013). Novel cement-based composites for the strengthening and repair of concrete structures. Construction and building materials, 41, 365-373.

[73] Li, V. C., Wu, C., Wang, S., Ogawa, A., & Saito, T. (2002). Interface tailoring for strain-hardening polyvinyl alcohol-engineered cementitious composite (PVA-ECC). Materials Journal, 99(5), 463-472.

[74] van Zijl, G. P., Wittmann, F. H., Oh, B. H., Kabele, P., Toledo Filho, R. D., Fairbairn, E. M., ... & Lepech, M. D. (2012). Durability of strain-hardening cement-based composites (SHCC). Materials and structures, 45(10), 1447-1463.

[75] Li, V. C. (2003). On engineered cementitious composites (ECC) a review of the material and its applications. Journal of advanced concrete technology, 1(3), 215-230.

[76] Mechtcherine, V., de Andrade Silva, F., Butler, M., Zhu, D., Mobasher, B., Gao, S. L., & Mäder, E. (2011). Behaviour of strain-hardening cement-based composites under high strain rates. Journal of Advanced Concrete Technology, 9(1), 51-62.

[77] Xin, L., Jin-yu, X., Weimin, L., & Erlei, B. (2014). Effect of alkali-activator types on the dynamic compressive deformation behavior of geopolymer concrete. Materials Letters, 124, 310-312.

[78] Fernández-Jiménez, A., Palomo, A., & Revuelta, D. (2009, September). Alkali activation of industrial by-products to develop new earth-friendly cements. In Proceeding of the 11th International Conference on Non-Conventional Materials and Technologies, Bath, UK (pp. 6-9).

[79] Barrer, R. M. (1982). Hydrothermal chemistry of zeolites. Academic press.

[80] Albitar, M., Ali, M. M., Visintin, P., & Drechsler, M. (2017). Durability evaluation of geopolymer and conventional concretes. Construction and Building Materials, 136, 374-385.

[81] Trindade, A. C. C., Alcamand, H. A., Borges, P. H. R., & Silva, F. A. (2017). On the durability behavior of natural fiber reinforced geopolymers. Ceramic and Science Proceedings, 38(3), 215-228.

[82] Pilehvar, S., Szczotok, A. M., Rodríguez, J. F., Valentini, L., Lanzón, M., Pamies, R., & Kjøniksen, A. L. (2019). Effect of freeze-thaw cycles on the mechanical behavior of geopolymer concrete and Portland cement concrete containing micro-encapsulated phase change materials. Construction and Building Materials, 200, 94-103.

[83] Davidovits, J., & Davidovics, M. (1991). Geopolymer: ultra-high temperature tooling material for the manufacture of advanced composites. How Concept Becomes Reality., 36, 1939-1949.

[84] Van Deventer, J. S. J., Provis, J. L., Duxson, P., & Lukey, G. C. (2007). Reaction mechanisms in the geopolymeric conversion of inorganic waste to useful products. Journal of hazardous materials, 139(3), 506-513.

[85] Barbosa, V. F., & MacKenzie, K. J. (2003). Synthesis and thermal behaviour of potassium sialate geopolymers. Materials Letters, 57(9-10), 1477-1482.

[86] Barbosa, V. F., & MacKenzie, K. J. (2003). Thermal behaviour of inorganic geopolymers and composites derived from sodium polysialate. Materials research bulletin, 38(2), 319-331.

[87] Ab Aziz, N. N. S. N., Mukri, M., Hashim, S., & Khalid, N. (2015). Influence of Compaction Effort for Laterite Soil Mix With Geopolymer in Designing Soil Liner. Ejge, 20, 12353-12364.

[88] de Araujo Neto, M. D., Furley, P. A., Haridasan, M., & Johnson, C. E. (1986). The murundus of the cerrado region of Central Brazil. Journal of Tropical Ecology, 2(1), 17-35.

[89] Obonyo, E. A., Kamseu, E., Lemougna, P. N., Tchamba, A. B., Melo, U. C., & Leonelli, C. (2014). A sustainable approach for the geopolymerization of natural iron-rich aluminosilicate materials. Sustainability, 6(9), 5535-5553.

[90] Samal, S., Thanh, N. P., Petríková, I., Marvalová, B., Vallons, K. A., & Lomov, S. V. (2015). Correlation of microstructure and mechanical properties of various fabric reinforced geo-polymer composites after exposure to elevated temperature. Ceramics International, 41(9), 12115-12129.

[91] Aygörmez, Y., Canpolat, O., Al-mashhadani, M. M., & Uysal, M. (2020). Elevated temperature, freezing-thawing and wetting-drying effects on polypropylene fiber reinforced metakaolin based geopolymer composites. Construction and Building Materials, 235, 117502.

[92] Trindade, A. C. C., Alcamand, H. A., Borges, P. R., & de Andrade Silva, F. (2017). Influence of Elevated Temperatures on the Mechanical Behavior of Jute-Textile-Reinforced Geopolymers.

[93] Tanyildizi, H., & Yonar, Y. (2016). Mechanical properties of geopolymer concrete containing polyvinyl alcohol fiber exposed to high temperature. Construction and Building Materials, 126, 381-387.

[94] Albidah, A., Abadel, A., Alrshoudi, F., Altheeb, A., Abbas, H., & Al-Salloum, Y. (2020). Bond strength between concrete substrate and metakaolin geopolymer repair mortars at ambient and elevated temperatures. Journal of Materials Research and Technology, 9(5), 10732-10745.

[95] Arslan, A. A., Uysal, M., Yılmaz, A., Al-mashhadani, M. M., Canpolat, O., Şahin, F., & Aygörmez, Y. (2019). Influence of wetting-drying curing system on the performance of fiber reinforced metakaolin-based geopolymer composites. Construction and Building Materials, 225, 909-926.

3 Influence of precursor materials on the rheological and thermo-chemo-mechanical properties of sodium-based geopolymers

3.1. Introduction

Geopolymers are ceramic materials that combine an aluminosilicate precursor with an alkaline reagent [1]. The geopolymerization process involves the dissolution of the solid aluminosilicate, resulting in the release of ions into the aqueous phase due to the alkaline hydrolysis reaction [2,3]. The increased Al and Si concentrations in the alkaline medium stimulate the condensation reactions until reaching equilibrium [2]. The rate of dissolution is directly dependent on the Al and Si concentration of the precursors [2,4]. Most studies with geopolymers use fly ash and/or metakaolin, as the aluminosilicate solid, due to local and wide availability [4]. Such materials are mostly developed due to their comparable-to-concrete mechanical capacities [3,4] and fire-resistant applications [5].

Recent data from the construction industry show the importance of developing new sustainable technologies [6], such as geopolymer binders, combining reductions in CO_2 emissions with the use of widely available materials that can effectively compete with conventional ones, i.e., based on Portland cement. To achieve this goal, it is necessary to study, modify and standardize several characteristics of the new technology, providing constructive solutions with a high level of confidence. In this sense, the use of varied precursor materials appears as a major challenge in the widespread geopolymer use, since distinct chemical and morphological characteristics can be found in a huge variety of kaolin deposits [7,4], mineral production wastes (fly ashes), and other pozzolans [8,4]. Additionally, an enormous variety of geopolymer formulations has been established in the literature, mainly modifying the SiO_2/Al_2O_3 ratios [9,10], causing difficulties in standardizing and understanding the effects of each precursor used in their chemical, rheological and mechanical processes at room conditions and when exposed to temperature.

Wang *et al.* [11], for example, studied the effects of using SiO_2/Al_2O_3 ratios equal to 1.0 and 2.0, in the dissolution of high-reactive metakaolin in an alkaline sodium-based media, concluding that the increased ratios resulted in longer dissolution times up to equilibrium and weaker molecules bond, due to excessive silicate species, affecting the strength and elastic modulus of the samples. This was also observed by Trochez *et al.* [12], adding the fact that this behavior is less significant when associated with higher Na_2O/SiO_2 ratios (up to 0.25) since larger reaction extents can be achieved. Meanwhile, Kriven *et al.* [13] focused on obtaining chemical refinements in geopolymer formulations, using a high reactive metakaolin [14,15], to achieve as close to a fully reacted geopolymer as possible, i.e., SiO_2/Al_2O_3 and Na_2O/SiO_2 ratios of 4.0 and 0.25, respectively. This combination resulted in a well-studied and applied reactive, nanoporous, and brittle product, with enormous rheological [16] and mechanical potential [17], that has been successfully used as the main binder in composite materials with varied fibers contents [16], presenting itself as a suitable option to be applied into quasi-static [17] and dynamic solicitations [18], and at room or elevated temperatures demands [19]. However, the incorporation of varied precursors in this formulation has not yet been completely demystified, given the enormous chemical variety found in different aluminosilicate sources around the world [7,8,17].

The study of SiO_2/Al_2O_3 synthesizing parameters from 3.2 to 3.7, provided by Ghosh and Ghosh [20], revealed that the workability, setting time, and microstructure development of a fly-ash geopolymer were directly dependent on the alkali solution, i.e., SiO_2 content and H_2O/binder ratio, since water plays an important role during dissolution, polycondensation and hardening stages. In the following study [21] they produced a fly-ash geopolymer with average 25 MPa compressive strength and moderate flow of 80% by using an H_2O/binder ratio of 0.4, meaning that such material must undertake mechanical reductions by H_2O addition to achieve suitable rheology. Szabó and Mucsi [22] studied the replacement of fly-ash by varied portions of metakaolin, confirming also considerable rheological and mechanical modifications through SiO_2/Al_2O_3 and Na_2O/SiO_2 variations. Gullu [23] demonstrated that fly-ashes inclusions by up to 40% in a metakaolin-based GP resulted in major changes in the rheological parameter, providing increases in flowability, appearing also as grouting options in practice.

Opposed to that, in a comparative study, Alnahhal *et al.* [24] verified that the partial replacement of fly-ash by blast furnace slag reduced the workability of the binder.

Increased alkali solution viscosities, such as the one required with slag addition, significantly affected the rheology of the mixture, resulting in a very distinct viscoelastic behavior compared to the well-percolated fly-ash-based material [24]. The use of blast furnace slag in alkaline conditions generates the so-called alkali-activated material [25], due to its high calcium content, generally characterized by a lower Si coordination. The alkalinization of such precursor provides a diminished lower Si coordination [26], that in presence of calcium contents partially forms hydration products, coexisting the geopolymer gel and Ca-rich Al-substituted silicate hydrate (C-(A)-S-H) reaction products [25,27], therefore enabling a different microstructural and hardening evolution from the low-calcium reference geopolymers, that are essentially three-dimensionally stable. This chemical and microstructural modification also affects the heat resistance and long-term durability of the material. Alcamand *et al.* [28] evaluated the sulfate durability of calcium-free geopolymers and slag containing alkali-activated SiO_2/Al_2O_3 ratios from 3.0 to 3.9. Metakaolin-based geopolymers presented a higher sulfate resistance, while the parts replaced by slag alkali-activated material demonstrated extreme mechanical losses due to ettringite and gypsum deterioration in presence of calcium amounts [28]. Trindade *et al.* [29] and Bernal *et al.* [27], however, found that the partial replacement of metakaolin by slag improved the material's mechanical performance when exposed to high temperatures, with slight shrinkage differences at 600 ºC, due to calcium-phase modifications [27].

Therefore, a proper study combining knowledge regarding the use of distinct precursors, chemical ratios, rheological parameters, setting times, mechanical properties, and thermal capacities should be assessed to allow a standardized use of varied geopolymers in a wide range of applications, such as composites [17], masonry [28], oil-well plugging [29], under-water constructions [30], and many others. For this reason, the goal of this work is to evaluate the influence of different precursor materials (low-reactive metakaolin, high-reactive metakaolin, fly ash, and blast furnace slag) on the fresh, transient, and hardened states of geopolymers produced with fixed chemical parameters of $Na_2O \cdot Al_2O_3 \cdot 4SiO_2 \cdot 11H_2O$. For this, the precursor particles' morphological evaluations, as well as their influence on the viscosity of the pastes and the consequent setting times and hardening processes were assessed. Conventional flow-rate tests were conducted, as well as squeeze-flow evaluations, presenting results hitherto not available in the literature.

The heat involved in the reaction, the reactive portion of the samples, and their mechanical behavior at various ages served as additional parameters in the correlation of data, helping to understand the effects of each incorporation in such scenarios through calorimetry, XRD, salicylic acid/methanol (SAM) and HCl extractions, and compression tests. Also, mechanical tests with exposure to high temperatures were performed, allowing an association between the precursors used with a thermal prediction of their efficiency under temperature regimes.

3.2. Materials and specimen production

The geopolymers produced in this study were prepared with varied precursors: low-reactive metakaolin (MK_{LR} - Metacaulim do Brasil), blast furnace slag (BFS - Lafarge Holcim), class F fly-ash (FA - PozoFly), and a high-reactivity metakaolin (MK_{HR} - BASF). Table 3.1 presents the materials' chemical compositions and their inherent SiO_2/Al_2O_3 ratio.

Table 3.1 – Chemical composition of the precursor aluminosilicate materials (%).

Precursor [%]	SiO_2	Al_2O_3	Fe_2O_3	K_2O	CaO	MgO
Low reactive metakaolin (MK_{LR})	56.02	34.05	2.8	0.18	-	-
Blast furnace slag (BFS)	33.65	12.42	0.45	-	41.06	7.95
Fly-ash (FA)	56.03	29.41	6.16	3.77	2.07	-
High-reactive metakaolin (MK_{HR})	53.00	43.80	0.43	0.19	-	-

MK_{LR} was used as the main source, due to its wide local availability. Slag and fly ash were used as alternative precursors, partially replacing the amount of MK_{LR} by 40% by weight, thus modifying the matrices properties. MK_{HR}-based geopolymers were manufactured to allow a proper comparison between the highly reactive material and the local one. The precursors were combined with a sodium-based water-glass (WG) in fixed pre-established chemical ratios of $SiO_2/Al_2O_3 = 4.00$, $Na_2O/SiO_2 = 0.25$, $H_2O/Na_2O = 11.00$, following the chemical prescriptions of previous studies ($Na_2O \cdot Al_2O_3 \cdot 4SiO_2 \cdot 11H_2O$) [31,32]; meaning that the type of precursor and their composition directly affected the amount of sodium silicon dioxide (SiO_2), hydroxide in pellets (NaOH), and deionized water (H_2O) used in the water-glass production for each mixture. In general, the higher the SiO_2/Al_2O_3 ratio presented by the precursor in Table 3.1, the lower the SiO_2, and consequently

NaOH and H_2O, required to achieve the desired chemical equilibrium. The testing methods presented in this study will allow a greater understanding of the effects of such variations. Table 3.2 summarizes the proportions of the compounds of each type of matrix.

Table 3.2 – Content in g of incorporated materials for all GP variations (for 1 kg of precursors).

GP material [g]	Solids				WG		
	MK	BFS	FA	MK_{HR}	NaOH	H_2O	SiO_2
MK	1000.00	-	-	-	316.73	613.84	296.63
MK+BFS	600.00	400.00	-	-	167.42	413.65	183.54
MK+FA	600.00	-	400.00	-	221.69	579.58	244.63
MK_{HR}	-	-	-	1000.0	359.76	810.36	440.45

The hydroxide component, dissolved into the deionized water, was used in pellets with purity higher than 90%, followed by the addition of hydrophilic fumed silica CAB-O-SIL® M-5 from Cabot. It is valid to mention that all the WG used in this study were prepared 24h prior to the GP mixture procedure, allowing the solutions to cool down, avoiding undesired temperature increases, and consequently reduction of the setting time [33,34].

The matrices were prepared in an IKA 60 control equipment mixer as follows: (i) dry mixing of the precursors at 1000 rpm for 1 min; (ii) addition of WG in the amounts presented in Table 2, followed by its mixture for 1 more min at an intermediate speed of 1600 rpm to guarantee an adequate dispersion during clumping stages; and (iii) final mix for 1 min at 2000 rpm, reaching a homogeneous paste, ensuring an adequate degree of geopolymerization. The mixing procedure was recorded, acquiring data related to speed, torque, and temperature, as shown in Figure 3.1. These parameters were obtained with Labworldsoft 6 software in line with the IKA 60 control equipment, following the steps presented previously. It is worth noticing an almost constant slow torque (~18 N.cm) during the dry mixing, followed by alternating rises in torque values at each clumping stage after WG incorporation, until paste achievement. The temperature increased a maximum of 5 ºC for all mixing processes, due to the geopolymerization reaction occurring under alkaline conditions [34].

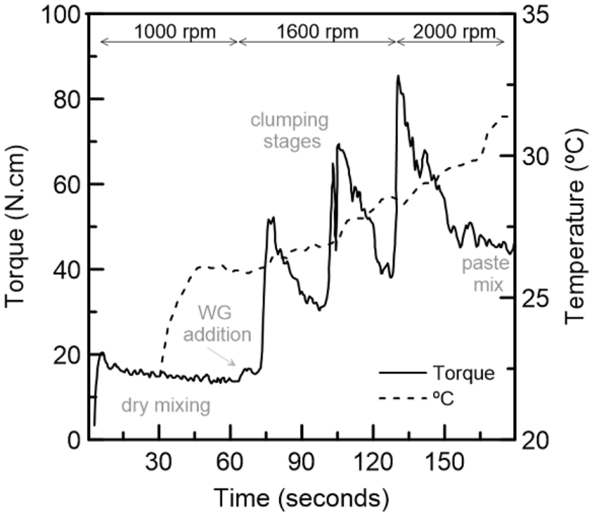

Figure 3.1 – Mixing procedure of the GP matrices.

The fresh GP mixtures were then used for the viscosity measurements or cast into cylindrical PVC molds with 5 x 10 cm (diameter and height), followed by a vibration step for consolidation and air voids removal. The molds were sealed in plastic bags for 24 h to prevent early dehydration, followed by the specimen's removal and storage inside dry plastic bags for the desired curing period, supported by the recommendations presented in earlier studies [31].

3.3. Testing Methods

3.3.1. Materials characterization

3.3.1.1. Particle analysis

Morphological analysis with the precursor materials was obtained with Morphologi 4 (Malvern Panalytical) throughout the scanning of optical static images, after the particles were spread on a glass-made slide, allowing more than 5,000 individual particles to be captured automatically, resulting in a wide range of statistical analysis in the Morphologi software.

3.3.1.2. X-ray diffraction (XRD)

The XRD patterns of the precursors and geopolymers were acquired through experiments on a Bruker D8 Discover diffractometer, using CuK α radiation ($\lambda K\alpha$ = 0.154186 nm), 40 kV and 40 mA, and LynxEye detector. A step size of 0.04º in an analytical range between 10º to 90 º (2θ) was programmed, and the scanning rates were adjusted to obtain a minimum of 5,000 counts on the most intense peak. The precursors were analyzed as received, and the geopolymer matrices were ground from fragments of 14-day aged specimens, with an agate mortar and pestle, from passing amount in the 200-mesh sieve.

Rietveld refinement was used to quantitatively perform a mineralogical analysis of the samples, using TOPAS software (Bruker AXS, Germany). The Rietveld method (RM) was used to adjust proposed theoretical models to the experimental data obtained, by least-square refinement until an acceptable convergence criterion was reached. The quality of the data obtained was evaluated by statistical parameters, namely weighted profile factor (R_{wp}), expected factor (R_{exp}), and goodness of fit (G_{OF}), calculated as indicated in previous works [35].

3.3.2. Fresh state properties

3.3.2.1. Viscosity

A Chandler viscometer Model 3530 was used at room temperature to obtain the rheological properties of the geopolymer matrices. A steel bob with 34 x 38 mm (diameter x length) and a rotor of 36 mm in diameter were used, allowing the paste to fill a 2 mm shear gap. Operating speeds of 3/6/10/20/30/60/100/200/300 rpm were set up, to result in specified shear rates of 5/10/17/34/51/102/170/341/511 s^{-1}. The data was acquired until the steady state of the mixtures was achieved. The testing procedure is presented in Fig. 3.2, showing the data-logging cycle obtained after 140 s by using Rheo 3000 Data Acquisition software.

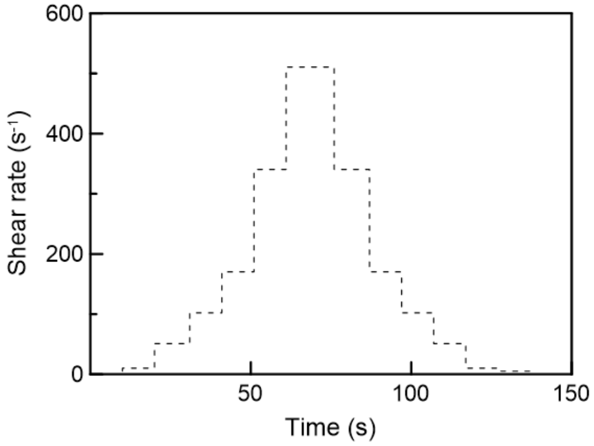

Figure 3.2 – The testing procedure of the viscosity measurements.

3.3.2.2. Squeeze flow

A servo-hydraulic MTS universal testing system, coupled with a 2.5 kN load cell, was used to conduct the squeeze-flow tests. The upper steel-made plate, fixed into the crosshead's load cell with a nominal diameter of 101 mm, was used to apply the load onto the fresh matrix. On the bottom surface, a plastic ring mold was placed on top of the steel plate, allowing the molding of the fresh paste in fixed initial dimensions of 101 x 10 mm (diameter and height). A displacement rate of 0.1 mm/s was used, up to a safety limit of 9 mm. The fresh matrices were tested immediately after the mixing procedure, comprising a maximum aging period of 5 min for assembling and testing.

3.3.3. Transient state properties

3.3.3.1. Vicat needle penetration tests

Vicat tests were performed following BS EN 196. This standard method was used to obtain the approximate setting time of the distinct geopolymer mixtures. Its accuracy to provide a proper hardening evaluation of the geopolymer materials was later evaluated and compared with more sophisticated methods, such as sonic strength and calorimetry.

3.3.3.2. Non-destructive compressive strength

A Chandler Ultrasonic Cement Analyzer (UCA) equipment was used to evaluate the sonic strength evolution of the different geopolymeric pastes from the initial molding time up to 48h. Additional temperature and pressure were not applied so that the constant temperature of 22 ºC was maintained during all tests to simulate regular molding conditions. This technique was able to provide an initial setting time, followed by a continuous profile of non-destructive compressive strength as a function of time by measuring the transit time of an acoustic signal. This correlation is made based on empirical formulations from the software’s library, which were able to accurately assess the geopolymer conditions.

3.3.4. Chemical properties

3.3.4.1. Calorimetry

The heat of reaction and heating rates were obtained by using an isothermal calorimeter I-Cal 4000 HPC (Calmetrix) at 25 ºC. The samples were previously mixed and placed inside each container in approximate amounts of 60 g. The experiments were performed three times for each geopolymer variation during the first 24 h of curing.

3.3.4.2. SAM and HCl extraction

To monitor and compare the amounts of unreacted precursors and calcium phases in each matrix variation, hydrochloric acid (HCl) and salicylic acid/methanol (SAM) extractions were performed. Initially, 14-days cured samples were crushed and grounded into fine powders (~75 µm) and kept sealed at room temperature for a week. SAM extraction was firstly performed, to potentially remove the calcium phases present in each type of geopolymer. For this, the samples were mixed with salicylic acid and methanol using a mass ratio of 1:6:40 and then agitated in a shaking table for 1 h, followed by filtration (0.45 µm Buchner filter) with periodic methanol washing, separating the insoluble residues. The samples were dried for 24 h at 100 ºC and their mass was recorded and compared to the before extraction values.

After this process, the samples underwent further treatment by hydrochloric acid (HCl) extraction to dissolve the aluminosilicate gel, leaving only the unreacted precursors. For this, one part of acid was diluted in 20 parts of deionized water, followed by the addition of 250 mL of HCl for every 1g of sample. Then, the mixture was stirred for 3 h on a shaking table, after which it was filtered and dried, allowing proper measurement.

3.3.5. Hardened thermal properties

3.3.5.1. Destructive tests

A servo-hydraulic MTS universal testing system with a load capacity of 500 kN was used to obtain the compressive strength of all GP matrices presented previously. The destructive tests were conducted in curing ages of 24h, 48h, 72h, and 7, and 14 days, to establish its evolution through a wide hardening period, while also allowing a proper comparison with the non-destructive results. Additionally, their mechanical properties were evaluated immediately after exposure to 100/250/500/750 ºC for 1 hour of heating in an electric furnace from Memmert GmbH + Co. Three cylindrical specimens were tested for each variation under a displacement-controlled rate of 0.5 mm/min. The deformation values were obtained from the readings of two linear variable displacement transducers (LVDT) attached to the sides of the specimens through an acrylic setup specially designed for this purpose. This measurement allowed Young’s modulus values to be accurately measured throughout the test.

3.4. Results and discussion

3.4.1. Materials characterization

Figure 3.3 presents the morphological parameters obtained for the varied precursors' materials throughout the scanning of optical static images of more than 10,000 particles for each variation. From the diameter distribution it is possible to observe that the peak value increased in order from BFS, MK_{LR}, MK_{HR}, and FA, i.e., BFS presented the lowest average diameter and FA the highest. All the materials except FA presented greater contents in lower diameter values up to 10 µm, while FA readings occurred mainly from 0.5 to 50 µm, meaning that MK_{LR},

MK_{HR}, and BFS have finer particles. This difference may play a role in the reactivity and rheological properties of the geopolymer materials [36]. The other morphological parameters showed similar trends for all materials, with a greater difference observed for MK_{HR}, where diminished values of aspect ratio and circularity were found, because of its greater particle elongation, meaning that MK_{LR}, BFS, and FA particles present a flatter and more circular geometry.

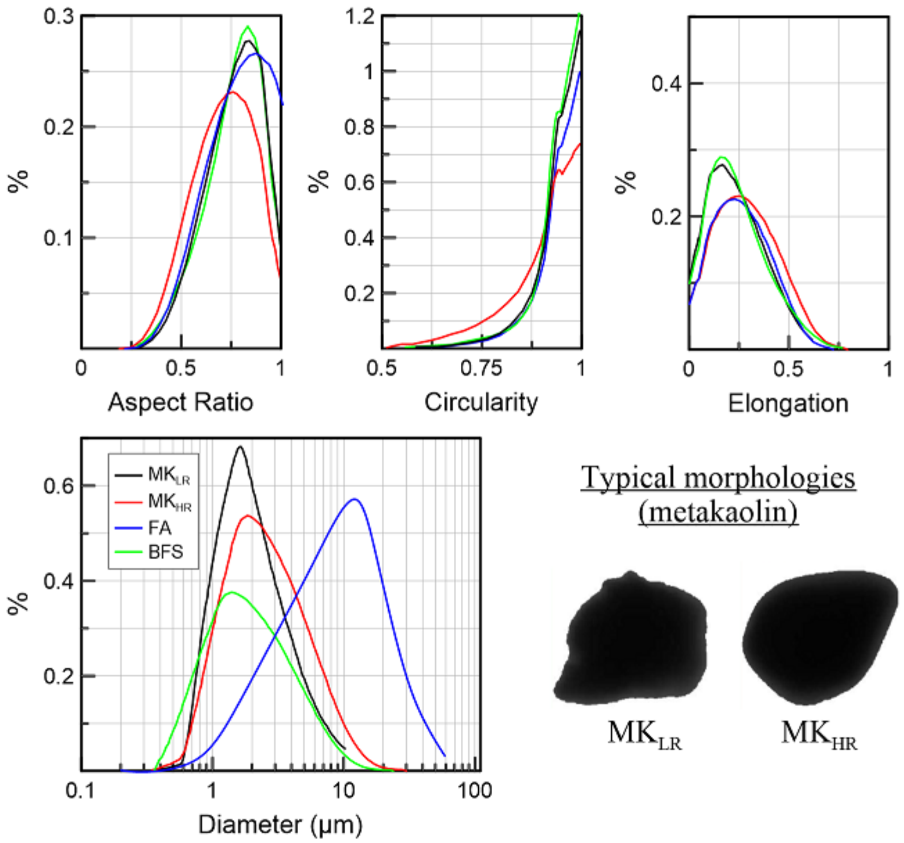

Figure 3.3 – Morphological parameters of the precursors' materials.

The diffractograms of all four precursors are shown in Figure 3.4a, while their quantitative mineralogical analysis is presented in Table 3. From the curves, it is possible to observe higher crystalline phases occurring for MK_{LR}, with quartz (SiO_2) and kaolinite ($Al_2Si_2O_5(OH)_4$) as the main contaminants, due to the presence of impurities and incomplete kaolinite calcination, respectively. Opposed to that, an enhanced amourphicity was found for MK_{HR}, i.e., higher purity, due to distinctions in the geological formation, extraction, and calcination processes between these two metakaolins. This statement is corroborated through the Rietveld mineralogical results in Table 3.3, showing the percentages by mass, where 33% of total crystallinity was found for MK_{LR}, opposed to only 2.6% found for MK_{HR}, thus justifying its nomenclature (highly reactive). Still, broad humps centered at 15-35º 2θ can be found for both aluminosilicate precursors, reflecting their intrinsic glassy structure.

The diffractogram obtained for FA also indicates a semi-crystalline trend, being this slightly more amorphous than MK_{LR}, with a broad hump at 15-30º 2θ. The main crystalline phases mullite ($2Al_2O_3SiO_2$), quartz (SiO_2), and hematite (Fe_3O_4) occur in 24.2% of the FA total mass. In opposition to this, the BFS sample did not present any crystalline portion, with its hump centered at 30º 2θ, being thus totally amorphous, as a possible result of an adequate cooling during its production. Such distinctions between both alternative precursors tend to significantly modify the geopolymer properties in both fresh and hardened states, which will be further investigated throughout this paper.

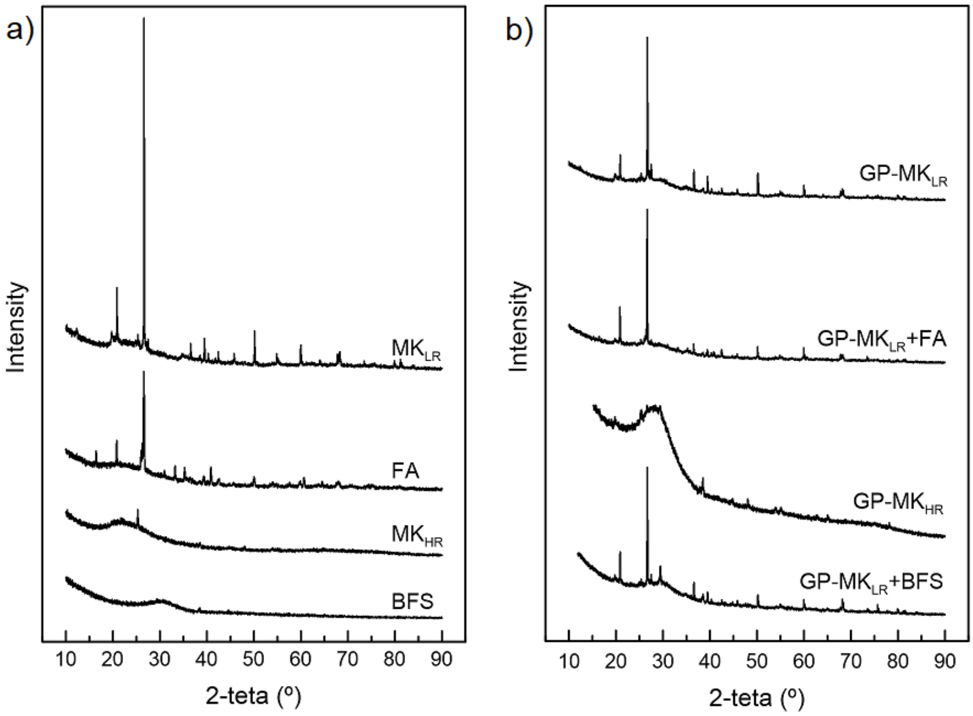

Figure 3.4 – Diffractograms obtained for all MK_{LR}, MK_{LR}+FA, MK_{LR}, and MK_{LR}+BFS (a) precursors, and (b) synthesized geopolymers.

When evaluating the diffractogram arrangements of the geopolymer mixtures in Figure 3.4b, it is possible to observe a typical change to the geopolymeric amorphous hump, occurring now between 25-40º 2θ for all samples, being more pronounced for mixtures containing MK_{HR} and MK_{LR}+BFS, thus suggesting higher degrees of geopolymerization due to their precursors increased amorphicity. It is interesting, however, to note that all the crystalline portions were reduced compared to the values obtained for the precursor materials in Table 3.3, indicating possibly a partial reactivity of their crystalline phases, coupled with the lower crystallinity of the alternative precursors (FA and BFS), that when combined with MK_{LR}, increase its amorphous portion and reactivity, thus suggesting an advantage in the combined use in geopolymer synthesis. Once again, the geopolymer manufactured with MK_{HR} demonstrated an increased amorphicity.

Table 3.3 – Mineralogical analysis of the varied precursors and GP matrices.

Material [%]	Precursors				Geopolymers			
	MK_{LR}	BFS	FA	MK_{HR}	MK_{LR}	MK_{LR}+BFS	MK_{LR}+FA	MK_{HR}
Crystalline	33.0	-	24.2	2.6	12.2	5.3	6.5	1.5
Amorphous	67.0	100.0	75.8	97.4	87.8	94.7	93.5	98.5
Total	100.0							
Crystalline phases								
Quartz	20.0	-	5.0	1.6	7.4	1.9	2.6	1.2
Calcite	-	-	-	-	-	3.4	-	-
Mullite	-	-	17.6	-	-	-	1.6	-
Hematite	-	-	1.4	-	-	-	-	-
Kaolinite	7.7	-	0.2	1.0	1.2	-	0.7	0.3
Others	5.3	-	-	-	3.6	-	2.3	-

3.4.2. Fresh state properties

The viscosity measurements are presented in Figure 3.5 and Table 3.4. The shear stress and shear rate data were recorded and fitted to a Bingham model described by the following equation [37]:

$$\tau = \tau_0 + \eta\gamma$$

where τ and τ_0 correspond to the shear stress and yield stress, while γ is the shear rate and η is the plastic viscosity associated with the resistance to continuous flow.

Table 3.4 – Viscosity measurements of the varied GP matrices.

GP material	MK$_{LR}$	MK$_{LR}$+BFS	MK$_{LR}$+FA	MK$_{HR}$
Yield stress [Pa]	6.43	1.18	2.43	1.53
Plastic viscosity [Pa·s]	1.49	1.01	0.68	0.17

The yield stress is related to the minimum shear stress capable of initiating the flow and deformation [38-40], through the adhesive and frictional forces between the liquids and particles, being thus dependent on their packing density and morphology [39]. In this study, the use of distinct precursors, and consequently varied WG combinations, resulted in different flow curves, as shown in Figure 3.5. In this sense, the results demonstrate superior values of Yield stress for MK$_{LR}$, reaching 6.43 Pa, opposed to the 2.43, 1.53, and 1.18 Pa, found for MK$_{LR}$+FA, MK$_{HR}$, and MK$_{LR}$+BFS, respectively. Here, the portion of unreacted particles and the difference in particle sizing seems to be of importance, since MK$_{LR}$ containing higher unreacted phases presented higher frictional forces, followed by MK$_{LR}$+FA containing a blend of broader particles sizes, compared to more regular morphologies of MK$_{LR}$+BFS and MK$_{HR}$. However, it is worth emphasizing that the adhesiveness of the manufactured WGs for each GP composition may also act significantly in the rheology of the paste, as a combined factor along with the particle's properties, which need to be assessed in a further study regarding relative viscosities (between the geopolymer pastes and WG).

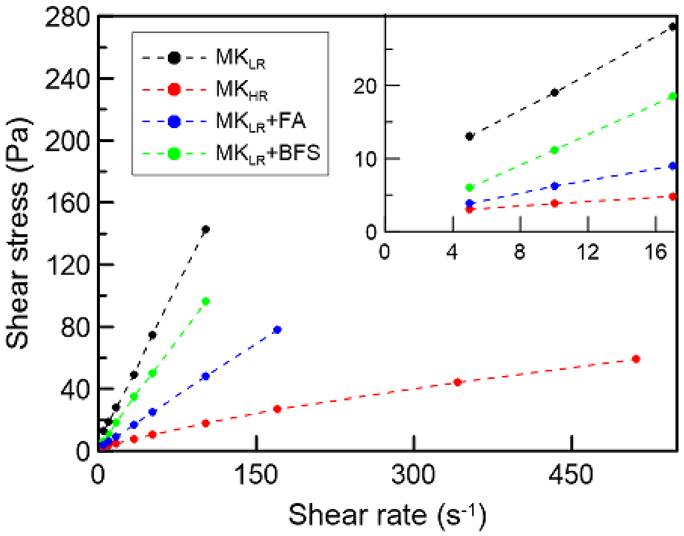

Figure 3.5 – Flow curves of the geopolymer matrices made from MK$_{LR}$, MK$_{LR}$+BFS, MK$_{LR}$+FA, and MK$_{HR}$.

The plastic viscosity (η) is also related to the friction of the particles with the liquid molecules [41], i.e., precursors and WG, also known as flow resistance, indicating the number of microstructures resisting to flow within a material [41]. Higher values of plastic viscosity were found for MK_{LR}, MK_{LR} +BFS, and MK_{LR} +FA, reaching 1.49, 1.01 Pa·s, and 0.68 Pa·s, respectively, while a diminished value of 0.17 Pa·s for MK_{HR}. This phenomenon can be partially attributed to the higher amount of unreacted quartz particles (SiO_2) present in MK_{HR}, creating mechanical frictional constraints on the fluidity of the matrix, and also partially to the silicate content in each type of WG, as presented in Table 2. The latter is known [38,42] to elevate the H_2O demand due to higher dissolution rates, thus modifying the GP flowability. Increased H_2O contents as observed for MK_{HR}, however, tend to prevent the friction of the fine particles, flowing at lower shear stresses, possibly affecting its strength development [41], therefore justifying its diminished response. Higher portions of H_2O can also be related to the MK_{LR}+FA composition presented in Table 2, therefore reinforcing the previous statement.

As an additional consistency evaluation, Figure 3.6 presents the squeeze-flow test results of the varied GP matrices. The (a) load-displacement curves show a typical squeeze-flow profile distinguished into three distinct regions, as presented in (b), and fully discussed in previous works [43,44].

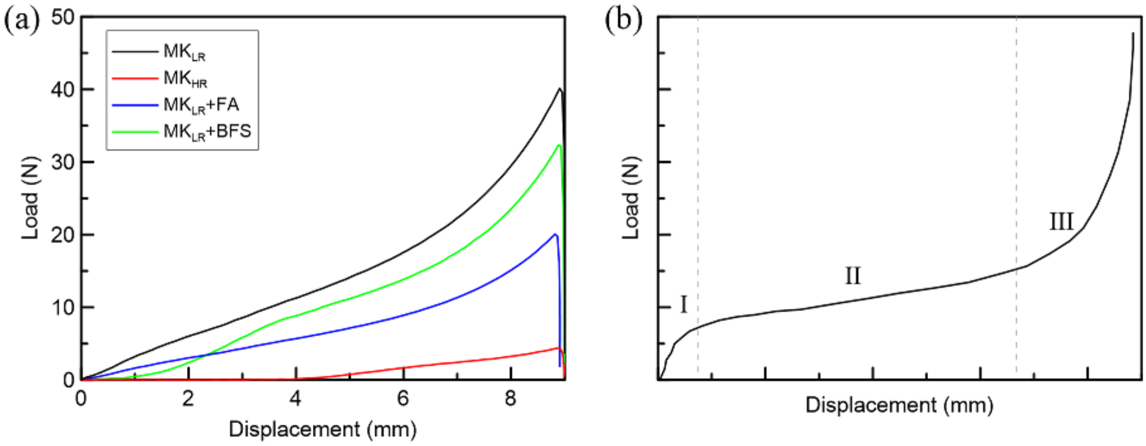

Figure 3.6 – (a) Squeeze flow curves of the different GP matrices, and (b) a typical profile [38,39].

Region I refer to the elastic deformation, related to the material's yield stress, that in small deformations behaves like a solid [43,44]. At this point, only MK_{LR}

presented a clear distinguished region I, due to its enhanced yield stress found previously, related to its higher number of unreacted particles combined with its assumed WG enhanced viscosity. In region II the increase in displacement results in a linear increase in elongational and shear radial deformations at small load variations, flowing into a plastic or viscous deformation, leading to region III, referred to as strain hardening with small increases in deformation despite the fast load enhancement [43,44]. All the GP variations, except MK_{HR}, presented an extended viscous flow stage at small loadings, due to their enhanced plastic viscosity. Their transition to the strain hardening region occurred only at the very end of the test, i.e., at larger displacements, visible through a shift in the orthogonal orientation of the curves. This extended viscous flow behavior is typically favorable in the application of mortars, allowing adequate spreading/regularization under increased displacements [45,46]. MK_{LR} presented the highest loads, followed by MK_{LR}+BFS and MK_{LR}+FA, with MK_{HR} demonstrating an excessive flowability, preventing the typical viscous behavior to occur. All GP responses are related to the viscosity parameters presented previously, with a gradual trend occurring from more to less viscous matrices. The strain-hardening stage is highly associated with the friction of the particles and an increase in solid concentration due to liquid-solid segregation [46]. At such displacement rate, no evidence of phase-segregation occurrence was recorded, possibly due to the small particle size distribution of both reference matrix MK_{LR} and combined replacements with BFS and FA.

3.4.3. Transient state properties

Figure 3.7 presents the monitoring of the setting times of each GP mixture using the Vicat needle method. None of the matrices provided any resistance to penetration neither immediately after nor within a few hours after mixing. This is a result of the cooling of the alkali solutions before mixing [47], slowing the geopolymer reactions, allowing a more extensive fresh state period to arise. As the geopolymerization process occurs, the microstructure develops, increasing the resistance to the penetrating needle, allowing estimated monitoring of the strength/hardening processes. However, each matrix composition demonstrated different setting times, which can be estimated from the curves. The reference MK_{LR} reached an earlier initial setting time, after only 4.8 hours of curing, compared to 6.0, 8.0, and 8.5 hours found for the mixtures containing MK_{LR}+BFS, MK_{LR}+FA, and MK_{HR}, respectively. The times between the initial and final settings were also estimated, with MK_{HR} reaching the highest setting period of 6.5 hours, compared to diminished intervals of 4.5, 4.8, and 5.5 hours estimated for MK_{LR}, MK_{LR}+BFS, and MK_{LR}+FA variations. This retardment on the setting time of MK_{HR} is associated with a longer dissolution time, due to excessive silicate species within its WG [2,4] combined with a highly amorphous precursor, as discussed in the previous section, retarding its microstructure and strength development.

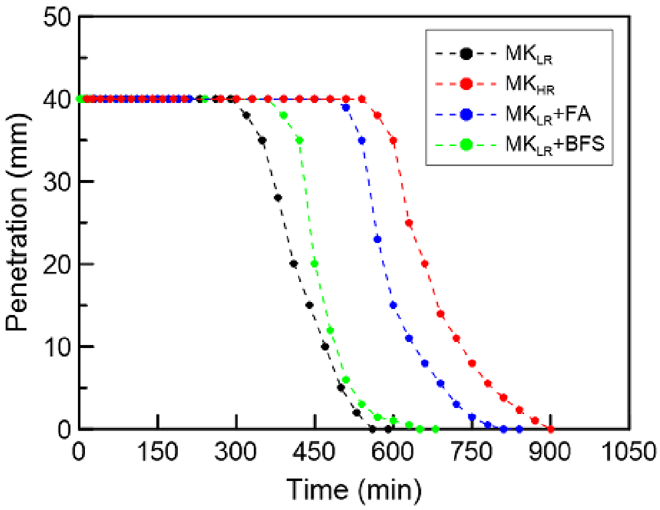

Figure 3.7 – Monitoring of the Vicat needle penetration for each geopolymer matrix.

Previous studies state that although being useful for estimation processes, the Vicat needle penetration test does not provide confident results regarding the hardening rate over time [47,48]. Such results are important parameters related to microstructural modifications, transport time, launching, finishing, and removal of formworks. The Ultrasonic Cement Analyzer (UCA) appears as a functional method to study the geopolymers transition from liquid to solid state [47], also allowing verification of the previous results found with the Vicat needle penetration tests. The apparatus used provided initial setting times and the consequent strength development up to 48 hours of curing, as shown in Figure 3.8.

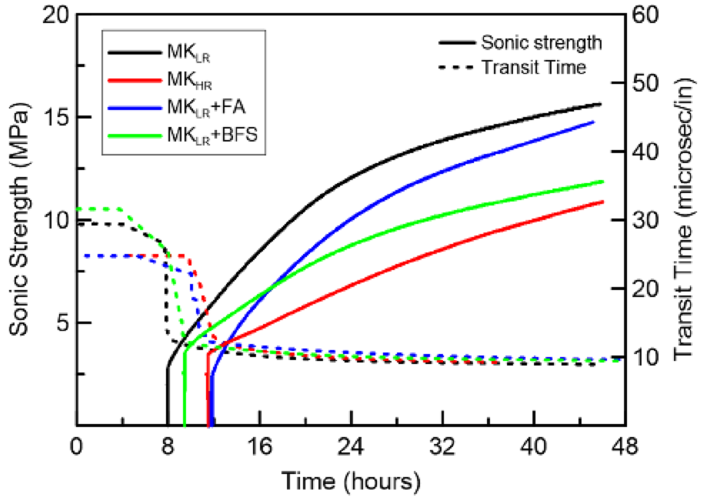

Figure 3.8 –Sonic strength and transit time values obtained from the different geopolymer matrices.

The curves show a similar trend with the one found with the Vicat penetration, recording setting times in the following order: MK_{LR}, MK_{LR}+BFS, MK_{LR}+FA, and MK_{HR}, after 8.0, 9.3, 11.5, and 11.6 hours, i.e., between the initial and final setting found with Vicat tests. This difference may be related to both apparatus calibration and accuracy [49], suggesting further analysis of the chemical and microstructural dependency through the heat released in the first hours. The small delay in the initial setting time may be also related to a retardment in gelation, resulting from the presence of small amounts of water on the upper surface of the pastes (necessary to perform the UCA tests) [50,51].

All the responses showed that the maximum rate of ultrasonic strength occurred on the first day. After 24 hours of curing, where MK_{LR} reached the highest compressive strength of 12.0 MPa, due to its faster dissolution rate, followed by MK_{LR}+FA (10.0 MPa), MK_{LR}+BFS (8.8 MPa), and MK_{HR} (6.8 MPa). This trend continued up to 48 hours, reaching then 15.6, 14.8, 11.9, and 10.9 MPa, respectively. It is worth noting, however, distinct strength gain rates in this short period, with enhanced values found for MK_{LR} and MK_{LR}+FA, with approximately 0.47 MPa/hour from setting time up to 24 hours, followed by a reduction at this midpoint to 0.15 MPa/hour up to 48 hours. MK_{LR}+BFS also underwent rate reductions at the test’s midpoint, while MK_{HR} maintained an almost constant rate of 0.20 MPa/hour throughout the test, once again related to a longer dissolution time, because of its increased amorphicity and reactivity. Smaller transit time values are usually related to diminished heat releases, also associated with lower viscosity modifications [52], which are in accordance with the results shown in the previous section, where MK_{HR} and MK_{LR}+FA presented lower viscosities, compared to MK_{LR} and MK_{LR}+BFS.

3.4.4. Chemical properties

Figure 3.9 presents the (a) cumulative heat of reaction and the (b) rates of heat flow of the varied geopolymer matrices, showing a similar lower trend for all GP variations, compared to usual cementitious binders [53]. The single exothermic peak emerges immediately after the mixture procedure, because of the dissolution of the precursors in the alkaline solution [54]. The cumulative heat and heat flow parameters of MK_{LR} are much higher than all the other variations, reaching 106.30 J/g and 1.45 mW/g, respectively. Its peak dropped also slowly compared to the other matrices. Both mechanisms are related to a faster chemical dissolution of this type of precursor during geopolymerization [54], occurring due to its lower amorphicity, as stated in XRD results. Opposite to this, MK_{HR} is formed by a great amount of active amorphous phase materials with a disruptive layer structure, containing high percentages of glassy phase materials [54,55], reaching thus only 102.25 J/g and 0.45 mW/g.

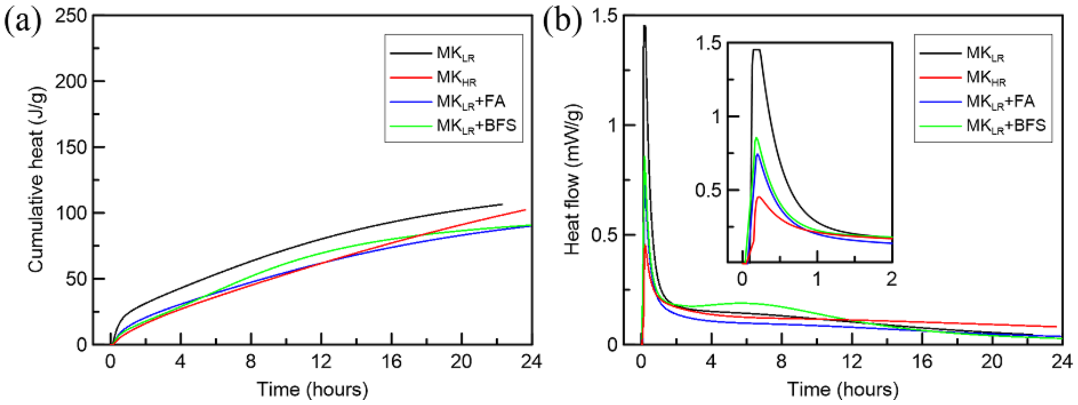

Figure 3.9 – (a) Cumulative heat and (b) heat flow of the distinct geopolymer matrices during the first 24 hours of curing.

The partial MK_{LR} substitutions with FA and BFS presented decreases in heat generation, with similar values of 90.60 J/g and 0.85 mW/g for MK_{LR}+BFS, and 89.85 J/g and 0.74 mW/g for MK_{LR}+FA. This kinetics endorse the results found in the previous section, where the incorporation of alternative precursors increases the MK_{LR} amorphicity. However, it was expected that the geopolymer containing portions of BFS would result in lower values compared to FA. This alteration is mainly attributed to the fact that BFS presents a much higher chemical activity than FA, modifying the reaction process due to increased calcium contents, which may result in similar/partial hydration processes, as occurs for cementitious binders [54,56], comprising the coexistence of a geopolymeric network and a calcium-based cement-like phase [56]. Also, the absence of a second peak for all the other variations suggests a diminished number of reaction products being formed after the first hour of curing [57], indicating a gradual geopolymerization process. Opposed to that, MK_{LR}+BFS shows a slightly visible second peak centered at 6 h, evidencing once again a late reaction process occurring due to calcium presence [56].

Adding to the calorimetry evaluation, two types of chemical extractions, based on salicylic acid in methanol (SAM) and hydrochloric acid (HCl), were used to separate the calcium-based phases and monitor the reactive part of the distinct geopolymer materials investigated in this study. Table 3.5 presents the quantitative chemical extraction.

Table 3.5 – Results of SAM and HCl extractions (given by mass %).

GP material	MK_{LR}	BFS	FA	MK_{HR}
Mass dissolved by SAM [%]	-	17.24	0.97	-
Unreacted particles left by HCl [%]	13.83	9.22	10.45	5.46

From the SAM extraction results, it is possible to observe, as expected, a higher calcium phase content for MK_{LR}+BFS materials, due to its secondary precursor chemical composition shown in Table 3.1. This information justifies the modified heat release observed previously, due to similarities found with cement-based binders, presenting recurring hydration processes, as discussed in previous works [58]. Additionally, MK_{LR}+FA binders demonstrated diminished calcium product content in Table 3.1, which may slightly affect their strength development. Both MK_{LR} and MK_{HR} did not record any calcium-phases amounts, due to their inherent aluminosilicate composition.

HCl extraction left unreacted portions of all materials studied. These portions are resultant from the (i) non-use of temperature in the curing regime and (ii) dissolution rates due to the amorphous and crystalline parts in the precursor, and to the alkali concentrations used [59]. Both promote great molecules agitation, and accelerate the reactions in high concentrations, increasing the solubility [60,61]. As expected from the XRD results, MK_{HR} demonstrated higher reactivity, followed by MK_{LR}+FA, MK_{LR}+BFS, and MK_{LR}, where the latter resulted also in increased crystalline phases obtained from Rietveld methodology.

3.4.5. Hardened properties

Figure 3.10 and Table 3.6 present the strength development through compressive tests with all geopolymer variations in curing periods of 24 h, 48 h, 72 h, 7 days, and 14 days. It is visible that a greater strength gain occurred for MK_{LR} in the first 24 hours, due to its faster dissolution, as evidenced previously, reaching higher compressive responses in all curing ages studied, up to an average of 68.1 MPa after 14 days. Additionally, the lower reactivity of MK_{LR} seems to be beneficial for compressive loadings, since the non-reacted particles may act as mechanical activators, such as fillers or particulate reinforcements [62]. The use of MK_{LR}+FA and MK_{HR} generated a gradual increase in all studied ages, due to a slower dissolution rate, with 9.7 and 7.8 MPa in the first 24 h, and an average of 38.5 and 39.1 MPa at 14 days. This late increased response found for MK_{HR} is due to its enhanced reactivity showed in XRD and HCl extraction results. MK_{LR}+BFS presented the lowest strength development up to 7 days, showing late strength gains up to 14 days (49.5 MPa) due to its calcium content, as expected and justified in the previous section.

These results also allow proper verification of the usability of the UCA test configuration parameters, since a maximum 1.5 MPa (MK_{HR}) difference was recorded comparing both non-destructive and destructive strength results, providing an acceptable error interval.

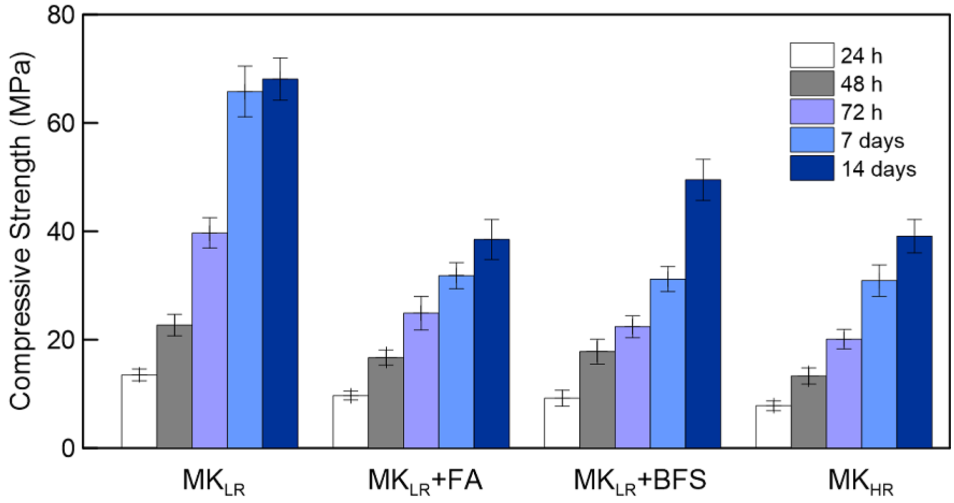

Figure 3.10 – Compressive strength development of all geopolymer variations in varied curing periods.

Table 3.6 – Compressive strength development of all geopolymer variations in distinct curing periods.

GP material	MK_{LR}					MK+FA				
	24h	48h	72h	7d	14d	24h	48h	72h	7d	14d
Compressive strength [MPa]	13.5 (1.1)	22.7 (2.0)	39.7 (2.8)	65.8 (4.7)	68.1 (3.9)	9.7 (0.8)	16.7 (1.4)	24.9 (3.1)	31.8 (2.4)	38.5 (3.7)
GP material	MK+BFS					MK_{HR}				
	24h	48h	72h	7d	14d	24h	48h	72h	7d	14d
Compressive strength [MPa]	9.2 (1.5)	17.8 (2.3)	22.4 (2.0)	31.2 (2.3)	49.5 (3.8)	7.8 (0.9)	13.3 (1.5)	20.1 (1.8)	30.9 (2.9)	39.1 (3.1)

Figure 3.11 and Table 3.7 present the results obtained with all geopolymer variations after exposure to varied elevated temperatures. It is possible to observe that from all the geopolymer materials studied, MK_{HR} presented an improved thermal residual behavior, compared to MK_{LR}, MK_{LR}+BFS, and MK_{LR} +FA. This enhanced performance can be attributed to its higher reactivity, which increases the homogeneity of the sample, regarding pore structure and particle agglomerations, reducing early damages to arise [19], reaching an average of 26.4 MPa at 500 ºC. This is opposed to all the other materials, that contain higher amounts of non-

reacted particles, inducing faster damage to occur [63], reaching 23.2, 21.5, and 13.8 MPa, for MK_{HR}, MK_{HR}+BFS, and MK_{HR}+FA, at similar temperature ranges.

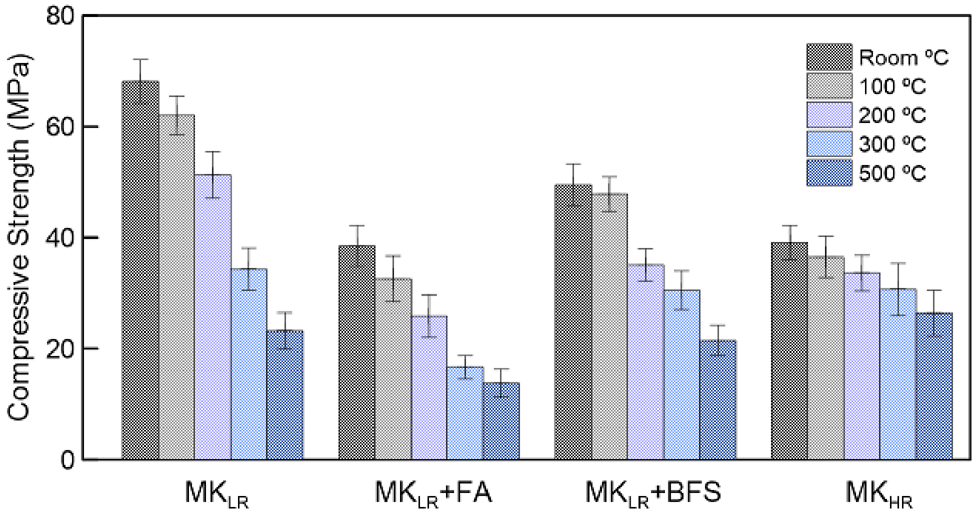

Figure 3.11 –Compressive strength of all geopolymer variations after exposure to elevated temperatures.

Table 3.7 – Compressive strength of all geopolymer variations after exposure to varied elevated temperatures of 100 °C, 200 °C, 300 °C, and 500 °C at 14 days.

GP material	MK_{LR}					MK+FA				
	RT	100 °C	200 °C	300 °C	500 °C	RT	100 °C	200 °C	300 °C	500 °C
Compressive strength [MPa]	68.1 (3.9)	62.0 (3.5)	51.3 (4.2)	34.3 (3.8)	23.2 (3.3)	38.5 (3.7)	32.6 (4.1)	25.9 (3.8)	16.7 (2.1)	13.8 (2.5)
GP material	MK+BFS					MK_{HR}				
	RT	100 °C	200 °C	300 °C	500 °C	RT	100 °C	200 °C	300 °C	500 °C
Compressive strength [MPa]	49.5 (3.8)	47.8 (3.1)	35.1 (2.9)	30.5 (3.5)	21.5 (2.7)	39.1 (3.1)	36.5 (3.7)	33.6 (3.2)	30.7 (4.7)	26.4 (4.1)

In general, it is visible residual strength reductions for all temperature increments. The diminished reduction found at 100 °C for all variations is known to be a result of the non-microstructural changes related to free-water evaporation [64,65]. From 100 °C to 300 °C the dehydration continues, now due to the loss of chemically bound water, possibly evolving to early crack formations (thermal shrinkage) due to continuous water losses [19,64,65]. In sequence, up to 500 ºC, the gel and possible calcium-phases (MK_{LR}+BFS) start to deteriorate, along with unreactive quartz expansion, resulting in significant strength reductions to MK_{LR} and MK_{LR}+FA, due to its higher alkalinity and quartz content, and differences in particle sizes (MK_{LR} and FA), possibly affecting their porous structure in both room and high-temperature exposures [66]. To further justify these mechanical results, extra XRD analysis with Rietveld quantification was conducted on samples exposed to temperature and are presented in Figure 3.12 and Table 3.8.

The thermal exposures increased the formation of stable crystalline phases up to 300 ºC for all geopolymer materials, except the one containing BFS, being more preponderantly to MK_{LR}. This is in accordance with previous studies [67], stating that the formation of such phases in free calcium geopolymers was found to induce thermal stresses within the nanoporous material, deteriorating its strength, causing thermal expansion of the quartz particles and mismatches with the amorphous portion, which was visually more drastic to MK_{LR} in the previously discussed compressive results. It is worth noticing the lower MK_{HR} crystalline formation upon heating, remaining mostly amorphous, guarantying, and justifying its increased mechanical stability. From all the geopolymer variations, MK_{LR}+BFS was the only one presenting calcite formation in this temperature range, due to the initiation of the calcium portion deterioration, with higher decomposition and lower phase formation at 500 ºC, thus partially reducing its mechanical performance.

In general, all the geopolymer materials presented suitable mechanical strength evolutions at room temperature, with viscosity and setting time variations depending mostly on the precursor used, i.e., their amorphous and crystalline portions, and their correspondent WG compositions. Due to its increased flowability, it is expected that MK_{HR} can be more efficiently used as the main binder designed to be reinforced with higher portions of particulate and fiber reinforcements, being also thermally stable upon 500 ºC. MK_{LR}+FA and MK_{LR}+BFS presented intermediate responses regarding rheology and mechanical capacity, where similar to MK_{HR} applications could be considered for the first, and late strength demands for the latter. MK_{LR}, despite presenting extremely higher viscosity, reaches outstanding initial and late strengths compared to the other variations, being thus more efficient for mechanical demands that do not require thermal resistances.

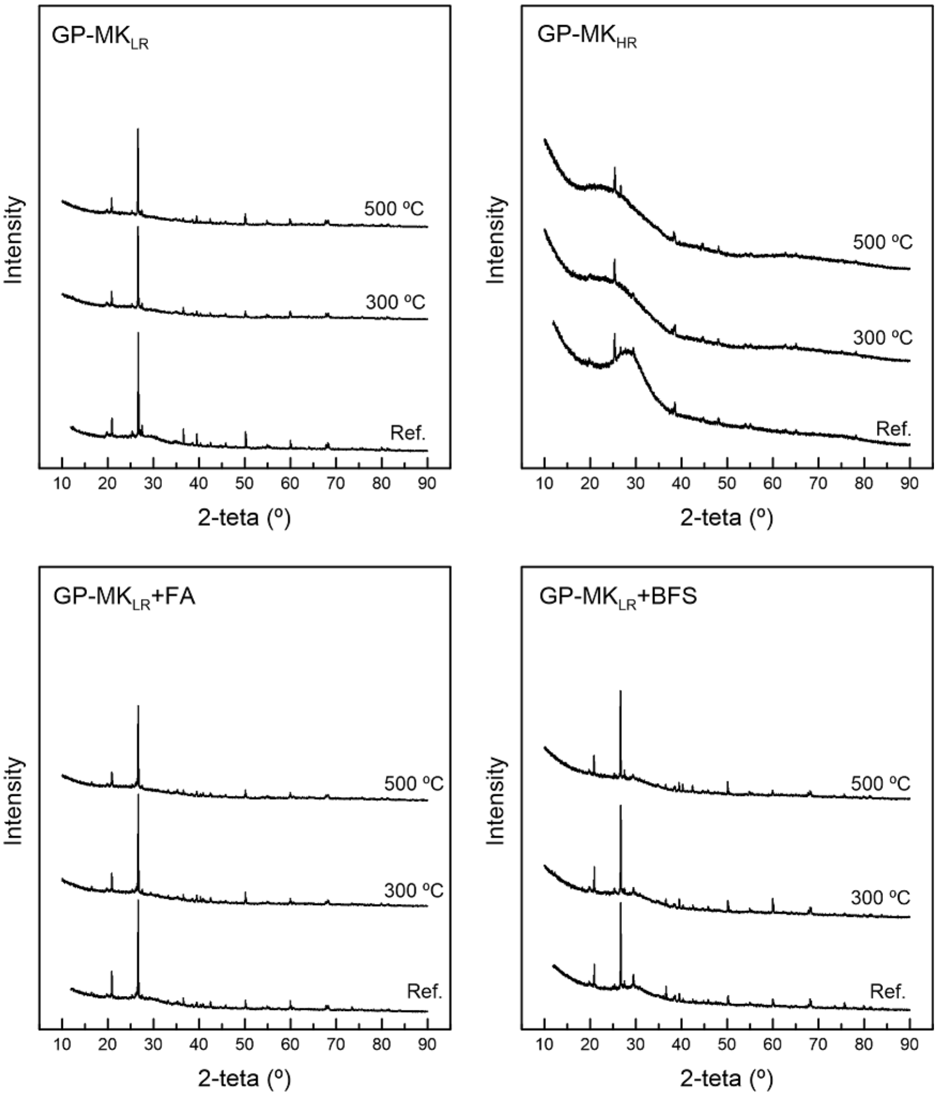

Figure 3.12 –Diffractograms obtained for all MK$_{LR}$, MK$_{LR}$+FA, MK$_{LR}$, and MK$_{LR}$+BFS geopolymers at room temperature, and after exposure to 300 ºC and 500 ºC.

Table 3.8 – Mineralogical analysis of the varied precursors and GP matrices.

Geopolymer [%]	MK_{LR}			MK_{HR}		
	Ref.	300 °C	500 ºC	Ref.	300 °C	500 ºC
Crystalline	12.2	18.3	17.4	1.5	3.8	5.9
Amorphous	87.8	81.7	82.6	98.5	96.2	94.1
Total	100.0					
Crystalline phases						
Quartz	7.4	9.3	8.8	1.2	3.2	4.8
Kaolinite	1.2	0.4	0.3	0.3	0.2	0.4
Pseudo-Wollastonite		-	-	-	-	-
Others	3.6	8.6	8.3	-	0.4	0.7
Geopolymer [%]	MK_{LR}+FA			MK_{LR}+BFS		
	Ref.	300 °C	500 ºC	Ref.	300 °C	500 ºC
Crystalline	6.5	8.8	10.9	5.3	11.4	4.4
Amorphous	93.5	91.2	89.1	94.7	88.6	95.6
Total	100.0					
Crystalline phases						
Quartz	2.6	2.9	3.8	1.9	2.9	2.2
Calcite	-	-	-	3.4	8.1	1.8
Mullite	1.6	1.7	2.6	-	-	-
Hematite	-	0.2	0.4	-	-	-
Kaolinite	0.7	1.1	1.2	-	-	-
Pseudo-Wollastonite	0.2	0.4	0.6	-	-	-
Others	2.1	2.4	1.3	-	0.4	-

3.5. Conclusions

This work evaluated experimental data regarding the use of varied aluminosilicate precursors in a well-known geopolymer design with distinctions regarding viscosity, setting times, heat releases, and strength evolution, over time and temperature, basing the justifications on chemical parameters. A low reactive metakaolin (MK_{LR}), and partial substitutions made with fly-ash (FA) and blast furnace slag (BFS) were used and compared to a high-reactive metakaolin (MK_{HR}). In general, the precursors' inherent amorphous and crystalline parts were the main responsible for the distinctions observed on each investigation, as well as their WG constitutions, since each geopolymer variation required distinct amounts of SiO_2, NaOH, and H_2O, to achieve equilibrium.

MK_{LR} presented high levels of crystallinity, 33% for the precursor and 12.2% for the geopolymer, being the crystal phases related to the presence of impurities (quartz) and incomplete kaolinite calcination. On its fresh state, reached higher Yield stress and plastic viscosity (6.43 Pa and 1.49 Pa.s), due to its particles properties (impurities) and WG viscosity, being confirmed by squeeze flow tests. Due to its diminished reactivity, assumed by XRD results and confirmed by SAM and HCl extractions, a faster dissolution rate occurred when in presence of high shear mixing with the alkali solution, evolving to a faster setting time, both under Vicat needle penetration tests and UCA evaluations. These were substantial parameters in achieving the highest compressive behavior of all the geopolymer materials at 14 days (68.1 MPa), combining the faster dissolution with the quartz portions acting as fillers. However, MK_{LR} was not suitable in presence of thermal stresses, reducing its reference strength by 65% when exposed to 500 ºC. This was, once again, due to the unreacted particles, which enhanced the damage evolution through thermal expansion.

The partial substitutions of MK_{LR} made by FA and BFS increased the geopolymers flowability, due to distinctions in blended particle sizes for the first, and higher levels of reactive portions for both, occurring in slower dissolution rates than MK_{LR}, reaching thus increased setting times. In fact, the BFS substitution added a new mechanism to the binder, modifying the synthetic parameters now containing calcium parts, resulting in partial hydration products, as occurs for cementitious material, evidenced by calorimetry, and SAM extractions, being highly pronounced on the strength evolution over time, with slower initial strength at 24 h (9.2 MPa), evolving to late strength development at 14 days (49.5 MPa).

MK_{HR} demonstrated a stable, yet slow, rate of dissolution, due to its mainly amorphous structure, reaching thus a slow strength development and heat release. This enhanced reactivity was also confirmed by XRD results and HCl extractions, acting mainly on the quality of the geopolymer binder, which in its fresh state present the highest flowability, being then able to incorporate particles and fibers in a more effective manner than the other geopolymer counterparts. Additionally, it is inherently more thermally stable, which may be beneficial in extreme temperature conditions.

3.6. References

[1] Davidovits, J. (2013). Geopolymer cement. A review. Geopolymer Institute, Technical papers, 21, 1-11.

[2] Buruberri, L. H., Tobaldi, D. M., Caetano, A., Seabra, M. P., & Labrincha, J. A. (2019). Evaluation of reactive Si and Al amounts in various geopolymer precursors by a simple method. Journal of Building Engineering, 22, 48-55.

[3] Hajimohammadi, A., & van Deventer, J. S. (2016). Dissolution behaviour of source materials for synthesis of geopolymer binders: a kinetic approach. International Journal of Mineral Processing, 153, 80-86.

[4] Duxson, P., Fernández-Jiménez, A., Provis, J. L., Lukey, G. C., Palomo, A., & van Deventer, J. S. (2007). Geopolymer technology: the current state of the art. Journal of materials science, 42(9), 2917-2933.

[5] Zhang, H. Y., Kodur, V., Qi, S. L., Cao, L., & Wu, B. (2014). Development of metakaolin–fly ash based geopolymers for fire resistance applications. Construction and Building Materials, 55, 38-45.

[6] Assi, L., Carter, K., Deaver, E. E., Anay, R., & Ziehl, P. (2018). Sustainable concrete: Building a greener future. Journal of cleaner production, 198, 1641-1651.

[7] Rovnaník, P., Rovnanikova, P., Vyšvařil, M., Grzeszczyk, S., & Janowska-Renkas, E. (2018). Rheological properties and microstructure of binary waste red brick powder/metakaolin geopolymer. Construction and Building Materials, 188, 924-933.

[8] Sandanayake, M., Gunasekara, C., Law, D., Zhang, G., & Setunge, S. (2018). Greenhouse gas emissions of different fly ash based geopolymer concretes in building construction. Journal of cleaner production, 204, 399-408.

[9] Pimraksa, K., Chindaprasirt, P., Rungchet, A., Sagoe-Crentsil, K., & Sato, T. (2011). Lightweight geopolymer made of highly porous siliceous materials with various Na2O/Al2O3 and SiO2/Al2O3 ratios. Materials Science and Engineering: A, 528(21), 6616-6623.

[10] De Silva, P., & Sagoe-Crenstil, K. (2009). The role of Al2O3, SiO2 and Na2O on the amorphous-> Crystalline phase transformation in geopolymer systems. Journal of Australian Ceramic Society, 63-71.

[11] Wang, R., Wang, J., Dong, T., & Ouyang, G. (2020). Structural and mechanical properties of geopolymers made of aluminosilicate powder with different

SiO2/Al2O3 ratio: Molecular dynamics simulation and microstructural experimental study. Construction And Building Materials, 240, 117935.

[12] Trochez, J. J., Mejía de Gutiérrez, R., Rivera, J., & Bernal, S. A. (2015). Synthesis of geopolymer from spent FCC: Effect of SiO2/Al2O3 and Na2O/SiO2 molar ratios. Materiales de Construcción, 65(317), e046.

[13] Kriven, W. M., Bell, J. L., & Gordon, M. (2003). Microstructure and microchemistry of fully-reacted geopolymers and geopolymer matrix composites. Ceramic Transactions, 153(1994).

[14] Barbosa, V. F., MacKenzie, K. J., & Thaumaturgo, C. (2000). Synthesis and characterisation of materials based on inorganic polymers of alumina and silica: sodium polysialate polymers. International Journal of Inorganic Materials, 2(4), 309-317.

[15] Rahier, H., Van Mele, B., Biesemans, M., Wastiels, J., & Wu, X. (1996). Low-temperature synthesized aluminosilicate glasses. Journal of Materials Science, 31(1), 71-79.

[16] Trindade, A. C. C., de Andrade Silva, F., & Kriven, W. M. (2021). Mechanical behavior of K-geopolymers reinforced with silane-coated basalt fibers. Journal of the American Ceramic Society, 104(1), 437-447.

[17] Trindade, A. C. C., Curosu, I., Liebscher, M., Mechtcherine, V., & de Andrade Silva, F. (2020). On the mechanical performance of K-and Na-based strain-hardening geopolymer composites (SHGC) reinforced with PVA fibers. Construction and Building Materials, 248, 118558.

[18] Khan, M. Z. N., Hao, Y., & Hao, H. (2019). Mechanical properties and behaviour of high-strength plain and hybrid-fiber reinforced geopolymer composites under dynamic splitting tension. Cement and Concrete Composites, 104, 103343.

[19] Trindade, A. C. C., Liebscher, M., Curosu, I., de Andrade Silva, F., Mechtcherine, V. (2021). Influence of elevated temperatures on the residual and quasi in-situ flexural strength of strain-hardening geopolymer composites (SHGC) reinforced with PVA and PE fibers. Composites Part B, under submission.

[20] Ghosh, K., & Ghosh, P. (2012). Effect Of Na2O/Al2O3, SiO2/Al2O3 and w/b ratio on setting time and workability of fly ash based geopolymer. International Journal of Engineering Research and Applications, 2(4), 2142-2147.

[21] Bhowmick, A., & Ghosh, S. (2012). Effect of synthesizing parameters on

workability and compressive strength of fly ash based geopolymer mortar. Int. J. Civ. Struct. Eng, 3(1), 168-177.

[22] Szabó, R., & Mucsi, G. (2019). Effect of SiO2, Al2O3 and Na2O content and fly ash fineness on the structure and mechanical properties of fly ash based geopolymer. Recycling and Sustainable Development, 12(1), 61-68.

[23] Güllü, H., Cevik, A., Al-Ezzi, K. M., & Gülsan, M. E. (2019). On the rheology of using geopolymer for grouting: A comparative study with cement-based grout included fly ash and cold bonded fly ash. Construction and Building Materials, 196, 594-610.

[24] Alnahhal, M. F., Kim, T., & Hajimohammadi, A. (2021). Distinctive rheological and temporal viscoelastic behaviour of alkali-activated fly ash/slag pastes: A comparative study with cement paste. Cement and Concrete Research, 144, 106441.

[25] Provis, J. L. (2018). Alkali-activated materials. Cement and Concrete Research, 114, 40-48.

[26] Luukkonen, T., Abdollahnejad, Z., Yliniemi, J., Kinnunen, P., & Illikainen, M. (2018). One-part alkali-activated materials: A review. Cement and Concrete Research, 103, 21-34.

[27] Bernal, S. A., Rodríguez, E. D., de Gutiérrez, R. M., Gordillo, M., & Provis, J. L. (2011). Mechanical and thermal characterisation of geopolymers based on silicate-activated metakaolin/slag blends. Journal of materials science, 46(16), 5477-5486.

[28] Alcamand, H. A., Borges, P. H., Silva, F. A., & Trindade, A. C. C. (2018). The effect of matrix composition and calcium content on the sulfate durability of metakaolin and metakaolin/slag alkali-activated mortars. Ceramics International, 44(5), 5037-5044.

[29] Trindade, A. C. C., Silva, F. D. A., Alcamand, H. A., & Borges, P. H. R. (2017). On the mechanical behavior of metakaolin based geopolymers under elevated temperatures. Materials Research, 20, 265-272.

[28] Assaad, J. J., & Saba, M. (2020). Suitability of Metakaolin-Based Geopolymers for Masonry Plastering. ACI Materials Journal, 117(6), 269-279.

[29] Ahdaya, M., & Imqam, A. (2019). Fly ash Class C based geopolymer for oil well cementing. Journal of Petroleum Science and Engineering, 179, 750-757.

[30] Hwalla, J., Saba, M., & Assaad, J. J. (2020). Suitability of metakaolin-based

geopolymers for underwater applications. Materials and Structures, 53(5), 1-14.

[31] Duxson, P. S. W. M., Mallicoat, S. W., Lukey, G. C., Kriven, W. M., & van Deventer, J. S. (2007). The effect of alkali and Si/Al ratio on the development of mechanical properties of metakaolin-based geopolymers. Colloids and Surfaces A: Physicochemical and Engineering Aspects, 292(1), 8-20.

[32] Trindade, A. C. C., Heravi, A. A., Curosu, I., Liebscher, M., de Andrade Silva, F., & Mechtcherine, V. (2020). Tensile behavior of strain-hardening geopolymer composites (SHGC) under impact loading. Cement and Concrete Composites, 113, 103703.

[33] Rahmiati, T., Azizli, K. A., Man, Z., Ismail, L., & Nuruddin, M. F. (2015). Effect of solid/liquid ratio during curing time fly ash based geopolymer on mechanical property. In Materials science forum (Vol. 803, pp. 120-124). Trans Tech Publications Ltd.

[34] Vitola, L., Pundiene, I., Pranckeviciene, J., & Bajare, D. (2020). The Impact of the Amount of Water Used in Activation Solution and the Initial Temperature of Paste on the Rheological Behaviour and Structural Evolution of Metakaolin-Based Geopolymer Pastes. Sustainability, 12(19), 8216.

[35] Protasio, F. N. M., de Avillez, R. R., Letichevsky, S., & de Andrade Silva, F. (2021). The use of iron ore tailings obtained from the Germano dam in the production of a sustainable concrete. Journal of Cleaner Production, 278, 123929.

[36] Nath, S. K., & Kumar, S. (2020). Role of particle fineness on engineering properties and microstructure of fly ash derived geopolymer. Construction and Building Materials, 233, 117294.

[37] Nehdi, M., & Rahman, M. A. (2004). Estimating rheological properties of cement pastes using various rheological models for different test geometry, gap and surface friction. Cement and concrete research, 34(11), 1993-2007.

[38] Peng, Y., Ma, K., Long, G., & Xie, Y. (2019). Influence of Nano-SiO2, Nano-CaCO3 and Nano-Al2O3 on Rheological Properties of Cement–Fly Ash Paste. Materials, 12(16), 2598.

[39] Favier, A., Hot, J., Habert, G., de Lacaillerie, J. B. D. E., & Roussel, N. (2013, September). Rheology of geopolymer: comparative study between Portland cement and metakaolin based geopolymer. In 1st RILEM International Conference on Rheology and Processing of Construction Materials., RILEM Publications sarl, Paris: France (pp. 49-56).

[40] Yang, T., Zhu, H., Zhang, Z., Gao, X., Zhang, C., & Wu, Q. (2018). Effect of fly ash microsphere on the rheology and microstructure of alkali-activated fly ash/slag pastes. Cement and Concrete Research, 109, 198-207.

[41] Soares, A. A., de Oliveira Freitas, J. C., de Araujo Melo, D. M., Braga, R. M., Amaral-Machado, L., Santos, P. H. S., & Soares, L. W. O. (2017). Cement slurry contamination with oil-based drilling fluids. Journal of Petroleum Science and Engineering, 158, 433-440.

[42] Kamal, M. S., Adewunmi, A. A., Sultan, A. S., Al-Hamad, M. F., & Mehmood, U. (2017). Recent advances in nanoparticles enhanced oil recovery: rheology, interfacial tension, oil recovery, and wettability alteration. Journal of Nanomaterials, 2017.

[43] Cardoso, F. A., Fujii, A. L., Pileggi, R. G., & Chaouche, M. (2015). Parallel-plate rotational rheometry of cement paste: Influence of the squeeze velocity during gap positioning. Cement and Concrete Research, 75, 66-74.

[44] Grandes, F. A., Sakano, V. K., Rego, A. C., Cardoso, F. A., & Pileggi, R. G. (2018). Squeeze flow coupled with dynamic pressure mapping for the rheological evaluation of cement-based mortars. Cement and Concrete Composites, 92, 18-35.

[45] Leemann, A., & Winnefeld, F. (2007). The effect of viscosity modifying agents on mortar and concrete. Cement and Concrete Composites, 29(5), 341-349.

[46] Kaze, C. R., Alomayri, T., Hasan, A., Tome, S., Lecomte-Nana, G. L., Nemaleu, J. G. D., ... & Rahier, H. (2020). Reaction kinetics and rheological behaviour of meta-halloysite based geopolymer cured at room temperature: Effect of thermal activation on physicochemical and microstructural properties. Applied Clay Science, 196, 105773.

[47] Puligilla, S., & Mondal, P. (2013). Role of slag in microstructural development and hardening of fly ash-slag geopolymer. Cement and Concrete Research, 43, 70-80.

[48] Struble, L., Kim, T. Y., & Zhang, H. (2001). Setting of cement and concrete. Cement, concrete and aggregates, 23(2), 88-93.

[49] Justnes, H., Clemmens, F., Depuydt, P., Van Gemert, D., & Sellevold, E. J. (2000, October). Correlating the deviation point between external and total chemical shrinkage with setting time and other characteristics of hydrating cement paste. In Proceedings of the International RILEM Conference (Vol. 1, pp. 57-73).

[50] Alvi, M. A. A., Khalifeh, M., & Agonafir, M. B. (2020). Effect of nanoparticles

on properties of geopolymers designed for well cementing applications. Journal of Petroleum Science and Engineering, 191, 107128.

[51] McLellan, B. C., Williams, R. P., Lay, J., Van Riessen, A., & Corder, G. D. (2011). Costs and carbon emissions for geopolymer pastes in comparison to ordinary portland cement. Journal of cleaner production, 19(9-10), 1080-1090.

[52] Wang, C., Liu, S., Wu, J., & Li, Z. (2014). Effects of temperature-dependent viscosity on fluid flow and heat transfer in a helical rectangular duct with a finite pitch. Brazilian Journal of Chemical Engineering, 31(3), 787-797.

[53] Xu, Q., Hu, J., Ruiz, J. M., Wang, K., & Ge, Z. (2010). Isothermal calorimetry tests and modeling of cement hydration parameters. Thermochimica Acta, 499(1-2), 91-99.

[54] Cai, J., Li, X., Tan, J., & Vandevyvere, B. (2020). Thermal and compressive behaviors of fly ash and metakaolin-based geopolymer. Journal of Building Engineering, 30, 101307.

[55] Duxson, P., Provis, J. L., Lukey, G. C., & Van Deventer, J. S. (2007). The role of inorganic polymer technology in the development of 'green concrete'. cement and concrete research, 37(12), 1590-1597.

[56] Robayo, R. A., De Gutiérrez, R. M., & Gordillo, M. (2016). Natural pozzolan- and granulated blast furnace slag-based binary geopolymers. Materiales de Construcción, 66(321), 077.

[57] Biondi, L., Perry, M., Vlachakis, C., Wu, Z., Hamilton, A., & McAlorum, J. (2019). Ambient cured fly ash geopolymer coatings for concrete. Materials, 12(6), 923.

[58] Huang, X., Yu, L., Li, D. W., Shiau, Y. C., Li, S., & Liu, K. X. (2015). Preparation and properties of geopolymer from blast furnace slag. Materials Research Innovations, 19(sup10), S10-413.

[59] Pilehvar, S., Sanfelix, S. G., Szczotok, A. M., Rodríguez, J. F., Valentini, L., Lanzón, M., ... & Kjøniksen, A. L. (2020). Effect of temperature on geopolymer and Portland cement composites modified with Micro-encapsulated Phase Change materials. Construction and Building Materials, 252, 119055.

[60] Mo, B. H., Zhu, H., Cui, X. M., He, Y., & Gong, S. Y. (2014). Effect of curing temperature on geopolymerization of metakaolin-based geopolymers. Applied clay science, 99, 144-148.

[61] Domingos, L. F. T., Azevedo, A. G. S., Lombardi, C. T., & Strecker, K. (2020).

Corrosion resistance of fly ash-based geopolymer in hydrochloric and sulfuric acid solutions. Cerâmica, 66(380), 394-403.

[62] Musil, S. S., & Kriven, W. M. (2014). In situ mechanical properties of chamotte particulate reinforced, potassium geopolymer. Journal of the American Ceramic Society, 97(3), 907-915.

[63] Yeddula, B. S. R., & Karthiyaini, S. (2020). Experimental investigations and prediction of thermal behaviour of ferrosialate-based geopolymer mortars. Arabian Journal for Science and Engineering, 1-22.

[64] Duxson, P., Lukey, G. C., & van Deventer, J. S. (2007). Physical evolution of Na-geopolymer derived from metakaolin up to 1000 C. Journal of Materials Science, 42(9), 3044-3054.

[65] Pouhet, R., Cyr, M., & Bucher, R. (2019). Influence of the initial water content in flash calcined metakaolin-based geopolymer. Construction and Building Materials, 201, 421-429.

[66] Zhang, H. Y., Kodur, V., Qi, S. L., Cao, L., & Wu, B. (2014). Development of metakaolin–fly ash based geopolymers for fire resistance applications. Construction and Building Materials, 55, 38-45.

[67] Kubatová, D., Rybová, A., Zezulová, A., & Švec, J. (2018, June). Thermal behaviour of inorganic aluminosilicate polymer based on cement kiln dust. In IOP Conference Series: Materials Science and Engineering (Vol. 379, No. 1, p. 012008). IOP Publishing.

4 Mechanical behavior of K- and Na-based, strain-hardening geopolymer composites (SHGC) reinforced with PVA fibers

4.1. Introduction

Strain-hardening cement-based composites (SHCC) [1] also called engineered cementitious composites (ECC) [2], represent a class of materials which were introduced in the early 90s [2] and which yield pronounced multiple cracking and hence, high strain capacity under tensile loading. SHCC are developed based on theories of micromechanical and fractural mechanics [1-4]. Such composites are commonly obtained by incorporating moderate amounts (1-3%) of short, synthetic micro-fibers into purposefully designed, fine-grained cementitious matrices [2,4]. With their favorable mechanical properties, such as tensile ductility, excellent crack control, damage tolerance, and high energy dissipation capacity, SHCC are suitable as the chief material both for new construction and for retrofitting applications. In both cases the use of SHCC enhances the durability and mechanical response of structures exposed to severe loading and environmental conditions [5-12].

Although the benefits of SHCC are evident [1-11], it is important to address their sustainability when choosing this type of material for large-scale applications [12] since SHCC contain a relatively high amount of cement, due to strict limitations regarding aggregates' content [13]. These issues are associated with high CO_2 emissions [12,14] as well as water demand, which is typical for cement-based binders [15]. Thus, the material design concept [13] should be extended to use feasible, more sustainable alternatives to cement, but still delivering equivalent mechanical performance [12]. The so-called geopolymers [16] appear to be such an alternative [12].

Initial studies on geopolymers date back to the 1930s, where Kuhl [15] evaluated the reaction between slag, a form of industrial waste, and potassium hydroxide (KOH). In the 1940s, Purdon [17] presented considerations on mixing the aforementioned residue with sodium-based solutions (NaOH). In 1967, Glukhovsky [18] provided complete reports describing the production of aluminosilicate binders with low calcium content, designating them as "alkaline binding systems", described by the general formulation: Me2•MO•Al2O3•SiO2•H2O (where Me = Na, K; and M = Ca, Mg). The term “geopolymers” was first introduced in the early 70s by Davidovits [16], who created a binder based on aluminosilicate materials only in order to enhance the thermal resistance of structural elements [19]. His team developed a fabrication method based on geosynthesis to obtain high-performance ceramic materials by the reaction of pure aluminosilicates in a stable alkaline environment [16,20]. The polymer network consists of SiO4 and AlO4 tetrahedra linked alternately by sharing oxygen in a range from amorphous to semi-crystalline [21], requiring positive ions to balance the negativity of Al3+ in IV-fold coordination [16,21]. Its empirical formula can be described as M2O•Al2O3•xSiO2•11H2O (where M = Na, K, Cs; and x represents the Si/Al ratio used) [21]. Although generally specified as a subclass of alkali-activated materials due to their many similarities, geopolymers require distinct mixing and reaction processes [21-24].

The reaction and hardening mechanisms, as well as the production particularities of geopolymers, aside from the benefits of their sustainability, may present appealing advantages in their use as an alternative to the common cementitious matrices. Such benefits range among fast setting time [22,25]; enhanced thermal resistance [19,20,26], high chemical [26,27] and long-term [28] durability; low Young’s modulus (positive in repair applications) with low variation determined mainly by its characteristic microstructure and aluminosilicate [28,29]; and low porosity [30]. The primary source of alumina and silica influences the mechanical properties of the final material since its chemical composition impacts the amount of alkali solution required to stabilize the reaction [26,29]. Hence, geopolymers based on fly ashes and metakaolin present very distinct microstructures and, consequently, different properties and behaviors [22,26,29]. Thus, the use of raw materials must be considered depending on their availability in the region of interest and particular applications [30].

In addition to extensive studies on plain geopolymer matrices, various composites have been investigated containing:

- aggregates [27,28];
- synthetic (carbon) [31], mineral (basalt) [32] and natural fabrics (jute, curauá, sisal) [25];
- and short polymer micro-fibers [33,34].

The latter approach was explored by Ohno *et al.* [33,35] and Nematollahi *et al.* [34,36] in studies on the production of fly ash-based engineered geopolymer composites (EGC) and strain-hardening geopolymer composites (SHGC), respectively. Note that both names stand for the same material group. Through a comprehensive analysis of the matrix design [37], optimal volume fractions of PE and PVA reinforcements [36] and by considering micromechanics-based material design [3,4], fly-ash-based SHGCs were obtained with strain capacities up to 4.5% [33]. Batista *et al.* [38] evaluated the gradual replacement of metakaolin by silica fume and its influence on the mechanical behavior of strain-hardening, alkali-activated materials and analyzed its cost-effectiveness. However, despite reaching reasonable tensile strength values with this substitution (on the order of 4.5 MPa), the strain capacity of the composite was in the range of 1%, thus demonstrating need for improvement.

This study aims at a comprehensive evaluation of established metakaolin-based geopolymer mixtures with respect to their use as SHGC matrix. Additionally, the effect of distinct alkali solutions (Na- and K-based) and the efficiency of the incorporation of fine-grained aggregates into the SHGC mixtures reinforced with PVA fibers are analyzed. The resulting mechanical performance characteristics are discussed not only against the background of the theories of fracture mechanics but also with respect to the microstructure of the GP matrices and SHGC and well as their behavior in fresh state.

4.2. Experimental program

4.2.1. Materials

Two geopolymer mixtures were produced through the combination of an aluminosilicate source (metakaolin, MK) and an alkali-based solution (Na- or K-based water glass, WG), representing a final composition of $X_2O \cdot Al_2O_3 \cdot 4SiO_2 \cdot 11H_2O$; where X may be replaced by Na or K elements. Sodium (Na) and potassium (K) hydroxide in pellets (Sigma-Aldrich®, reagent grade > 90%) were dissolved in deionized water, where hydrophilic fumed silica (CAB-O-SIL® M-5) was added and mixed for 24 h using a magnetic stirrer, forming the stable water-glass solution. Metamax from BASF was used as the aluminosilicate source due to its high level of purity and small particle size, enabling adequate reactivity, as presented and discussed in previous studies [22,39]. An LS 13-320 Beckman Coulter apparatus was used to verify the particle size distribution of metakaolin. A small amount corresponding to 0.5 g of the material was mixed previously with isopropanol in a magnetic stirrer and then placed inside the device. Figure 4.1 shows that this material has a range of particle size between 0.5 µm and 15 µm.

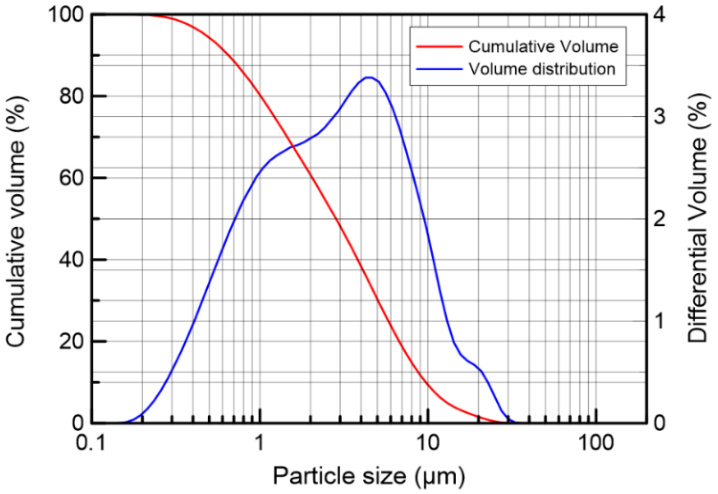

Figure 4.1 – Particle size distribution of metakaolin.

The material contents (in grams) in each mixture are presented as WG:MK as follows: (i) 1000:585 and (ii) 1000:538,39 for NaGP and KGP, respectively. Distinct types of reinforcements were incorporated in both matrices in order to evaluate their effectiveness in various combinations. The letter “A” is used for fine quartz sand with a maximum diameter of 0.2 mm and density equal to 2.62 g/cm³ added to a 50% by mass content of MK. The WG-to-MK ratios obtained from the chemical formulations showed previously are 1.71 and 1.85 for NaGP and KGP, respectively.

PVA short fibers produced by Kuraray under the brand name Kuralon® K-II REC 15 were used in a mixture with 2% content by volume for both mixtures. Their length is 12 mm, the diameter 40 µm, and the density 1.26 g/cm³, while tensile strength and Young’s modulus according to the information by the producer are 1600 MPa and 40 GPa, respectively. Since PVA fibers are highly hydrophilic, during production they are coated with an oil agent (1.2 wt.%) to limit the chemical bond strength in cementitious matrices.

4.2.2. Production

A planetary Hobart mixer with a capacity of 10 l was used to produce the matrices and composites as follows: (i) addition of metakaolin and water glass in the mixer; (ii) mixing for 3 min at intermediate speed (198 rpm) to ensure proper homogeneity and reactivity; (iii) addition of aggregates; (iii) mixing for 1 min at intermediate speed (198 rpm); (iv) addition of fibers; (v) mixing for 3 min at higher speed (365 rpm) allowing proper fiber distribution in the geopolymer binder. The fresh mix was then poured into molds, which required a vibration step of 1 min both for consolidation and removal of voids. The molds were sealed in plastic bags for 48 h at room temperature to prevent early dehydration. After this period, the samples were removed from the molds and kept inside dry plastic bags for 2 weeks, which is the necessary curing regime to stabilize the geopolymer water loss. It is important to note that the molds for flexural and tensile specimens used in this study were made of steel, which in the case of geopolymers usually results in difficulties on mold release. For this reason, semitransparent adhesive tapes were used to cover and protect the steel parts of the molds, allowing complete removal of the materials after 48 hours of curing.

Prismatic specimens with dimensions of 160 mm x 40 mm x 40 mm were produced for the bending tests. Some of these specimens were produced with a notch by positioning an aluminum plate in the center of the mold, creating an opening 1.5 mm thick and 12 mm high. Dumbbell-shaped specimens were produced for uniaxial tension tests. They had a rectangular middle cross-section of 40 mm x 24 mm in accordance with the dimensions established in previous studies; see e.g. [9].

The manufacturing process of single-fiber pullout specimens followed a distinct methodology, where a special rectangular polymer-made mold was used; see Figure 4.2a. Three long polymeric plates (two sturdy and one thinner and lower) were screwed together, creating a longitudinal channel in the middle of the mold (Figure 4.2a). The width of the channel corresponds to the desired fiber embedment length of 2 mm. The fibers were then transversely positioned over the channel with a spacing of 10 mm between each other and carefully fixed with wax at their ends. Two long plates were then positioned and screwed onto the first two sturdy plates, ensuring a 6 mm total channel depth, which was subsequently filled completely with matrix material; see Figure 4.2b. The molding process and curing regime followed the same procedure as presented above for other specimens.

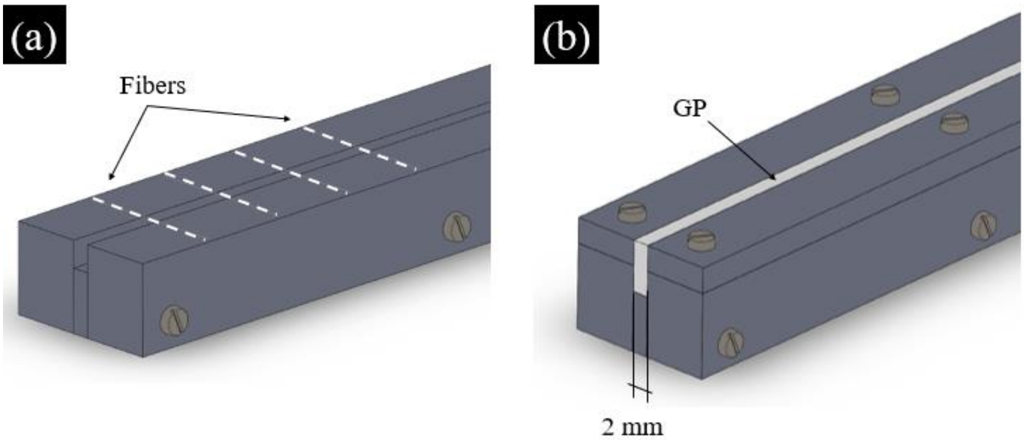

Figure 4.2 – Schematic view of the mold for single-fiber pullout specimens and of the casting process: (a) fibers' positioning; (b) final assembly after casting.

Demolding consisted of extracting the "long" beams from the pullout mold with laterally protruding fibers. For single specimen preparation, the beams were cut between the fibers, resulting in at least 10 single specimens with approximate dimensions of 6 mm x 6 mm and 2 mm thickness, corresponding to the embedded length. The subsequent preparation of the samples consisted in cutting the fibers on one side of the specimen and isolating the remaining spot with wax to avoid any contact of the fiber with glue in the later steps prior to testing.

4.3. Testing methods

4.3.1. Fresh-state properties of the geopolymer mixtures

The fresh-state properties of the geopolymer mixtures with and without aggregates were evaluated by means of flow table tests according to ASTM C1437 [40] and ASTM C230 [41]. The cone dimensions were 80 mm top diameter, 125 mm bottom diameter and 65 mm height. The flow diameter was measured after cone removal, followed by 25 vertical jolts applied to the table for 15 seconds. The standard consistency was equal to the average of the diameter measured after the test in two orthogonal directions. Four tests were performed for each mixture. The viscosity of the mixtures was assessed following ASTM D6910 [42]: the fresh mix was completely poured into a funnel and the time for all its content to pass through its 4.75 mm square opening was recorded. Additionally, the fresh density was obtained according to ASTM C138 [43], for which the fresh mixtures were placed with subsequent consolidation inside cylindrical containers with known dimensions.

4.3.2. Analytical investigations

An XRD 3003 TT diffractometer system (model 7000XRD) was used to investigate the raw material (metakaolin) and the synthesized geopolymers in amounts of 0.22 g. The results of the X-ray diffractions were obtained by using copper irradiation (Cu-Ka, $\lambda = 1.5418$ Å) operating at 40 kV and 30 mA. Scans were performed using an angular velocity of 0.02º per 6 seconds, measuring the intervals between (2θ) Bragg angles of 5° and 70°. The geopolymer samples were ground in a McCrone Micronizing mill with isopropanol and mixed with 10 wt.% of ZnO as the internal standard for quantification. Metakaolin was also tested with the same amount of ZnO but X-rayed without isopropanol treatment.

Untested specimens were cut into 10 mm x 10 mm x 10 mm cubes for porosity evaluations. Two types of treatments (i) isopropanol immersion and (ii) freezing were tested; and the first was established as the most adequate, non-destructive system to determine the porosity of the geopolymer samples. The samples were placed into an Alpha 1-2 LDplus Christ vacuum desiccator for drying over 24 h, allowing its evaluation in a Porotec Porosimeter PASCAL 140/440, with a mercury surface tension of 0.48 N/m, a contact angle of 140º and maximum testing pressure of 400 MPa. The tests were performed in a temperature range of 23 to 23.6 ºC with increased and decreased speeds of 6 to 19 MPa/min and 28 to 7 MPa/min, respectively.

The pore quantity and characteristics in the reinforced matrices were analyzed additionally in order to evaluate the impact of fibers and aggregates on the composites' microstructure. An ESEM Quanta 250 FEG (FEI, Eindhoven/ The Netherlands) was used for microscopic analysis of the fracture surfaces of the geopolymer matrices and fiber-reinforced composites. Additionally, energy dispersive X-ray (EDX) spectroscopy was used with a 15 kV accelerating voltage in order to obtain an accurate information on phases and their distribution in the samples.

4.3.3. Mechanical testing setups

A servo-hydraulic MTS universal testing system with a load capacity of 200 kN was used to perform three-point bending tests with all material variations presented previously. The tests were carried out based on the BS EN 196-1 [44]; 3 specimens were tested for each material variation under a load-controlled rate of 50 N/s. The span between the specimen supports was 100 mm.

Three-point bending tests were performed on notched specimens in a servo-hydraulic MTS testing system with closed-loop control and a load cell of 100 kN for all plain matrix samples presented previously. All specimens were tested at a constant crack mouth opening displacement (CMOD) rate of 0.008 mm/min, in order to maintain crack growth stability. The span distance between end supports was equal to 120 mm. The compressive stress-deformation responses were obtained using 40 mm cubes in the same testing system using a loading rate of 2400 N/s.

Hydraulic Instron testing equipment (model 8501) with closed-loop control and a load capacity of 100 kN was used to perform the uniaxial tension tests on the composites under a displacement rate of 0.04 mm/s. Three dumbbell-shaped specimens were tested for each composite material. The specimens were glued at their ends in 20 mm thick, steel rings bolted to the testing machine, in this way ensuring non-rotatable boundary conditions. The specimen was first glued in one ring outside of the machine, while after glue hardening the other end was subsequently glued inside the machine. Two Linear Variable Differential Transducers (LVDTs) were attached to each side of the specimen using a steel frame in order to measure the deformation of the 100 mm gauge length. Figure 4.3 presents the tensile testing setup.

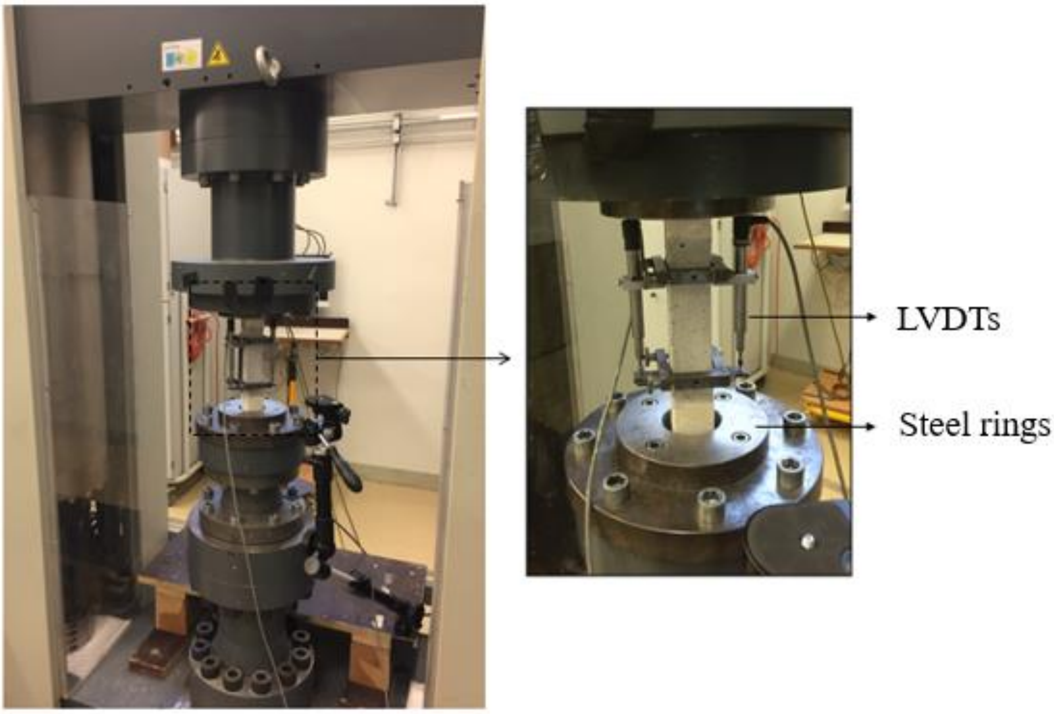

Figure 4.3 – Setup for the uniaxial tension test.

Additionally, optical measurements were performed during the tension tests in order to monitor and quantify the specimen deformation, crack formation and fracture processes with the help of Digital Image Correlation (DIC). A black and white speckle pattern was sprayed onto the specimens for this purpose. The optical sampling rate was 1 frame in 5 seconds. The frames were processed with a commercial software ARAMIS 5M, developed by GOM GmbH.

Single-fiber pullout tests were performed for all fiber-mixture combinations in a Zwick-Roell testing machine (model Z 1445) with a 0.05 mm/s displacement rate using a load cell of 10 N capacity. It was only possible to use the displacement recorded from the transverse actuator, the fiber elongation and displacement were not measured directly. Figure 4.4 presents the testing setup for single-fiber pullout experiments. The specimens were glued on a flat aluminum plate, which was screwed to the lower part of the machine. The free fiber end was glued to another plate, which was attached to the force sensor.

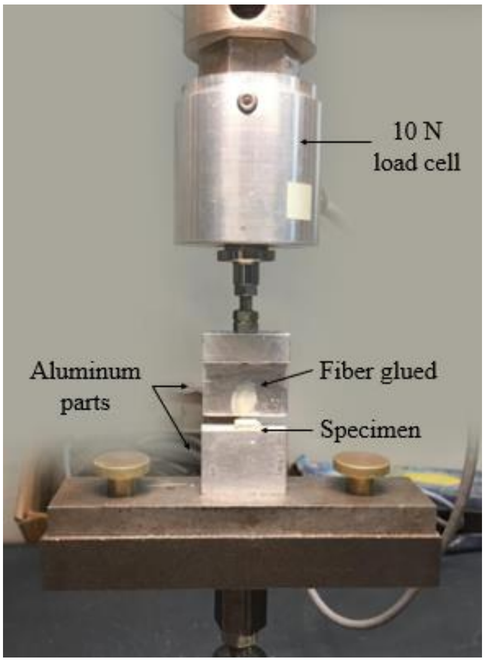

Figure 4.4 – Setup for the single-fiber pullout test.

4.3.4. Fracture mechanics requirements

Previous studies of SHCC demonstrated the importance of the crack-bridging response by fibers extending across a crack in the matrix, usually referred to the bridging stress (σ) versus crack opening (δ) curve [35,47,48,49]. The bridging performance necessary to reach pseudo-strain-hardening (PSH) behavior can be estimated by means of the pullout and bending tests on notched specimens [1,36]. This methodology has already been adapted previously for geopolymer materials and is considered once again in this study since it allows the derivation of distinct material parameters. Fracture toughness is a measure of the magnitude of the stress concentration occurring in the crack tip when the crack starts to propagate [35,49]. According to the crack model presented in previous studies [50], the material's modulus of elasticity E_m and fracture toughness K_m can be obtained by the following equations:

$$E_m = \frac{0.413\,P_i}{\delta_i}\left[\frac{l^3\left(1+\frac{5\omega l}{8P_i}\right)}{4bd^3\left(1-\frac{a}{d}\right)^3}+\frac{1.17l}{1.68bd\left(1-\frac{a}{d}\right)}\right] \quad (1)$$

$$K_m = \sigma_n\sqrt{\alpha_e}\,Y(\alpha) \quad (2)$$

$$Y(\alpha) = \frac{1.99-\alpha(1-\alpha)(2.15-3.93\alpha+2.70\alpha^2)}{(1+2\alpha)(1-\alpha)^{1.5}} \quad (3)$$

where [46]:

P_i corresponds to a load level in the initial portion of the load-deflection plot, δ_i is the deflection value; l, b, and d are the span, width, and depth of the specimen, respectively; a and ω are the initial notch depth and self-weight of the specimen per unit length, respectively.

σ_n is the flexural strength of the specimen; α_e is the effective notch depth that can be obtained from equation 2 and $Y(\alpha)$ is the correction factor; $\alpha = \alpha_e/d$.

Following recommendations in the literature, two criteria must be satisfied to obtain pseudo-strain hardening behavior with multiple cracking formations: (i) an energy-based condition; and (ii) a stress-based condition [1,34,38,48]. The energy-based condition can be expressed as [1,34,48]:

$$J_{tip} \leq J'_b \quad (4)$$

where J'_b is the complementary energy, and J_{tip} is the composite crack tip toughness, obtained from the σ(δ) curve [1,34,38]. J_{tip} and J'_b can be expressed as:

$$J_{tip} = \frac{(K_m)^2}{E_m} \quad (5)$$

$$J'_b = V_f \frac{L_f}{d_f}\left(\frac{\tau_0^2 L^2_f}{6 d_f E_f} - 2G_d\right) \quad (6)$$

Equation (6) is related to energy equilibrium during steady state [1,34,38]. If J'_b is greater than J_{tip}, steady state as well as the occurrence of a multiple cracking behavior is assured [1,4,48]. The shape of the σ(δ) curve and the rising branch associated with J'_b are also related to the fiber/matrix interactions [4,47]. When fibers are only in frictional contact with the matrix, the stiffness is mainly controlled by the fiber content V_f, diameter d_f, length L_f, stiffness E_f and frictional bond τ_0 [4,47]. When a chemical bond G_d occurs, the starting point of the curve is not at the origin but is shifted upwards [4,47], resulting in the need for interfacial mechanisms to occur before the chemical adhesion is lost to guarantee an improved loading distribution. The chemical adhesion energy G_d is equivalent to [34]:

$$G_d = \frac{2\left(P_{ad} - P_{fr}\right)^2}{\pi^2 E_f d_f^3} \quad (7)$$

where E_f is Young's modulus of the fiber, and d_f is the fiber diameter.

Thus, the presence of G_d diminishes the complementary energy J'_b. The stress-based condition corresponds to [1,34,48]:

$$\sigma_{fc} \leq \sigma_0 \text{ (8)}$$

where σ_0 is the ultimate tensile strength of the composite, and σ_{fc} is the stress at the formation of the first crack in the composite. If σ_0 is greater than σ_{fc}, there will be multiple crack formation; if σ_{fc} is greater than σ_0, the composite will fail after the formation of its first crack [1,34]. In the literature [1] it is also suggested to use PSH performance indices to evaluate the behavior of the composites [1,38]:

$$\text{Energy-based condition: } PSH_{(1)} = \frac{J_b'}{J_{tip}} \text{ (9)}$$

$$\text{Stress based condition: } PSH_{(2)} = \frac{\sigma_0}{\sigma_{fc}} \text{ (10)}$$

Indices higher than 1 indicate the likelihood of strain-hardening.

4.4. Results and discussion

4.4.1. Fresh-state properties of the geopolymer mixtures

The results obtained from fresh mixtures are summarized in Table 4.1. The average values for flowability obtained for NaGP and KGP were 241 mm and 284 mm, respectively. The incorporation of aggregates led to a reduction of the flow diameter to 193 mm and 226 mm, respectively. The aggregates had the similar effect on the viscosity of the fresh mixtures. The NaGP and KGP matrices required 102 and 78 seconds to pass through the funnel opening completely, while on addition of aggregates the duration increased to 145 and 108 seconds, respectively. The influence of aggregates on the flowability can be attributed to the increase in internal friction [52] associated with the difference between MK and sand grain sizes. This increase in internal friction can also improve the homogeneity of the matrix as well as the fiber dispersion in the matrix during mixing, which is explained in the next sections. As expected, the fine aggregates also influenced the fresh density results, where sand-reinforced mixtures presented 6.9 to 9.1% greater values when compared to the plain matrices.

Table 4.1 – Fresh properties of Na- and K-based GP mixtures.

Mixture	Aggregates	Flowability (mm) ASTM C1437 [40]	Viscosity (s) ASTM D6910 [42]	Fresh density (g/cm^3) ASTM C138 [43]
NaGP	-	241	102	1.69
NaGP+A	Fine sand	193	145	1.81
KGP	-	284	78	1.61
KGP+A	Fine sand	226	108	1.76

4.4.2. Analytical investigations

The XRD patterns of the raw material MK and of the two GP formulations are presented in Figure 4.5.

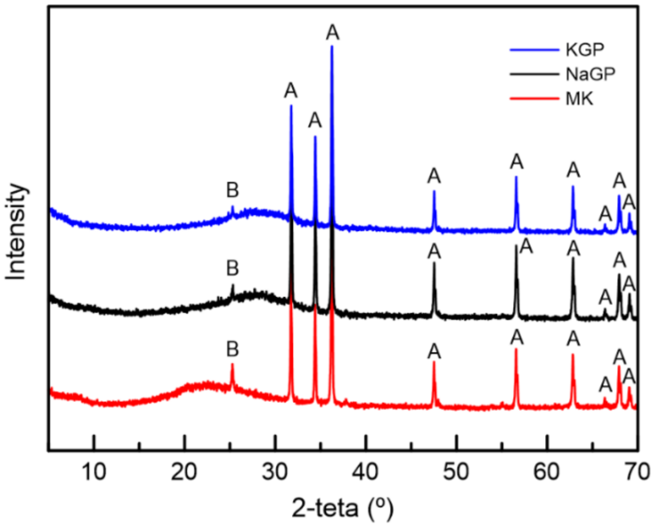

Figure 4.5 – Diffractograms of metakaolin (MK), KGP and NaGP: (A) ZnO and (B) TiO_2.

From the diffractograms it is possible to deduce that they are mostly amorphous, with crystalline peaks from ZnO and TiO2 (25.3º 2θ), resulting from the sample treatment and impurities from its fabrication, respectively. Usually, an amorphous material subjected to XRD evaluations may present 1 or 2 humps related to an irregular arrangement of atoms in its microstructure [22]. This pattern is no different for the samples studied in this paper, with the presence of broad humps in all of the samples' distinctions related to their position in the aluminosilicate material (18º-30º 2θ) and geopolymers (24-32º 2θ), which originate from the geopolymerization process and depends on the Si-to-Al ratio, as evidenced in previous studies [51,53]. The results obtained from MIP measurements are presented in Figure 4.6 and Table 4.2.

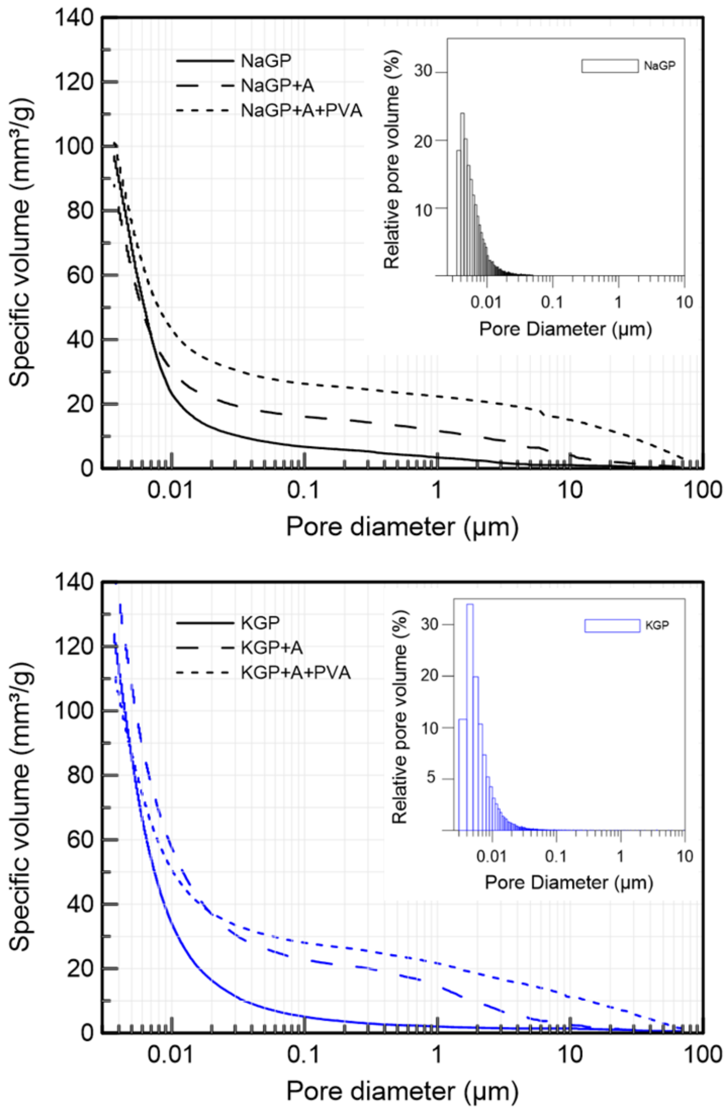

Figure 4.6 – Results of MIP analysis for: (i) Na and K-based plain matrix; (ii) enriched with aggregates; and (iii) containing both aggregates and PVA fibers.

It is possible to notice differences between NaGP and KGP plain matrices treated in isopropanol solutions (blue and black curves). NaGP exhibits lower total porosity at 16.04%, while KGP reaches a slightly larger value of 18.49%. This difference may be associated with: (i) the total volume of water entrapped in the mixture when still in the fresh state and its consequent evaporation during the curing regime; and (ii) different reaction kinetics of NaGP and KGP resulting in their distinguishable microstructures. KGP production requires a larger amount of water in the KOH solution to be in accord with the requirements prescribed in its general formulation. This may lead to a more porous material and higher susceptibility to shrinkage effects. However, it is interesting to note that the average pore diameter found for both plain matrices was practically the same, showing regular nano-porosity for GPs in general, as indicated in previous studies [22,51].

Table 4.2 – General results of MIP analysis.

Sample	Porosity by Hg intrusion (%)	Average pore diameter (µm)	Bulk density (g/cm³)
NaGP	16.04	0.0067	1.65
NaGP+A	16.46	0.0074	1.71
NaGP+A+PVA	16.86	0.0084	1.77
KGP	18.49	0.0067	1.49
KGP+A	20.32	0.0079	1.54
KGP+A+PVA	21.02	0.0087	1.59

With the addition of aggregates and fibers, increases in total porosity and pore size were recorded. The larger change of porosity – an increase of 2.53% – occurred for KGP enriched with aggregates and fibers. Regarding bulk density, NaGP had higher values, equal to 1.65 g/cm³, while KGP reached only 1.49 g/cm³. When enriched with fibers and aggregates, NaGP-based materials yielded densities equal to 1.71 and 1.77 g/cm³, respectively, while KGP composites showed 1.54 and 1.59 g/cm³ for the same variations. Additionally, the bulk density values measured on the hardened materials were smaller than the ones found for the fresh state, which can be traced back to the water loss during storage and treatments adopted for this analysis; see Table 4.1.

Figure 4.7 shows the scanning electron microscopy results for both NaGP and KGP. A denser microstructure was observed for NaGP materials, while KGP samples presented a greater number of larger pores, confirming the previous findings by MIP analysis.

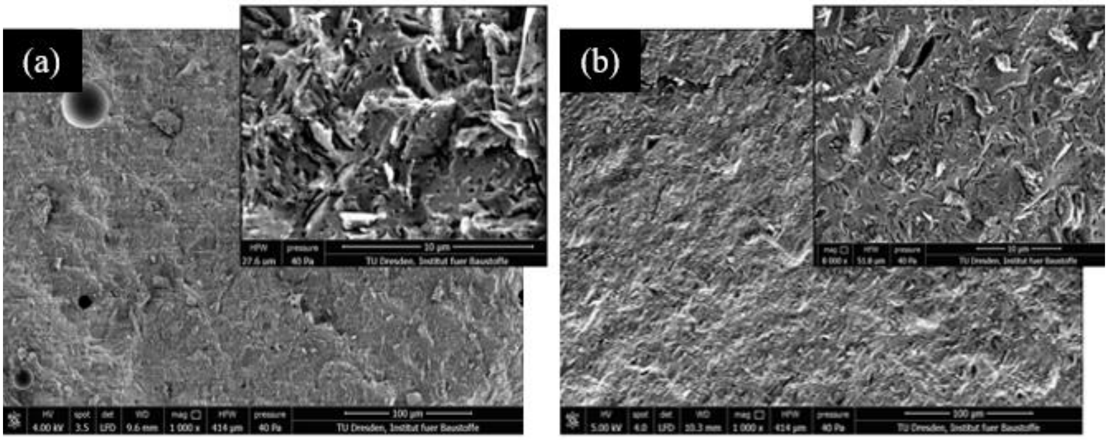

Figure 4.7 – Microstructure of the GP matrices in distinct magnifications: (a) NaGP and (b) KGP.

4.4.3. Mechanical properties of the geopolymers

Figure 4.8 and Table 4.3 present the results of the three-point bending tests, which demonstrated the flexural strength and fracture toughness of the geopolymers. In general, mixtures both with and without aggregates exhibited very brittle behavior, which can be laid to their fine-grained nature and the elastic behavior of ceramic materials at room temperatures [54]. Nevertheless, the plain GP matrices and those enriched with aggregates showed very distinct responses. The plain GP yielded a lower load-bearing capacity and considerably lower fracture toughness, the former being also dependent on the latter. The Na-based GPs had higher flexural strength when compared to the KGP.

Table 4.3 – Results of crack-mouth opening displacement (CMOD) measurements.

Mixture	$P_{máx}$ (N)	E_m (GPa)	K_m (MPa•m^0.5)	J_{tip} (N/m)
NaGP	368.77	8.76	0.152	2.63
NaGP+A	506.78	10.35	0.148	2.12
KGP	235.18	7.02	0.254	9.21
KGP+A	490.45	9.76	0.247	8.32

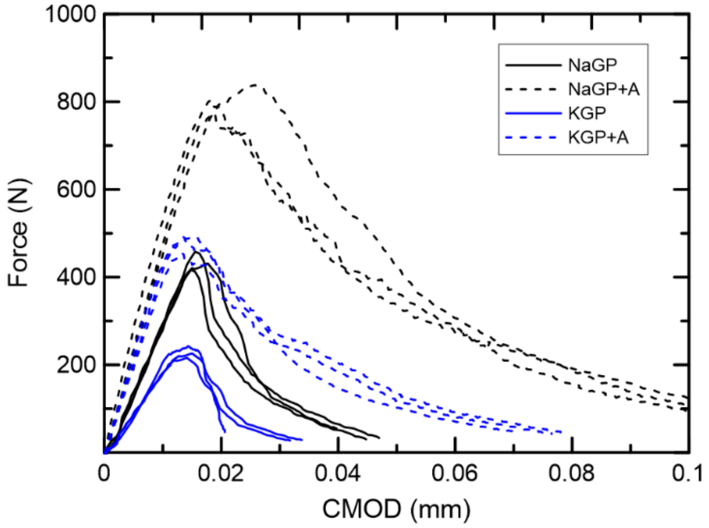

Figure 4.8 – Effects of matrix composition and addition of aggregates on force vs. CMOD curves.

These results are supported by the XRD, MIP and ESEM investigations, where NaGP mixtures exhibited higher density and lower porosity when compared to KGP. A material with low Young's modulus, such as KGP, tend to have an increased crack tip toughness (J_{tip}). This was verified by calculating the K_m and J_{tip} factors, which will be discussed later. Indeed, KGP-based compositions yielded higher J_{tip} values, 6.32 N/m on average in comparison to just 2.63 N/m measured for NaGP. This result may be explained by the intrinsic toughness of the GP materials, where a more porous microstructure leads to crack meandering effects [55]. As expected, Young's modulus was higher for materials enriched with aggregates, being more evident in the case of NaGPs. However, the J_{tip} values found for GP containing sand were not as distinct from the plain matrix, showing even slightly lower values, which indicates a low variability in the crack tip toughness of geopolymers with this type of inclusions.

By comparing the results obtained by various investigation techniques, it can be asserted that Na-based GP possess a less porous microstructure (MIP) and consequently higher density, per MIP and ESEM, resulting in higher values of flexural strength and modulus of elasticity but in a lower fracture toughness when compared to K-based GPs. These properties also influence the fracture behavior of the matrices, which is evaluated in the following analysis of the composites' behavior. In addition, the incorporation of aggregates decreases the fluidity of both systems and increases their density, the latter resulting in enhanced flexural strength and Young's modulus, but only little interference with their toughness, as observed in flexural tests on notched specimens.

4.4.4. Mechanical properties of the fiber-reinforced geopolymers

The representative flexural stress-deflection curves obtained for GP composites reinforced with PVA fibers are shown in Figure 4.9, while the corresponding average mechanical parameters are summarized in Table 4.4.

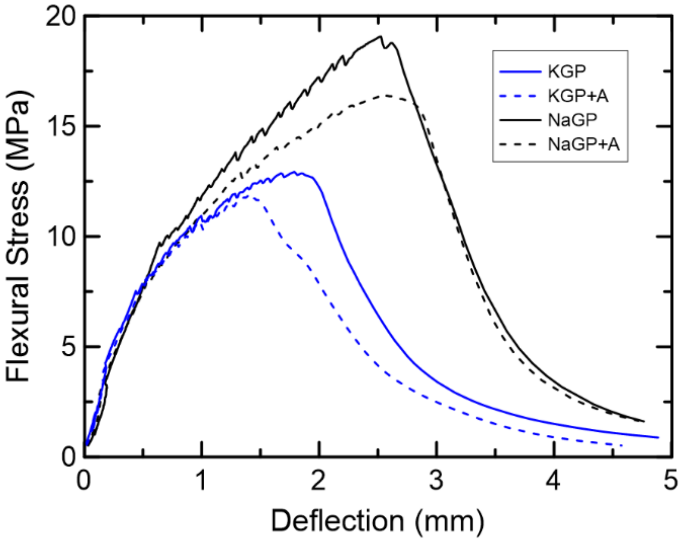

Figure 4.9 – Results of the bending tests on Na- and K-based geopolymers reinforced with PVA with and without aggregates.

The flexural stress was calculated by using the general formulation for three-point bending tests:

$$\sigma = \frac{3Pl}{2bd^2} \quad (11)$$

where P is the applied load; l is the span between supports; b and d are the width and depth of the specimen.

The results of the bending tests indicate the superior mechanical performance of NaGP-based fiber-reinforced composites when compared to the K-based GP; they reach an average flexural strength of 19.7 MPa, opposed to 14.9 MPa found for the latter. Since the flexural strength of strain-hardening composites is determined by the crack bridging action of the fibers to a great extent, the results also indicate distinct fiber-matrix interactions. The incorporation of aggregates had a negative effect on the flexural strengths of the composites, which can be attributed to the negatively altered fiber distribution. To identify and quantify better the effects of matrix composition and aggregates on the fiber-matrix interaction, single-fiber pullout tests appear to be instrumental.

Table 4.4 – Results of bending tests on Na- and K-based geopolymers: (i) plain matrix; (ii) enriched with aggregates; (iii) reinforced with PVA fibers; and (iv) containing aggregates and PVA fibers.

Mixture	σ max (MPa)	δ (mm)	Fracture energy (N•mm)
NaGP	1.82 (0.17)	-	-
NaGP+A	3.41 (0.21)	-	-
NaGP+PVA	19.74 (0.18)	2.74 (0.19)	24133 (2420)
NaGP+A+PVA	17.32 (0.94)	2.31 (0.38)	20153 (1792)
KGP	0.91 (0.12)	-	-
KGP+A	1.93 (0.35)	-	-
KGP+PVA	14.92 (1.82)	2.30 (0.29)	13800 (2570)
KGP+A+PVA	13.15 (1.08)	1.95 (0.14)	11805 (2784)

The stress-displacement curves obtained from compression tests are presented in Figure 4.10, their evaluation summarized in Table 4.5. An increase in compressive strength due to the use of aggregates is observed together with an enhancement of the stiffness of both types of geopolymers. The incorporation of fibers had a positive effect on compressive strength, mainly for Na-based GP materials: 77.6 MPa were reached for NaGP containing fibers and aggregates, as opposed to 44.1 MPa measured for plain NaGP. This behavior may be associated with the reduction of spalling effects that occur during the loading in the brittle unconfined geopolymers [54] by efficient crack bridging and force redistribution. Aggregates and especially fibers act as internal micro-confinements, enhancing the toughness and damage tolerance of the material. This improvement in strength was less pronounced in the case of K-based GP materials, arising from 37.4 MPa for plain KGP to 59.4 MPa for KGP containing both aggregates and fiber. Obviously, the fibers also improved the post-peak behavior of the specimens, leading to a shallower softening branch.

Table 4.5 – Results of compression tests on Na- and K-based geopolymers: (i) plain matrix; (ii) enriched with aggregates; (iii) reinforced with PVA fibers; and (iv) containing aggregates and PVA fibers.

Mixture	σ0 max (MPa)	Displacement at σ0 max (mm)
NaGP	44.09 (4.92)	0.775 (0.022)
NaGP+A	56.83 (8.27)	0.647 (0.032)
NaGP+PVA	65.48 (5.41)	1.185 (0.027)
NaGP+A+PVA	77.56 (11.48)	1.054 (0.039)
KGP	37.35 (3.81)	0.682 (0.024)
KGP+A	53.94 (4.67)	0.661 (0.025)
KGP+PVA	47.09 (4.71)	0.889 (0.044)
KGP+A+PVA	59.43 (3.77)	0.991 (0.073)

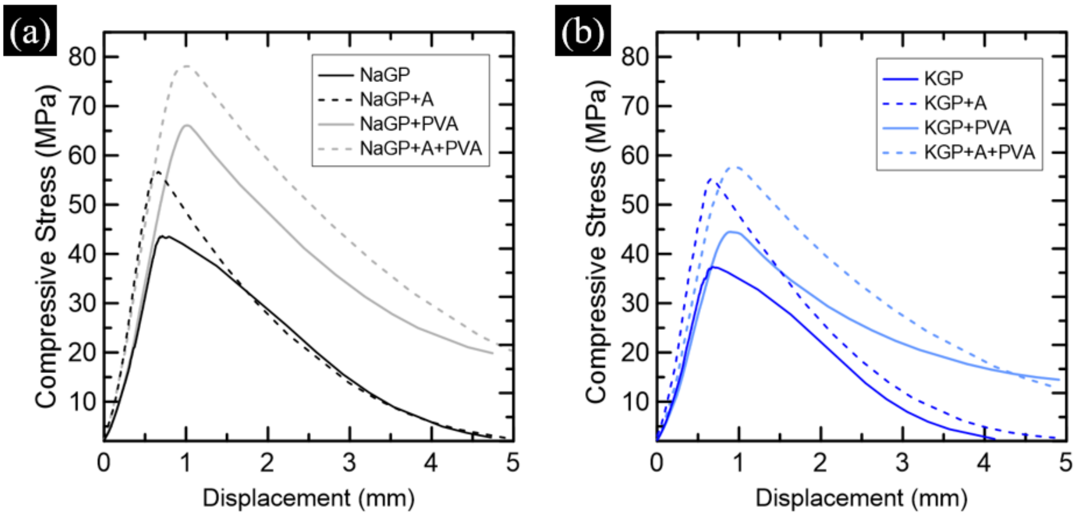

Figure 4.10 – Results of the compression tests on (a) Na- and (b) K-based geopolymers: (i) plain matrices; (ii) matrices enriched with aggregates; (iii) reinforced with PVA fibers; and (iv) containing aggregates and PVA fibers.

The tensile behavior of NaGP and KGP composites reinforced with PVA fibers are presented in Figure 4.11; Table 4.6 provides the characteristic values obtained by the evaluation of the strass-strain curves. For the NaGP-based compositions, a pronounced increase in first-crack stress can be observed for the material containing aggregates in comparison the plain matrix, from 2.0 MPa to 2.9 MPa. This result could be expected in considering the previous findings of this study. However, the composite without aggregates exhibited higher tensile strength, reaching 4.2 MPa, as opposed to the 3.8 MPa measured for the same material but containing sand. Nevertheless, both Na-based composites showed pronounced strain-hardening and great strain capacities of 3.5 to 4.8%. Obviously, an optimal balance between the cracking strength of the matrix and the crack-bridging capacity of the fibers was attained. The differences in fiber-matrix interactions for various types of matrices will be discussed when presenting the results of pullout tests.

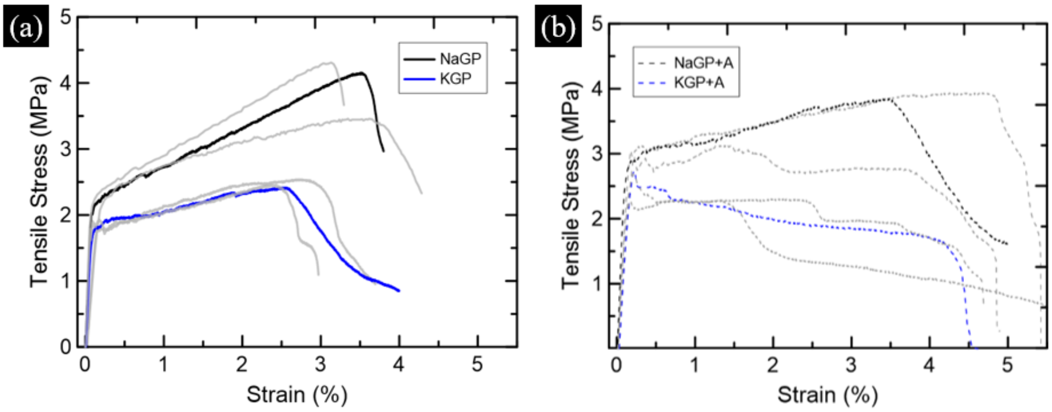

Figure 4.11 – Results of tension tests on Na and K-based geopolymers: (a) plain matrix with PVA fibers; and (b) with addition of both aggregates and PVA fibers.

The tensile behavior of the KGP composites was slightly different; the composite containing sand did not yield a typical strain-hardening curve, but a strain-softening one. In contrast, KGP composites without aggregates showed a stress gain with increasing strain, presenting themselves as a feasible option for SHGC. Young’s modulus calculated for K- and Na-based composites was in the same range of values, reaching 9.3 MPa to 9.8 GPa, respectively, for mixtures without aggregates, while a slight enhancement was observed for the corresponding mixtures with sand: 10.2 and 10.9 GPa, respectively, as evidenced in previous studies with sand incorporation [28,29].

Table 4.6 – Results of tension tests on Na- and K-based geopolymers: (i) plain matrix reinforced with PVA fibers; and (ii) containing both aggregates and PVA fibers.

Composite	σ_0 (MPa)	ε_1 (%)	E_t (GPa)	σ_{max} (MPa)	$\varepsilon_{capacity}$ (%)
NaGP	2.01 (0.07)	0.17 (0.02)	9.82 (0.99)	4.17 (0.47)	3.53 (0.79)
NaGP+A	2.87 (0.18)	0.16 (0.02)	10.94 (1.13)	3.71 (0.38)	4.76 (0.34)
KGP	1.86 (0.12)	0.20 (0.01)	9.30 (0.14)	2.57 (0.29)	2.68 (0.28)
KGP+A	2.73 (0.06)	0.18 (0.01)	10.17 (0.51)	2.73 (0.06)	-

Multiple cracking and fracture occurrence were evaluated with digital image correlation, allowing the determination of number of cracks, average crack width, and crack spacing as presented in Table 4.7 and Figure 4.12. Figure 4.12 also presents a typical analysis of the crack patterns at different stages of loading. Stage I represents the initial, crack-free elastic phase of the test. Stage II stands for the strain-hardening and multiple cracking phase. Stage III corresponds to the final strain-softening stage. A higher crack density was observed for NaGP composites, with and without aggregates, when compared to the KGP materials. However, crack widths recorded for KGP composites are in the same range as for NaGP mixtures, demonstrating a restriction in crack opening regardless the mixture used. In combination with a less pronounced multiple cracking, K-based SHGC yielded lower strain capacity in comparison to Na-based composites. It is interesting when one notices the slightly better crack control in comparison to common PVA-SHCC, which typically yield crack widths of about 70 µm and crack spacing of 2.5 mm [56].

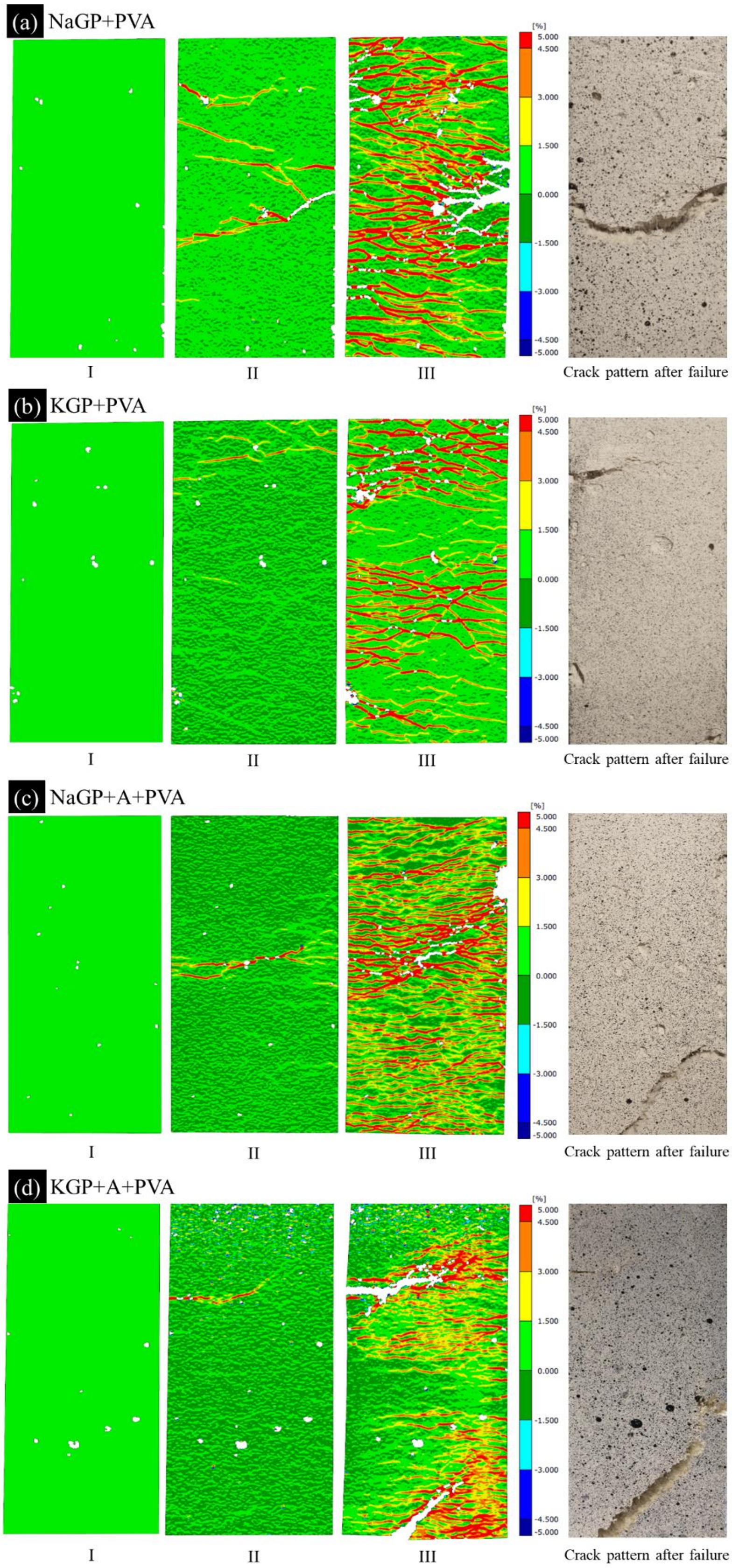

Figure 4.12 – Evaluation of cracking by means of DIC analysis for all composites in 3 different stages of loading.

Table 4.7 – Evaluation of cracks by means of DIC analysis.

Composite	Average number of cracks	Average crack width (μm)	Average crack spacing (mm)
NaGP	52.5	64.08	1.34
NaGP+A	66.25	62.45	1.13
KGP	38.5	62.37	1.57
KGP+A	43.5	59.37	1.85

Figure 4.13 presents the microstructure of the fracture surfaces of the composites after complete failure in the uniaxial tension tests.

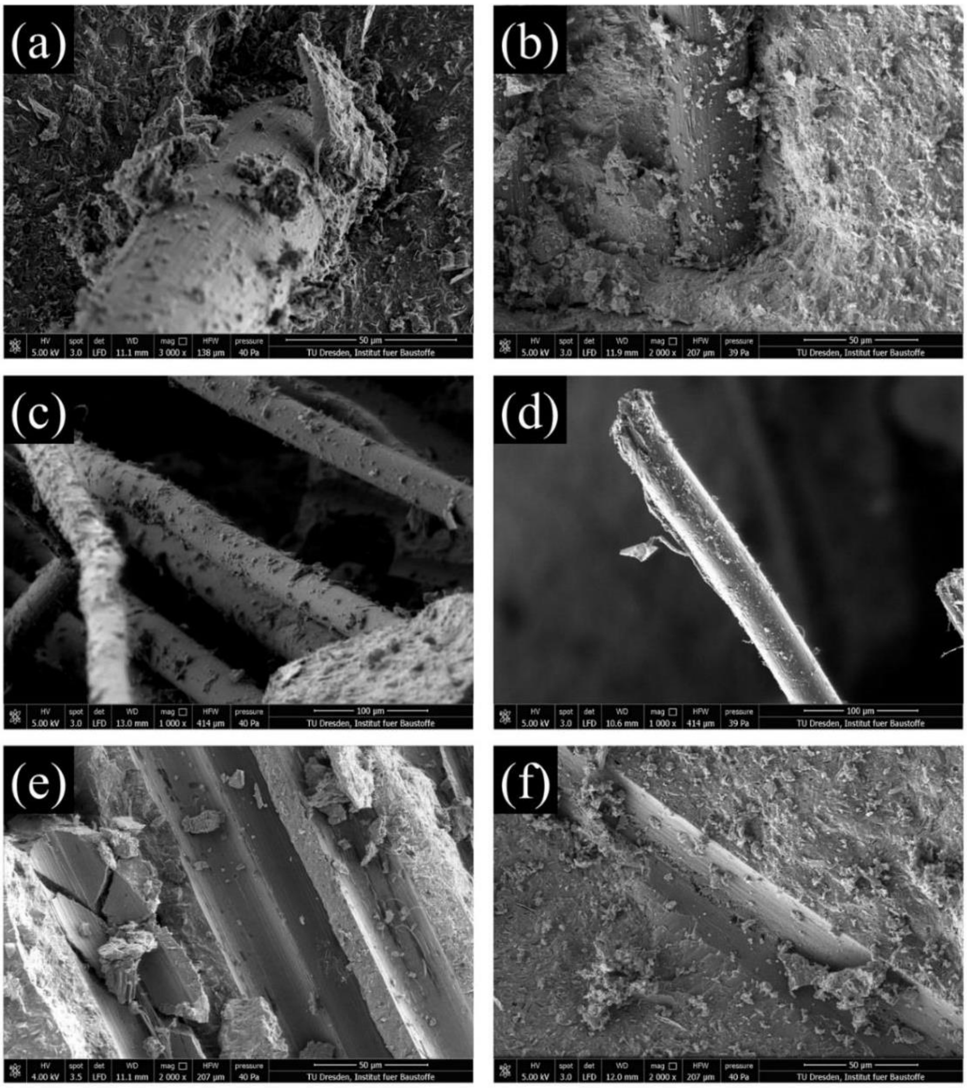

Figure 4.13 – Condition of the fibers and matrix on the fracture surfaces of (a,c,e) NaGP and (b,d,f) KGP geopolymer composites.

Figures 4.13a and b show the embedment of the fibers in the matrices, demonstrating adequate interaction for both K-based and Na-based materials, without any evident fiber surface damage. Figures 4.13c and d show the external surfaces of the partially pulled out fibers; once again, no deterioration can be observed. Micrographs also revealed some regions of fiber agglomerations for all mixtures under investigation, exemplarily shown here in Figure 4.13c. This finding points out a need for enhancing the rheology of the fresh mixture as well as mixing procedure. Figures 4.13e and f depict the channels left in the matrix after fiber pullout, confirming the occurrence of partial fiber debonding. The images clearly show the high homogeneity of the NaGP matrix and its pronounced brittleness, marked by the fine loose fragments. The microstructure of the same matrix enriched with sand was also investigated in ESEM, but no clear distinctions were observed. Figure 4.14 presents a comparison of the stress-strain behavior of SHGC investigated in this study with a typical SHCC response [57].

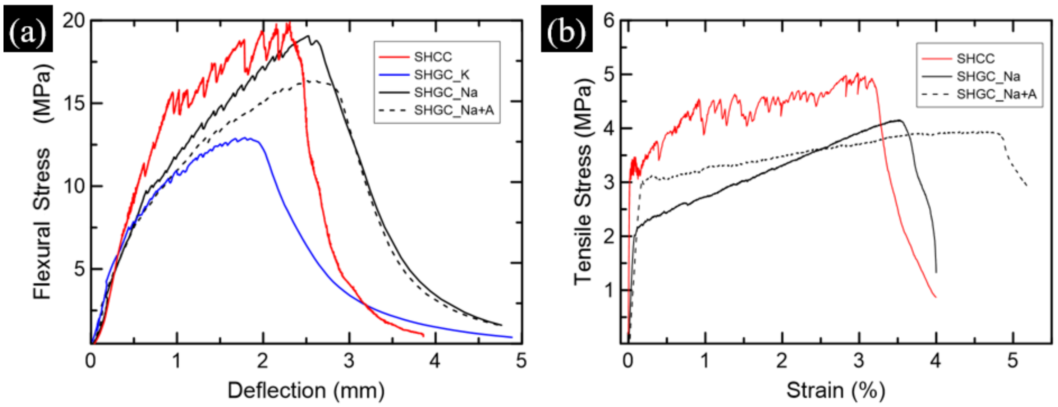

Figure 4.14 – Comparison of mechanical behavior of SHGC and SHCC (SHCC data from [57]).

By plotting the representative curves together, it can be affirmed that similar overall mechanical performance was obtained for Na-based SHGC, with flexural strength close to 20 MPa both for SHCC and SHGC. At the same time, individual properties of these mixtures differ more evidently: Cement-based materials exhibit a higher Young’s modulus of 13.6 GPa and higher tensile strength of approximately 5 MPa [57]. Worth noting is also the explicit indication of crack formation in SHCC by sudden stress drops in the stress-strain curves, while the corresponding curves for SHGC are much smoother. While lower crack widths and high crack density in

SHGC certainly contribute to this type of response, we need to look in detail at possible distinctions in fiber-matrix adhesive and frictional bonds as well. These features may also be interesting for applications with dynamic loading and requirements of long-term durability. Furthermore, the little difference in the density of the matrix and the fibers in the case of geopolymers may contribute to better fiber dispersion and consequently to improved crack control. Note that the cement-based materials have a density of 2.01 g/cm³ as opposed to those made of GP with 1.49 to 1.77 g/cm³; the density of PVA fibers is 1.26 g/cm³.

The pullout tests results are presented in Figure 4.15 and Table 4.8. The shear (adhesive and frictional) stresses were evaluated using the following equations [34,35]:

$$\tau_{\text{adhesional}} = \frac{P_{ad}}{2\pi r L} \quad (12)$$

$$\tau_{\text{frictional}} = \frac{P_{fr}}{2\pi r L} \quad (13)$$

where P_{ad} and P_{fr} are the adhesive and frictional forces, r is the radius of the fiber and L is the embedded fiber length.

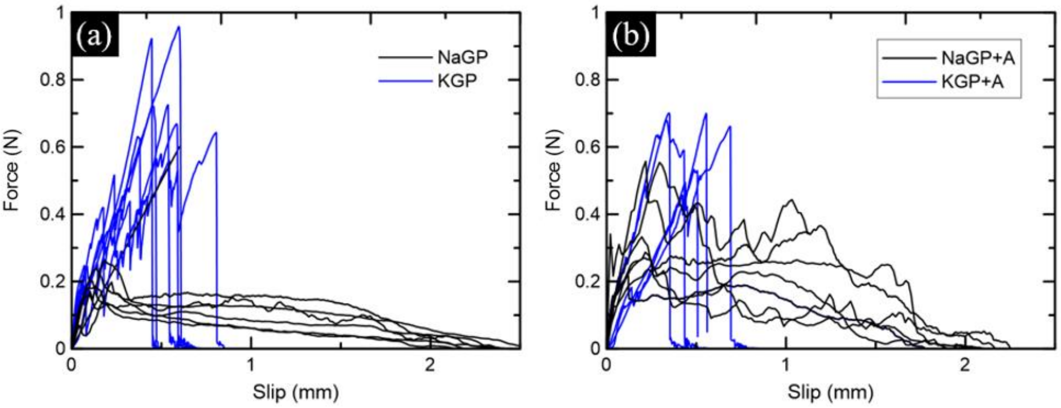

Figure 4.15 – Behavior of PVA fibers when pulled out from (a) NaGP and KGP matrices and (b) NaGP and KGP matrices enriched with aggregates.

Figure 4.15 shows typical pullout curves for geopolymer mixtures with and without aggregates. For Na-based compositions a complete pullout of the fibers could be observed, which is indicated by the relatively steady and long descending branches of force-slip displacement curves. NaGP without sand demonstrated lower average force values at adhesive failure and friction activation, 0.186 and 0.141 N, respectively, with the maximum force recorded in the initial part of the curve. In contrast, the mixture NaGP+A demonstrated greater adhesive and frictional forces, with the maximum occurring in the frictional phase (average value of 0.361 N).

Table 4.8 – Results of pullout tests.

Composite	Pa (N)	Pb (N)	Pmáx (N)	σa (MPa)	σb/δ0 MPa)	σmáx (MPa)	Gd (J/m^2)	Jb' (N/m)
NaGP	0.186 (0.032)	0.141 (0.031)	0.218 (0.058)	0.741 (0.131)	0.557 (0.124)	0.871 (0.233)	0.019 (0.016)	3.52 (1.70)
NaGP+A	0.341 (0.122)	0.235 (0.056)	0.361 (0.113)	1.358 (0.486)	0.935 (0.224)	1.438 (0.451)	0.129 (0.153)	9.56 (4.51)
KGP	0.595 (0.133)	-	0.595 (0.133)	2.214 (0.525)	-	2.214 (0.525)	2.57 (1.232)	-
KGP+A	0.574 (0.249)	-	0.574 (0.249)	2.269 (0.992)	-	2.269 (0.992)	2.88 (1.395)	-

Note that in common PVA-SHCC matrices, the pullout of the PVA fibers is accompanied by pronounced surface damage, partly caused by the cohesive interfacial failure and partly by the low abrasion resistance of the fibers [58, 59]. The interfacial damage mechanisms result in slip-hardening pullout behavior, leading to fiber rupture after just short pullout phases. On the contrary, the anchorage of the PVA fibers in the NaGP matrix results in a slip-softening behavior, indicating a dramatic reduction of the chemical adhesion. This behavior may be related to the: (i) hydrophilic nature of the fiber, which generates a much greater chemical adhesion in mixtures with higher water content; (ii) inadequate polarity between the oil coating and the fresh GP mixtures; and (iii) difference in the chemical composition and morphology of the matrix resulting from geopolymerization. Moreover, the slip-softening pullout behavior shows that the fibers do not suffer surface damage during pullout, which is likely due to high matrix homogeneity at the microscopic level. The addition of sand seems to roughen the walls of the fiber channel, leading to slight slip-hardening, as shown in Figure 4.14b.

The K-based compositions yielded pullout behavior similar to that observed in cementitious matrices [58,59], i.e., strong chemical adhesion and slip-hardening with complete fiber rupture. Given the flexural and tensile properties of the corresponding composites, the importance of a balanced fiber-matrix interaction and the negative effect of the strong slip-hardening pullout must be explicitly highlighted.

Regarding fracture mechanics: Since there is no occurrence of frictional loads for KGP-based materials, the complementary energy values $J_{b'}$ tend to be very low; they depend fully on the difference between frictional bond strength P_b and chemical adhesion G_d. In contrast, in the case of Na-based mixtures it was possible to calculate the complementary energy, which resulted in values of 3.52 N/m and 9.56 N/m for composition without and with aggregates, respectively. Herewith, Na-based SHGC containing fine sand exhibit similar behavior to that of SHCC, for which typical J_b values range between 9.6 and 10.7 N/m [56].

This brings us to the criteria for the occurrence of pseudo-strain-hardening. The $PSH_{tension}$ value of 2.7 obtained for NaGP composites without aggregates is higher than that calculated for the same parameter variations with KGP, where 1.38 was observed. PSH_{energy} appears as the main variable in the estimation of composite behavior. The value obtained for KGP-based materials is not representative due to the dominance of chemical adhesion between fiber and matrix, as mentioned previously. As for NaGP composites, a large value variation can be observed with the addition of aggregates, mainly influenced by the frictional adhesion, resulting in a PSH_{energy} value of 4.51, as opposed to 1.33 found for plain NaGP matrix. In the literature it is possible to find indications for better efficiency with $PSH_{energy} > 3$ [56], which would theoretically result in micro-crack formation saturation in the composite. This is exactly what occurs in case of NaGP with aggregates.

4.5. Conclusions

The results of the experimental investigations showed that Na-based geopolymer (GP) mixtures exhibited lower flowability and workability in the fresh state while achieving higher density and lower porosity in comparison with K-based GP. This resulted in higher tensile, flexural and compressive strengths and well as in higher Young’s moduli of the NaGP compositions. The addition of fine quartz sand caused a decrease in the workability of the fresh mixtures, both Na- and K-based, but enhanced their Young’s moduli and first-crack stress level. The use of PVA fibers improved not only the tensile strength and ductility of the composites, but also enhanced their compressive behavior, acting as an internal micro-confinement.

The fiber reinforcement was effective in ensuring typical strain-hardening behavior under tensile loading, accompanied by pronounced multiple cracking. Na-based strain-hardening geopolymer composites (SHGC) with and without fine sand yielded strain capacities of 3.5% and 4.7% strains, respectively. K-based SHGC without aggregates achieved only 2.6% on average, while K-based composites containing both fiber and aggregates exhibited strain-softening behavior.

Pullout tests made possible a comprehensive analysis of the fiber-matrix interactions, evidencing a more balanced fiber anchorage for NaGP composites, with improvements in the frictional adhesion supported by the addition of aggregates. In contrast, KGP composites showed strong chemical adhesion between fiber and matrix, which led to fiber failure rather than to proper debonding. The calculated pseudo-strain-hardening criteria based on the concepts of fracture mechanics confirmed the better standing of Na-based composites with respect to tensile ductility.

DIC evaluations of crack formation showed that the SHGC compositions developed exhibited full crack saturation with crack widths of 60 µm and average crack spacing of around 1.4 mm. When compared to the typical behavior of strain-hardening cement-based composites (SHCC), it was found that SHGC showed smaller crack widths, but a larger number of cracks. Thus, in summary improved strain capacity and smoother shape of the stress-strain curves were observed in the case of SHGC. This indicates the great potential of this material for a wide range of applications, including structural elements subject to dynamic loading or harsh chemical environments.

4.6.References

[1] Li, V. C. (2003). On engineered cementitious composites (ECC) a review of the material and its applications. Journal of advanced concrete technology, 1(3), 215-230.

[2] Mechtcherine, V. (2013). Novel cement-based composites for the strengthening and repair of concrete structures. Construction and building materials, 41, 365-373.

[3] Aveston, J., & Kelly, A. (1973). Theory of multiple fracture of fibrous composites. Journal of Materials Science, 8(3), 352-362.

[4] van Zijl, G. P., Wittmann, F. H., Oh, B. H., Kabele, P., Toledo Filho, R. D., Fairbairn, E. M., ... & Lepech, M. D. (2012). Durability of strain-hardening cement-based composites (SHCC). Materials and structures, 45(10), 1447-1463.

[5] Mechtcherine, V., de Andrade Silva, F., Müller, S., Jun, P., & Toledo Filho, R. D. (2012). Coupled strain rate and temperature effects on the tensile behavior of strain-hardening cement-based composites (SHCC) with PVA fibers. Cement and Concrete Research, 42(11), 1417-1427.

[6] Yun, H. D., Kim, S. W., Lee, Y. O., & Rokugo, K. (2011). Tensile behavior of synthetic fiber-reinforced strain-hardening cement-based composite (SHCC) after freezing and thawing exposure. Cold regions Science and technology, 67(1-2), 49-57.

[7] Müller, S., & Mechtcherine, V. (2017). Fatigue behaviour of strain-hardening cement-based composites (SHCC). Cement and Concrete Research, 92, 75-83.

[8] Qian, S., & Li, V. C. (2008). Simplified inverse method for determining the tensile properties of strain hardening cementitious composites (SHCC). Journal of Advanced Concrete Technology, 6(2), 353-363.

[9] Curosu, I., Liebscher, M., Mechtcherine, V., Bellmann, C., & Michel, S. (2017). Tensile behavior of high-strength strain-hardening cement-based composites (HS-SHCC) made with high-performance polyethylene, aramid and PBO fibers. Cement and Concrete Research, 98, 71-81.

[10] Curosu, I., Mechtcherine, V., Forni, D., & Cadoni, E. (2017). Performance of various strain-hardening cement-based composites (SHCC) subject to uniaxial impact tensile loading. Cement and Concrete Research, 102, 16-28.

[11] Lepech, M. D., & Li, V. C. (2009). Application of ECC for bridge deck link slabs. Materials and Structures, 42(9), 1185-1195.

[12] Li, V. C. (2019). Sustainability of Engineered Cementitious Composites (ECC) Infrastructure. In Engineered Cementitious Composites (ECC) (pp. 261-312). Springer, Berlin, Heidelberg.

[13] Choi, W. C., Yun, H. D., Kang, J. W., & Kim, S. W. (2012). Development of recycled strain-hardening cement-based composite (SHCC) for sustainable infrastructures. Composites Part B: Engineering, 43(2), 627-635.

[14] Schneider, M., Romer, M., Tschudin, M., & Bolio, H. (2011). Sustainable cement production—present and future. Cement and concrete research, 41(7), 642-650.

[15] Shi, C., Jiménez, A. F., & Palomo, A. (2011). New cements for the 21st century: The pursuit of an alternative to Portland cement. Cement and concrete research, 41(7), 750-763.

[16] Davidovits, J. (1991). Geopolymers: inorganic polymeric new materials. Journal of Thermal Analysis and calorimetry, 37(8), 1633-1656.

[17] Purdon, A. O. (1940). The action of alkalis on blast-furnace slag. Journal of the Society of Chemical Industry, 59(9), 191-202.

[18] Glukhovsky, V. D. (1967). Soil silicate articles and structures. Russian, Budivel'nyk Publish., Kiev.

[19] Vickers, L., Van Riessen, A., & Rickard, W. D. (2015). Fire-resistant geopolymers: role of fibres and fillers to enhance thermal properties. Springer Singapore.

[20] Lyon, R. E., Balaguru, P. N., Foden, A., Sorathia, U., Davidovits, J., & Davidovics, M. (1997). Fire-resistant aluminosilicate composites. Fire and materials, 21(2), 67-73.

[21] Davidovits, J. (1994). Geopolymers: man-made rock geosynthesis and the resulting development of very early high strength cement. Journal of Materials education, 16, 91-91.

[22] Kriven, W. M., Bell, J. L., & Gordon, M. (2003). Microstructure and microchemistry of fully-reacted geopolymers and geopolymer matrix composites. Ceramic Transactions, 153(1994), 227-250.

[23] Sankar, K., Stynoski, P., Al-Chaar, G. K., & Kriven, W. M. (2018). Sodium silicate activated slag-fly ash binders: Part I–Processing, microstructure, and mechanical properties. Journal of the American Ceramic Society, 101(6), 2228-2244.

[24] Fletcher, R. A., MacKenzie, K. J., Nicholson, C. L., & Shimada, S. (2005). The composition range of aluminosilicate geopolymers. Journal of the European Ceramic Society, 25(9), 1471-1477.

[25] Trindade, A. C. C., Borges, P. H. R., & de Andrade Silva, F. (2019). Evaluation of Fiber–Matrix Bond in the Mechanical Behavior of Geopolymer Composites

Reinforced with Natural Fibers. Advances in Civil Engineering Materials, 8(3), 361-375.

[26] Provis, J. L., & Van Deventer, J. S. J. (Eds.). (2009). Geopolymers: structures, processing, properties and industrial applications. Elsevier.

[27] Alcamand, H. A., Borges, P. H., Silva, F. A., & Trindade, A. C. C. (2018). The effect of matrix composition and calcium content on the sulfate durability of metakaolin and metakaolin/slag alkali-activated mortars. Ceramics International, 44(5), 5037-5044.

[28] Trindade, A. C. C., Alcamand, H. A., Borges, P. H. R., & Silva, F. A. (2017). On the durability behavior of natural fiber reinforced geopolymers. Ceramic and Science Proceedings, 38(3), 215-228.

[29] Duxson, P., Provis, J. L., Lukey, G. C., Mallicoat, S. W., Kriven, W. M., & Van Deventer, J. S. (2005). Understanding the relationship between geopolymer composition, microstructure and mechanical properties. Colloids and Surfaces A: Physicochemical and Engineering Aspects, 269(1-3), 47-58.

[30] Zhuang, X. Y., Chen, L., Komarneni, S., Zhou, C. H., Tong, D. S., Yang, H. M., ... & Wang, H. (2016). Fly ash-based geopolymer: clean production, properties and applications. Journal of Cleaner Production, 125, 253-267.

[31] Menna, C., Asprone, D., Ferone, C., Colangelo, F., Balsamo, A., Prota, A., ... & Manfredi, G. (2013). Use of geopolymers for composite external reinforcement of RC members. Composites Part B: Engineering, 45(1), 1667-1676.

[32] Dias, D. P., & Thaumaturgo, C. (2005). Fracture toughness of geopolymeric concretes reinforced with basalt fibers. Cement and concrete composites, 27(1), 49-54.

[33] Ohno, M., & Li, V. C. (2014). A feasibility study of strain hardening fiber reinforced fly ash-based geopolymer composites. Construction and Building Materials, 57, 163-168.

[34] Nematollahi, B., Sanjayan, J., & Ahmed Shaikh, F. U. (2015). Tensile strain hardening behavior of PVA fiber-reinforced engineered geopolymer composite. Journal of Materials in Civil Engineering, 27(10), 04015001.

[35] Ohno, M., & Li, V. C. (2018). An integrated design method of Engineered Geopolymer Composite. Cement and Concrete Composites, 88, 73-85.

[36] Nematollahi, B., Sanjayan, J., Qiu, J., & Yang, E. H. (2017). Micromechanics-based investigation of a sustainable ambient temperature cured one-part strain

hardening geopolymer composite. Construction and Building Materials, 131, 552-563.

[37] Nematollahi, B., Sanjayan, J., & Shaikh, F. U. A. (2016). Matrix design of strain hardening fiber reinforced engineered geopolymer composite. Composites Part B: Engineering, 89, 253-265.

[38] Batista, R. P., Trindade, A. C. C., Borges, P. H., & Silva, F. D. A. (2019). Silica fume as precursor in the development of sustainable and high-performance MK-based alkali-activated materials reinforced with short PVA fibers. Frontiers in Materials, 6, 77.

[39] Bell, J. L., Driemeyer, P. E., & Kriven, W. M. (2009). Formation of ceramics from metakaolin-based geopolymers. Part II: K-based geopolymer. Journal of the American Ceramic Society, 92(3), 607-615.

[40] ASTM C1437-15, Standard Test Method for Flow of Hydraulic Cement Mortar, ASTM International, West Conshohocken, PA, 2015, www.astm.org.

[41] ASTM C230 / C230M-14, Standard Specification for Flow Table for Use in Tests of Hydraulic Cement, ASTM International, West Conshohocken, PA, 2014, www.astm.org

[42] ASTM D6910 / D6910M-09, Standard Test Method for Marsh Funnel Viscosity of Clay Construction Slurries (Withdrawn 2018), ASTM International, West Conshohocken, PA, 2009, www.astm.org

[43] ASTM C138 / C138M-17a, Standard Test Method for Density (Unit Weight), Yield, and Air Content (Gravimetric) of Concrete, ASTM International, West Conshohocken, PA, 2017, www.astm.org

[44] BS EN 196-1: 2016. Methods of testing cement. Part 1: Determination of strength.

[45] Rinne, H. (2008). The Weibull distribution: a handbook. CRC press.

[46] de Andrade Silva, F., Chawla, N., & de Toledo Filho, R. D. (2008). Tensile behavior of high performance natural (sisal) fibers. Composites Science and Technology, 68(15-16), 3438-3443.

[47] Li, V. C., Wu, C., Wang, S., Ogawa, A., & Saito, T. (2002). Interface tailoring for strain-hardening polyvinyl alcohol-engineered cementitious composite (PVA-ECC). Materials Journal, 99(5), 463-472.

[48] Li, V. C., Wang, S., & Wu, C. (2001). Tensile strain-hardening behavior of polyvinyl alcohol engineered cementitious composite (PVA-ECC). Materials Journal, 98(6), 483-492.

[49] Peterson, P. E. (1980). Fracture energy of concrete: Method of determination. Cement and Concrete research, 10(1), 79-89.

[50] Karihaloo, B. L., & Nallathambi, P. (1990). Effective crack model for the determination of fracture toughness (KICe) of concrete. Engineering Fracture Mechanics, 35(4-5), 637-645.

[51] He, P., Wang, M., Fu, S., Jia, D., Yan, S., Yuan, J., ... & Zhou, Y. (2016). Effects of Si/Al ratio on the structure and properties of metakaolin based geopolymer. Ceramics international, 42(13), 14416-14422.

[52] Braga, M., De Brito, J., & Veiga, R. (2012). Incorporation of fine concrete aggregates in mortars. Construction and Building Materials, 36, 960-968.

[53] Rahman, A. S. (2015). Nanofiber reinforcement of a geopolymer matrix for improved composite materials mechanical performance (Doctoral dissertation, Colorado State University).

[54] Cho, S. (2015). Geopolymer composites and their applications in stress wave mitigation. University of Illinois at Urbana-Champaign.

[55] Pires, E. F. C., Azevedo, C. M. C. D., Pimenta, A. R., Silva, F. J. D., & Darwish, F. A. I. (2017). Fracture properties of geopolymer concrete based on metakaolin, fly ash and rice rusk ash. Materials Research, 20, 630-636.

[56] Van Zijl, G. P. A. G., & Wittmann, F. H. (Eds.). (2010). Durability of strain-hardening fibre-reinforced cement-based composites (SHCC) (Vol. 4). Springer Science & Business Media.

[57] Curosu, I. (2018). Influence of fiber type and matrix composition on the tensile behavior of strain-hardening cement-based composites (SHCC) under impact loading.

[58] Drechsler, A., Frenzel, R., Caspari, A., Michel, S., Holzschuh, M., Synytska, A., ... & Mechtcherine, V. (2019). Surface modification of poly (vinyl alcohol) fibers to control the fiber-matrix interaction in composites. Colloid and Polymer Science, 297(7), 1079-1093.

[59] Ranjbarian, M., Mechtcherine, V., Zhang, Z., Curosu, I., Storm, J., & Kaliske, M. (2019). Locking Front Model for pull-out behaviour of PVA microfibre embedded in cementitious matrix. Cement and Concrete Composites, 103, 318-330.

5 Tensile behavior of strain-hardening geopolymer composites (SHGC) under impact loading

5.1. Introduction

The high brittleness and low tensile strength of plain mineral-based materials do not facilitate a favorable mechanical response when subjected to dynamic loadings, such as caused by earthquakes, explosions, or impact [1]. Since steel reinforcement often does not provide sufficient enhancement in structural ductility [2], strengthening solutions for existing critical infrastructure should be developed. Particulate [3] and, more effectively, fibrous reinforcements [4,5] can be used to improve the ductility and energy absorption of cementitious materials [4,6]. Compelling examples of such composites are the textile-reinforced concretes (TRC) [7,8] and the strain-hardening cementitious composites (SHCC) [4-6], both yielding promising features for impact-resistant strengthening layers [9,10].

SHCC, also named Engineered Cementitious Composites (ECC), are made of fine-grained cement-based matrices and short synthetic micro-fibers in volume contents of up to 2 %. These composites exhibit a strain-hardening tensile behavior accompanied by the formation of multiple, fine cracks up to failure localization [7,11], both under quasi-static and dynamic loads [12,13]. However, considering that these high-performance composites require relatively high cement content, there is room for improvement in terms of sustainability [14]. For this reason, alternatives must be explored, such as the use of geopolymers (GP), which enable comparable mechanical properties by combining aluminosilicate sources with alkaline solutions [15,16]. Additionally, GP exhibit high resistance under elevated temperatures of up to 1000 ºC [17,18], and against highly aggressive chemical attacks [19].

Given the fine-grained nature of the GP matrices, the micromechanical concepts of SHCC are also applicable for achieving strain-hardening geopolymer composites (SHGC). Previous studies have pointed out the promising behavior of SHGC when subjected to quasi-static tensile loading, reaching higher deformation capacity when compared to SHCC of similar mechanical strength [20]. Furthermore, GP materials yield a lower Young’s modulus (approximately 10 GPa) than their cementitious counterparts [21], which may be favorable for repair and strengthening applications in cases of dynamic loading. Investigations into the dynamic behavior of SHGC are limited. Khan *et al.* [22] demonstrated a strong rate-dependent enhancement of the compressive strength of heat-cured fly-ash based GPs as tested in a split Hopkinson pressure bar (SHPB). Menna *et al.* [23] and Khan *et al.* [24] reported similar responses for heat-cured and unheated GPs based on metakaolin and fly-ash, respectively. Based on dynamic splitting tensile tests in an SHPB, they reported little to no influence of the curing regimes. Moreover, significant improvements were observed in terms of strength and strain capacity by changing the reinforcement from steel fibers to polyethylene fibers.

As opposed to the compressive impact behavior of SHGC, their dynamic tensile behavior has not been analyzed so far. Considering that the tensile behavior of SHCC is highly rate-dependent both in terms of tensile strength and strain capacity [6], corresponding investigations must be performed on SHGC to assess the effect of loading rate and material composition on their mechanical performance.

The paper at hand presents an extensive investigation on the dynamic tensile behavior of two types of SHGC at the composite and fiber levels, as well as the behavior of the corresponding plain matrix. The impact tension tests on the non-reinforced and fiber-reinforced GPs were performed using a split Hopkinson tension bar (SHTB) specifically developed for ductile composites such as SHCC [13]. The setup facilitates accurate material characterization under impact tensile loading in terms of force-displacement (stress-strain) relationships. The plain GP was based on metakaolin combined with a Na-based solution, while the corresponding SHGCs were made with PVA and UHMWPE fibers in volume fractions of 2 %. The impact tension tests were monitored with a high-speed stereo camera system, which enabled the description and quantification of the fracture mechanisms in the loaded samples using Digital Image Correlation (DIC). Optical microscopy and ESEM analyses were performed on the fracture surfaces of tested composite specimens. Dynamic single-fiber pullout tests were performed in a purposefully designed miniature SHTB and their results were compared to the quasi-static responses measured in an electromechanically actuated testing machine. Additionally, a comparative assessment was carried out between the impact behavior of SHGC and previously investigated SHCC.

5.2. Experimental program

5.2.1. Materials and specimen production

A combination of the aluminosilicate source metakaolin (MK) with a Na-alkali-based solution, i.e., water-glass (WG), was used to produce the geopolymer (GP) mixture evaluated in this study. It represents the well-known final composition of $Na_2O \cdot Al_2O_3 \cdot 4SiO_2 \cdot 11H_2O$ [16,25]. Metakaolin ($Al_2O_3 \cdot 2SiO_2$) was chosen as the main aluminosilicate source, mostly due to its high level of purity, enabling adequate reactivity. Sodium hydroxide in pellets (reagent grade > 90%) was dissolved in deionized water, where hydrophilic fumed silica was added and mixed for 24 h using a magnetic stirrer, thus forming the stable water-glass solution ($Na_2O \cdot 2SiO_2 \cdot 11H_2O$). Quartz fine sand with a maximum diameter of 0.2 mm was incorporated into the mix as a natural aggregate in a 50 % mass fraction to metakaolin.

PVA and UHMWPE (short PE) fibers were used as dispersed reinforcement in the GP in a volume content of 2.0 %. This allowed for a comparative assessment of the influence of the fiber properties on the interaction with the GP matrix and, finally, on composite behavior. Table 5.1 summarizes the physical and mechanical properties of the fibers under investigation. An overview of the material combinations used in this study is presented in Table 5.2.

Table 5.1 – Physical and mechanical properties of the PVA and PE fibers under investigation.

Fiber type	PVA	PE
Producer	Kuraray (Japan)	DSM (The Netherlands)
Brand	Kuralon® K-II REC15	Dyneema® SK62
Length [mm]	12	12
Nominal diameter [µm]	40	20
Density [g/cm^3]	1.26	0.97
Tensile strength [MPa]	1600	2500
Young’s modulus [GPa]	40	80
Elongation at break [%]	7	3.5

Table 5.2 – Mixture composition for each material variation.

Composite	NaGP	SHGC$_{PVA}$	SHGC$_{PE}$
WG/MK ratio	1.712		
WG [g]	1000		
MK [g]	584		
Sand [g]	292		
PVA % by vol.		2.0	-
PE % by vol.	-	-	2.0

A 10-liter planetary mixer was used to prepare the GP-based composites. The mixing procedure was as follows: (i) mixing of MK and WG in proper amounts for 3 min with an intermediate speed of 198 rpm to ensure an adequate reactivity; (ii) addition of aggregates (quartz sand); (iii) mixing for 1 min with an intermediate speed of 198 rpm; (iv) addition of fibers (PVA or PE); (v) mixing for 3 min at a higher speed of 365 rpm to ensure proper fiber distribution. The fresh mixtures were then cast in molds with a 1 min vibration step for consolidation and extraction of air voids. The molds were sealed in plastic bags for 48 h to prevent early dehydration. Beams with dimensions of 160 mm x 40 mm x 40 mm were produced for plain NaGP matrix, PVA fiber-reinforced NaGP composite - SHGC$_{PVA}$, and PE fiber-reinforced NaGP composite - SHGC$_{PE}$. The use of steel molds usually causes difficulties in specimen extraction; accordingly, semitransparent adhesive tape was used to cover and protect the steel parts, allowing and facilitating specimen extraction after 48 h. The extracted beam-like samples were cured inside dry plastic bags for two weeks. This curing regime was adopted from Kriven *et al.* [25] as the time required for a slow and gradual water loss to occur, preventing the drastic formation of cracks at early age. After demolding and curing, cylindrical specimens were core-drilled in the longitudinal direction of the beams. The cylindrical specimen geometry with a diameter of 22.5 mm was imposed by the split Hopkinson testing setup [13]. The specimens had lengths of 25 mm or 50 mm, depending on the testing regime, i.e. quasi-static or dynamic, respectively. The reason for this is explained in the next section.

The production of the single-fiber pullout specimens implied casting the matrix in a rectangular plastic mold, as shown in Figure 5.1. Three long plastic plates (two sturdy and one thinner) were bolted together, creating a longitudinal channel in the middle of the mold, with the width corresponding to the desired fiber embedment length of 2 mm. The fibers bridged the channel with a spacing of 10 mm between them, while their ends were fixed with wax to the mold. Two long plates were subsequently bolted on top of the first two sturdy ones, forming the complete height of the channel in which the GP matrix was finally cast. The curing regime was identical to that of the matrix and composite specimens. After demolding, the matrix rods obtained with their laterally protruding fibers were cut between neighboring fibers, resulting in ten single specimens with dimensions of approximately 6 mm x 6 mm x 2 mm, the latter dimension indicating the embedded length of the fibers. The preparation of the samples for testing assumed cutting the fibers on one side of the specimen and using wax to cover the fibers' cut ends and prevent their contact with the glue in the subsequent steps. Further details regarding specimen fixation in the testing device are presented in the next section.

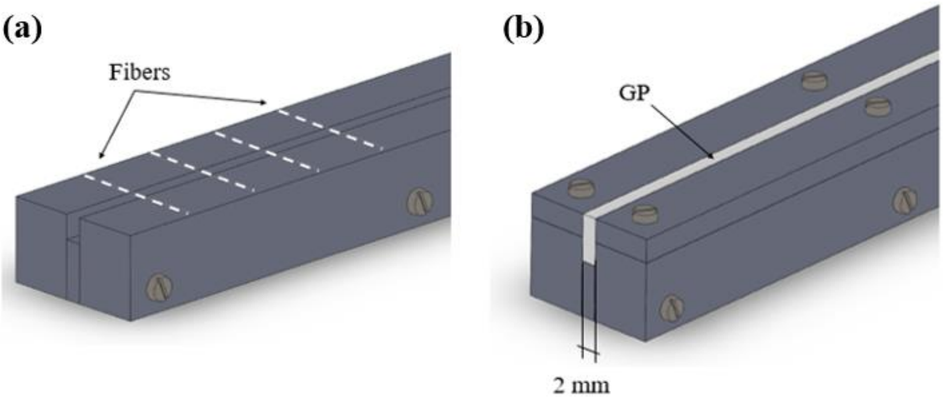

Figure 5.1 – Schematic view of the mold for single-fiber pullout specimens: (a) fiber positioning and (b) matrix casting.

5.2.2. Testing configurations

5.2.2.1. Quasi-static tension tests

Figure 5.2 presents the electro-mechanically actuated Zwick 1445 testing machine, that was used to perform the quasi-static tension tests on the plain matrix and fiber-reinforced composites at a displacement rate of 0.05 mm/s. The cylindrical specimens were glued at their ends in 12.5 mm-thick steel rings bolted to steel stamps and fixed in the testing machine through steel rods. This configuration ensured non-rotatable boundary conditions. The alignment of the specimens in the testing device was ensured by gluing the specimens first outside the machine in a specially fabricated frame. After one end was glued, the specimen was mounted in the upper cross-member and driven downwards into the second ring filled with glue. Note that the total specimen length of the quasi-statically tested specimens was 50 mm. This is because of the 12.5 mm embedment in the fixing rings. The free (gauge) length of the samples was 25 mm.

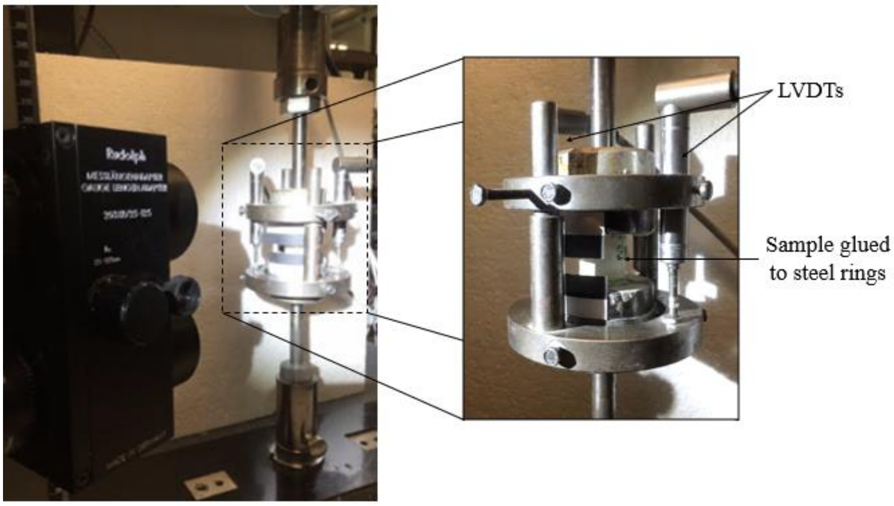

Figure 5.2 – Setup for quasi-static tension tests.

A fast-hardening, bi-component glue consisting of the fluid component DEGADUR®1801 and powder DEGADUR®7742 was used to glue the specimens. It was possible to run the tests after 10 minutes of glue hardening in the second ring. A circular steel frame was attached around the specimen on the steel stamps to support two Linear Variable Differential Transducers (LVDTs), which recorded the deformation of the loaded specimens. Three cylindrical specimens were tested for each material variation.

5.2.2.2. Gravity-driven split Hopkinson tension bar

The impact tension tests on plain matrix and fiber-reinforced specimens were performed in a gravity-driven split Hopkinson tension bar (SHTB). The device is described in detail in [13,26]. Figure 5.3 presents the test setup and specimen positioning. The setup consisted of an input bar, where the loading wave was induced; of a transmitter bar rigidly attached to an aluminum frame and in which the wave transmitted by the specimen was recorded; and of a striker system with a weight of 30 kg. The cylindrical specimen was sandwiched between the bars using a bi-component epoxy resin Barrafix EP (PCI). The loading pulse was generated by dropping the weight assembly onto the impact flange at the bottom of the input bar. The drop height was 3.5 m. The corresponding peak displacement rate was 7.5 m/s.

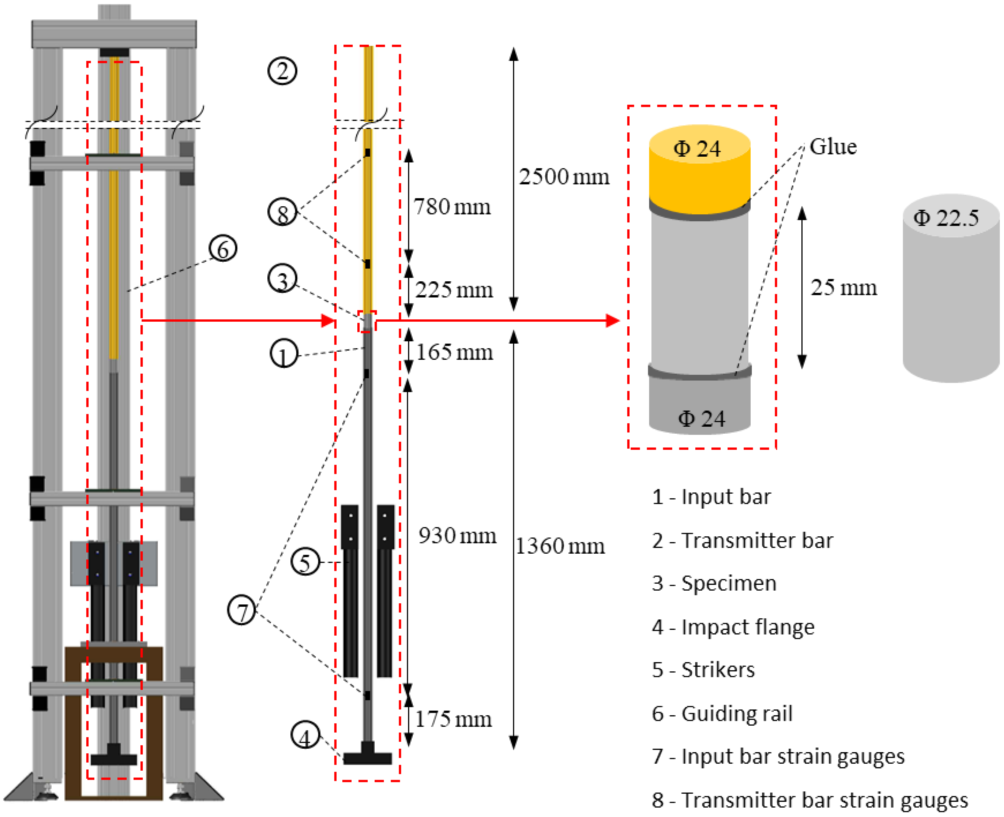

Figure 5.3 – Configuration and dimensions of the split Hopkinson tension bar [13,26].

At each strain measurement point on the bars, three strain gauges were positioned at 120 degrees relative to each other. The measurements were sampled with a rate of 1 MS/s and filtered subsequently with a zero-phase 60 kHz low-pass filter. Data acquisition was performed with two SIRIUSi HS-STG+.

Four cylindrical specimens were tested for each composite variation. Initially, one variation was tested in various lengths: 25 mm, 35 mm, and 50 mm, in order to determine the proper length concerning the dynamic stress equilibrium in the samples prior to crack formation. The equilibrium condition ensures a uniform stress state along with the sample, and it is a prerequisite to an accurate derivation of the material properties in split Hopkinson bar setups [27,28]. Reaching this state before the formation of the first crack is directly dependent on: (i) specimen length; (ii) tensile strength of the matrix; (iii) wave velocity in the material, i.e. Young's modulus and density; (iv) impedance mismatch between the sample and the bars; and (v) rise-time of the input loading wave. In the current study, only the length of the sample was adjusted until an acceptable match between the forces at both sample ends was achieved. Figure 5.4 presents the results obtained for two different specimen lengths, with a proper stress equilibrium recorded for 25 mm-long specimens only.

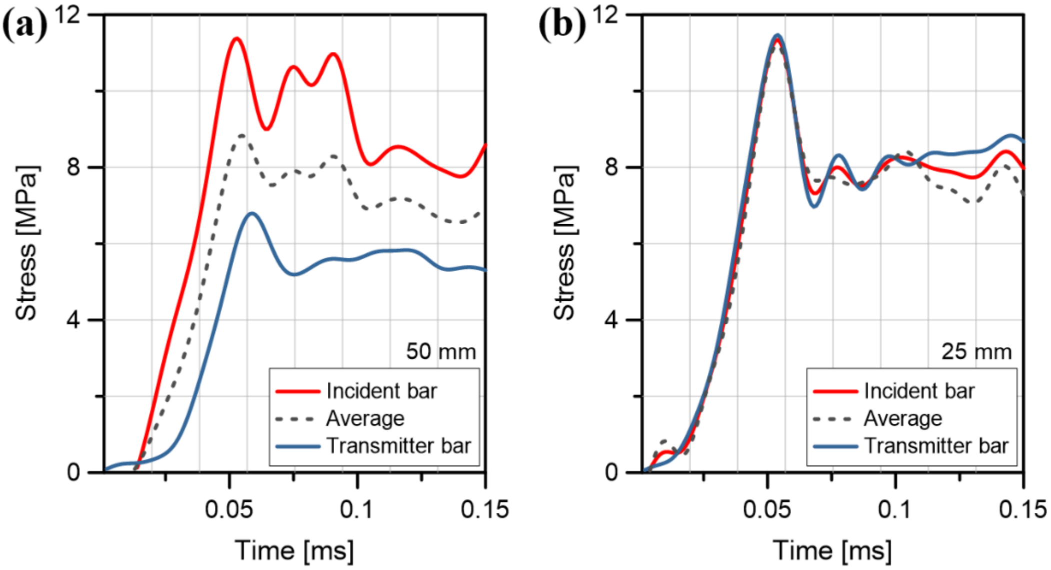

Figure 5.4 – Stress vs. time history at the ends of two SHGC specimens with different lengths of (a) 50 mm and (b) 25 mm.

The forces at both ends of the specimen must be compared to verify the equilibrium. In case an acceptable equilibrium is reached, the average value is considered for deriving the stress-strain relationships. The wave analysis is performed based on the theory of one-dimensional wave propagation [26,28]. The indices *i* and *t* refer to the calculations related to the two ends of the specimen in contact with the incident and transmitter bars, respectively. Eqs. 1 and 2 were used to calculate the forces acting at the ends of the sample using ε_I, ε_R, and ε_T which are the recorded input, reflected and transmitted waves, respectively.

$$F_i(t) = E_i A_i(\varepsilon_I(t) + \varepsilon_R(t)) \tag{1}$$

$$F_t(t) = E_t A_t \varepsilon_T(t) \tag{2}$$

The displacements were obtained with Eqs. 3 and 4, where C represents the elastic wave velocity in each bar.

$$\delta_i(t) = C_i \int_0^t (\varepsilon_I(t) - \varepsilon_R(t))\mathrm{dt} \tag{3}$$

$$\delta_t(t) = C_t \int_0^t (\varepsilon_T(t)\mathrm{dt} \tag{4}$$

The stress in the sample was calculated using Eq. 5, where A_s corresponds to the sample cross-sectional area, while the strain values were obtained through Eq. 6, in which L_s represents the sample length. Also, the strain rate could be calculated with Eq. 7, which corresponds to the relative displacement speed of the two ends of the sample divided by the sample length.

$$\sigma(t) = \frac{F_i(t)+F_t(t)}{2A_s} \tag{5}$$

$$\varepsilon(t) = \frac{\delta_i(t)+\delta_t(t)}{L_s} \tag{6}$$

$$\dot{\varepsilon}(t) = \frac{(\varepsilon_I(t)+\varepsilon_R(t))C_I - \varepsilon_T(t)\, C_T}{L_S} \tag{7}$$

5.2.2.3. Digital image correlation (DIC)

Digital Image Correlation (DIC) was used as a supplementary strain measurement tool as well as to monitor the multiple cracking and fracture processes. The samples were sprayed with a speckle pattern, consisting of a white base layer subsequently covered by a random dot pattern using a black color painting spray. The optical deformation measurements were performed with a high-speed stereo system consisting of two Photron SA-X2 cameras, capturing 150,000 frames per second with a resolution of 128 x 304 pixels. The frames were processed using the commercial software ARAMIS 5M, developed by GOM GmbH.

5.2.2.4. Microscopic analysis

A digital microscope VHX-6000, equipped with an 18 Megapixel, 1/1.8-inch, CMOS image sensor camera, and high brightness LED with a 3200 x 2400 resolution, was used to evaluate the failure modes of both quasi-statically and dynamically tested composites.

The state of the fibers on the fracture surfaces of the tested samples was assessed in an environmental scanning electron microscope (ESEM) Quanta 250 FEG equipped with an energy-dispersing X-ray analyzer (EDX). For this the system required a 40 Pa pressure and a 10 kV accelerating voltage, acquiring images in an 800 X magnification.

5.2.2.5. Quasi-static single-fiber pullout tests

Quasi-static single-fiber pullout tests were performed on both fiber-matrix combinations in a Zwick-Roell Z 1445 testing machine under a displacement rate of 0.05 mm/s using a 10 N load cell; see Figure 5.5.

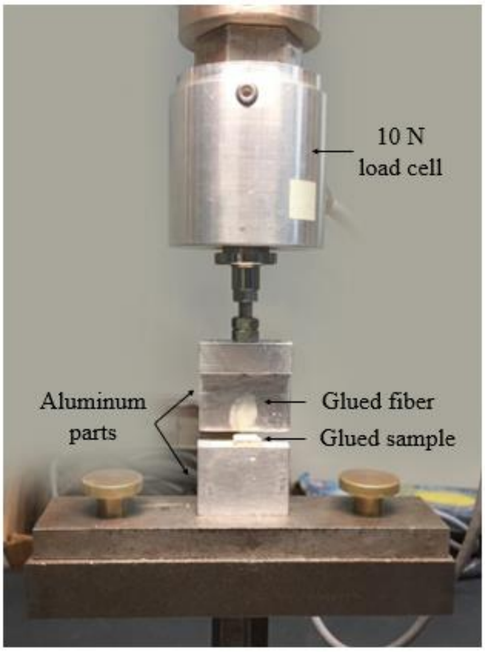

Figure 5.5 – Setup for quasi-static single-fiber pullout tests.

The displacement of the fibers was approximated as being the displacement of the machine cross-member. The specimens were fixed in the testing machine as follows: (i) gluing of the specimen onto a flat aluminum piece bolted to the lower, static cross-member of the machine and (ii) gluing of the fiber onto an aluminum plate, which was attached to the force sensor. Both the embedded length and the free length of the fibers were 2 mm. The tests could be started after 5 min of glue hardening.

5.2.2.6. Dynamic single-fiber pullout tests

A miniature SHTB was used to perform the dynamic pullout tests, similar to the equipment used by Cheng et al. [29] and Sanborn and Weerasooriya [30]. The setup consists of an aluminum incident bar with a diameter of 4 mm, a tubular striker, and a flange attached to the end of the bar. Figure 5.6 presents the setup configuration. The specimen is glued to a small tubular adapter attached to the incident bar, and the fiber is glued to an aluminum adapter attached to a piezoelectric load cell of type Kistler 9205. The pullout and rupture loads of the fibers were typically lower than 1 N, which did not allow the use of a conventional transmitter bar for measuring the output in terms of wave propagation. As soon as the striker reached the flange, the tensile pulse was generated, traveling through the incident bar towards the specimen and resulting in a pullout rate of 1000 mm/s. The maximum displacement caused by one wave passage was 0.5 mm, which was not enough for complete fiber pullout, but enough to reach the peak pullout force and derive the corresponding interfacial properties.

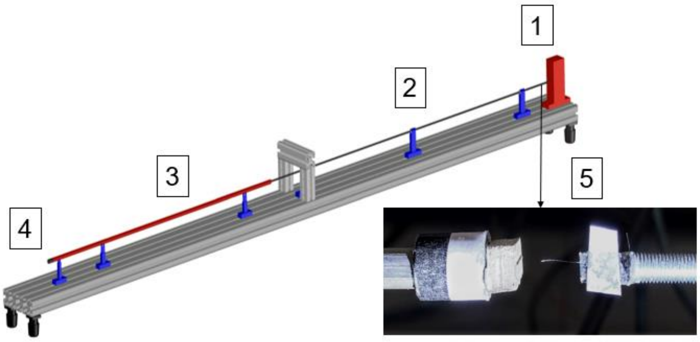

1. Block to fix piezoelectric force-cell
2. Input bar
3. Cylindrical striker
4. Impact flange
5. Sample and adapter with optical measurement target

Figure 5.6 – Setup for dynamic pullout tests.

Part of the incident (loading) wave is transmitted through the sample and the rest is reflected as a compression pulse. However, as the impedance of the fiber is significantly smaller than that of the bar, the transmitted wave is significantly weaker than the reflected compression wave. The displacement values were measured with a high-speed optical extensometer, which followed the target attached to the adapter where the specimens were glued.

The fiber-matrix bond strength was derived using Eq. 8, where P represents the maximum pullout load obtained from the load cell, r is the radius of the fiber, and L is the embedded fiber length.

$$\tau_{\text{bond}} = \frac{\text{P}}{2\pi r L} \tag{8}$$

5.3. Results and discussion

5.3.1. Quasi-static tension tests

Table 5.3 summarizes the results of the quasi-static tension tests on the GP matrix and on both SHGC reinforced with PVA and PE fibers, respectively. The GP matrix, having an average compressive strength of 57 MPa [31], showed a brittle fracture with an average tensile strength of only 1.7 MPa. A substantial increase in the matrix cracking stress was observed after the addition of fibers, as shown in Figure 5.7, where SHGC_{PVA} and SHGC_{PE} yielded first crack stresses of 2.9 MPa and 3.7 MPa, respectively. Note that in cementitious matrices the PVA fibers allow for pre-crack confinement of the matrix through the strong chemical bond, while the hydrophobic PE fibers are mostly activated after crack formation [6]. This effect was also demonstrated in high-strength SHCC made with different high-performance polymer fibers [32]. However, in the case of SHGC, the PVA fibers exhibit mainly a frictional bond, both in matrices with and without aggregates [31]. Thus, the increase in first crack stress is related to the reduction effect of crack bridging on the stress intensity at crack tip. The higher first crack stress in the case of SHGC_{PE} could be attributed to the smaller fiber diameter compared to PVA.

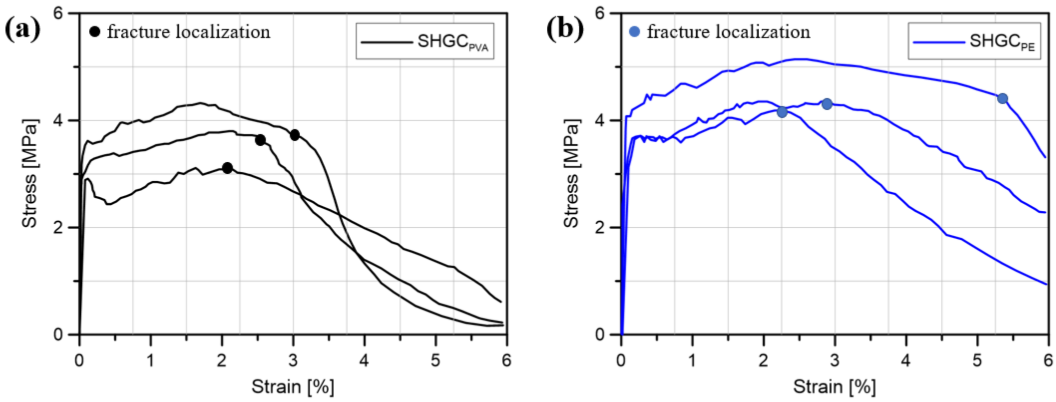

Figure 5.7 – Quasi-static tensile stress-strain curves of NaGP reinforced with: (a) PVA and (b) PE fibers (the filled circles on the curves indicate fracture localization).

Table 5.3 – Quasi-static tensile properties of plain GP and SHGC reinforced with PVA and PE fibers. Average values with standard deviations given in parentheses.

Composite	NaGP	$SHGC_{PVA}$	$SHGC_{PE}$
First crack stress [MPa]	1.7 (0.2)	2.9 (0.3)	3.7 (0.3)
Tensile strength [MPa]	-	4.1 (0.9)	4.7 (0.7)
Strain at fracture localization [%]	-	2.5 (0.5)	3.6 (0.8)
Work-to-fracture (up to softening) [kJ/m³]	-	87.9 (18.4)	152.2 (40.5)

The investigated composites yielded also different tensile strength and strain capacities. Note that not all the specimens yielded strain-hardening up to failure localization; some showed an initial stress peak with subsequent multiple cracking. Initiation of softening is indicated by the filled circles in the curves in Figure 5.7. In the paper at hand tensile strength corresponds to peak stress while the strain values were derived at fracture localization. $SHGC_{PVA}$ showed an average tensile strength (peak stress) of 4.1 MPa, while $SHGC_{PE}$ reached a slightly higher value of 4.7 MPa. Their respective strain capacities up to fracture localization were 2.5 % and 3.6 %. The higher tensile strength of $SHGC_{PE}$ can be attributed to the smaller diameter of the PE fibers, resulting in a greater number of filaments embedded in the matrix when compared to PVA. With the same volume fraction and with similar bond strength (as it will be demonstrated in Section 3.4), the collective crack-bridging action of the PE fibers is considerably higher.

The higher tensile strength and strain capacity of $SHGC_{PE}$ resulted in a higher work-to-fracture, which is represented by the area under the stress-strain curves up to fracture localization. SHGC reinforced with PVA and PE fibers yielded average work-to-fracture values of 87.9 kJ/m³ and 152.2 kJ/m³, respectively. Thus, in the case of quasi-static loading, the energy dissipation in the GP composites reinforced with PE fibers is 73 % higher in comparison to the composites made with PVA fiber.

5.3.2. Impact tension tests

The results of dynamic tension tests on the plain GP matrix are presented in Figure 5.8a and Table 5.4. A pronounced increase in tensile strength was recorded, when compared to the quasi-static responses, reaching an average of 11.2 MPa. The dynamic increase factor (DIF, the ratio of the dynamic value of a mechanical parameter to the corresponding quasi-static value) for the tensile strength of plain GP equals 6.5. Figure 5.8b presents the full-field strain measurement obtained by DIC at the moment of fracture localization, showing the only crack formed during the test. It can also be observed that the brittle nature of NaGP yields failure localization already during the rising phase of the input wave, i.e. before reaching a constant strain rate in the test.

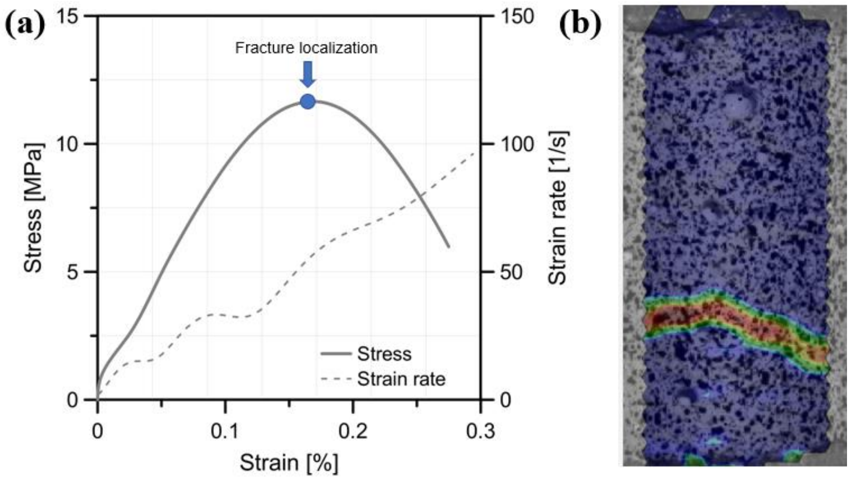

Figure 5.8 – Results of impact tension tests on plain NaGP matrix: (a) stress-strain and strain rate curves and (b) DIC image showing the fracture localization.

At this point it is possible to make an analogy with cementitious materials, where the influence of the loading rate on the apparent tensile strength depends on the crack-tip inertia [33], structural inertia activated during the acceleration phase in the ascending part of the loading wave [34] and by the softening during failure localization [35]. As a result, a considerably higher tensile strength is achieved by the samples tested at high strain-rate in split-Hopkinson tension bar [6,13]. It is worth mentioning that the structural inertia which is activated as a result of the softening of the sample is dependent on the fracture energy of the material. Materials with very low fracture energy, such as glass, present almost no rate sensitivity [35]. The fracture properties of the GP matrix under investigation were described in the previous study by the authors based on flexural tests [31].

Figure 5.9 and Table 5.4 present the results of dynamic tension tests on both SHGC. The values obtained for first crack stress agree with the dynamic tensile strength recorded for the plain GP, reaching 11.1 MPa for PVA and 10.1 MPa for PE-based SHGC, respectively. The corresponding DIFs for the first crack stress in both composites are 3.8 and 3.5. Thus, both SHGC show a very similar dynamic increase in first-crack stress. Note that the difference among the average values of first crack stress is within the standard deviation and no definite conclusions on the influencing factors could be traced so far. However, it seems that the dynamic tensile strength of the Na-based GP matrix plays a dominant role in this respect, while the influence of the fibers is secondary.

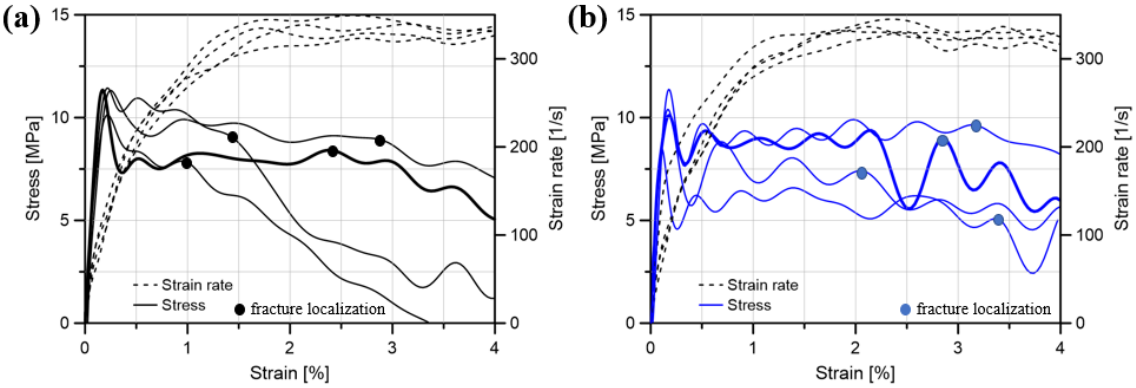

Figure 5.9 – Dynamic tensile curves for NaGP reinforced with: (a) PVA and (b) PE fibers. The filled circles indicate fracture localization as derived from the DIC images, while the thick curves correspond to the DIC images in Figure 10.

Table 5.4 – Dynamic tensile properties of plain GP and SHGC reinforced with PVA and PE fibers. Average values with standard deviations given in parentheses.

Composite	NaGP	$SHGC_{PVA}$	$SHGC_{PE}$
First crack stress [MPa]	11.2 (1.0)	11.1 (0.6)	10.1 (1.2)
DIF of first crack stress	6.5	3.8	3.5
Peak crack bridging stress [MPa]	-	9.3 (1.8)	8.8 (1.3)
DIF of peak crack bridging stress	-	2.3	1.9
Strain at fracture localization [%]	-	1.8 (0.2)	2.6 (0.4)
DIF strain at fracture localization		0.7	0.7
Work-to-fracture (up to softening) [kJ/m^3]	-	160.6 (28.2)	220.8 (21.7)
DIF of work-to-fracture (up to softening)	-	1.8	1.5

After the initial stress peak at first crack formation, $SHGC_{PVA}$ yielded the peak crack bridging stress at 1.1 % strain, while the subsequent deformation occured under gradually reducing stress levels. On the other hand, $SHGC_{PE}$ exhibited a maximum stress at 1.7 % strain. PVA fiber-reinforced GP showed an average peak crack-bridging stress of 9.3 MPa, while $SHGC_{PE}$ reached 8.8 MPa. The peak strain rates for both composites varied between 300 s^{-1} and 330 s^{-1}. Upon reaching a strain of approximately 1.5 %, the structural inertia is negligible, as there is no acceleration applied to the sample; see strain rate curves in Figure 5.9. Furthermore, the multiple cracking causes additional wave reflections and reduces the effective strain rate in the non-cracked regions. The first effect causes the pronounced stress oscillations in the curves, while the second one explains the subsequent multiple cracking occurring under reducing load. However, note that also under quasi-static loading the composites do not show a constant strain-hardening, with failure localization occurring considerably later after the peak stresses in a considerable number of specimens.

Because of the unsteady pattern of the stress-strain curves, the moments of fracture localization in the specimens were derived from the high-speed video recordings and indicated with filled circles on the curves in Figure 5.9. $SHGC_{PVA}$ yielded an average strain capacity of 1.8 %, while the average dynamic strain capacity of $SHGC_{PE}$ was 2.6 %. In both cases these values are lower than the corresponding strain at failure localization under quasi-static loading, with resulting DIFs of 0.7 for both materials. Partly this can be traced back to the lower crack widths, since both under quasi-static and impact loading the number of formed cracks were similar. Figure 5.10 shows representative crack patterns for both composites tested dynamically at distinct loading stages: I – before first crack formation; II – initiation of multiple cracking; III – failure localization. The corresponding stress-strain curves are indicated with thicker lines in Figure 5.9.

The composite reinforced with PE fiber yielded a denser crack pattern, as it can be judged by the extent of the damaged area. Note that the DIC evaluations in Figure 5.10 were not able to detect all the cracks distinctly due to the limited resolution of the high-speed cameras. However, in the case of $SHGC_{PVA}$, as the crack density was relatively low, the cracks could be observed more distinctly throughout the test. Therefore, the crack width measurements on $SHGC_{PE}$ specimens under impact loading were performed only in distinguishable cracks, in order to provide a reliable qualitative comparison. The evaluated crack openings showed larger values for GP reinforced with PVA fibers. After the first crack formation, $SHGC_{PVA}$ yielded a crack opening of 18 µm, while $SHGC_{PE}$ showed a crack opening of 14 µm. Prior to failure localization, $SHGC_{PVA}$ showed average crack openings of 64 µm (at 1.8 %

of strain), while SHGC_{PE} yielded an average crack width of 35 mm (at 2.6 % of strain). Although the cracks in SHGC_{PE} were narrower than in SHGC_{PVA}, the higher crack density ensured a superior strain capacity under dynamic loading.

(a) SHGC_{PVA}

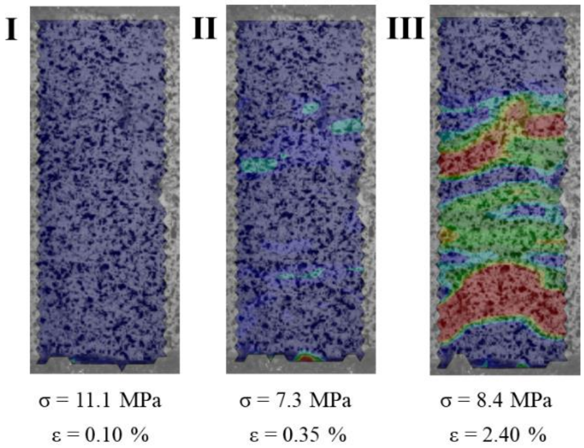

(b) SHGC_{PE}

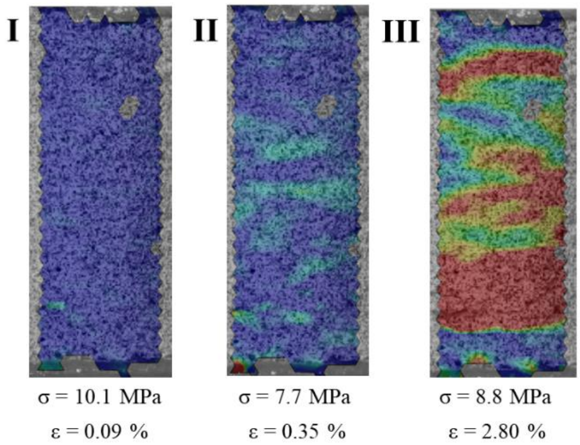

Figure 5.10 – Representative DIC results obtained in dynamic tests on NaGP reinforced with: (a) PVA and (b) PE fibers. Images show crack patterns at distinct stages: I – prior to first crack formation; II – initiation of multiple cracking; III – failure localization.

For both composites, the work-to-fracture increased under impact loading, which can be attributed to the dynamic increase of the peak crack bridging strength. This will be also demonstrated based on single-fiber pullout tests in Section 3.4. The average values for work-to-fracture are 160.6 kJ/m³ for SHGC_{PVA} and 220.8 kJ/m³ for SHGC_{PE}, respectively. The resulting DIFs are 1.8 and 1.5.

5.3.3. Microscopic analysis of the fracture surfaces

Figure 5.11 presents the failure modes of the tested specimens based on the optical analysis of the fracture surfaces with digital microscopy. SHGC_{PVA} shows a considerable degree of fiber rupture under quasi-static loading (Figure 5.11a), while under impact loading considerably more pronounced fiber pullout can be observed; see Figure 5.11b. The significant fiber rupture of the quasi-statically loaded SHGC_{PVA} specimens compared to SHGC_{PE} also explains the difference in the softening regimes of stress-strain curves in Figure 5.7. At the same time, the predominant fiber pullout exhibited by the fracture surfaces of SHGC_{PVA} under impact loading (Figure 5.11b) is in agreement with the measured reponse of the correponding specimens, showing extensive deformations under reducing stress levels. This change in failure mode was also observed on normal-strength PVA-SHCC in previous studies [36,37,38], and it was attributed to the unbalanced rate-dependent enhacement of the Young’s modulus and tensile strength of the PVA fibers [39].

Figures 5.11c,d present the failure modes corresponding to SHGC_{PE}. The predominance of the fiber pullout can be observed for both loading cases with distinguishable micro-spalling of the matrix, indicating no significant change in failure mode. Matrix micro-spalling can be attributed to the smaller diameter, smaller fiber spacing and higher tensile strength of the PE fibers.

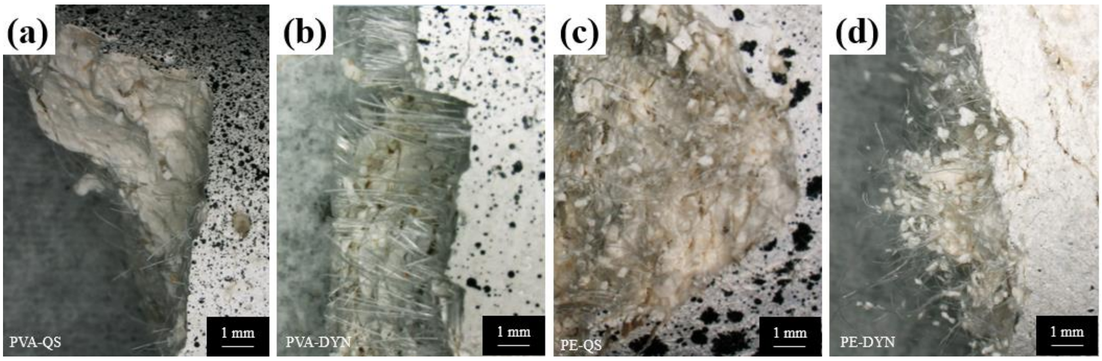

Figure 5.11 – Failure modes of SHGC_{PVA} under (a) quasi-static and (b) impact loading, and SHGC_{PE} under (c) quasi-static and (d) impact loading.

Also the ESEM images in Figure 5.12 demonstrate the matrix micro-spalling in SHGC_{PE}. Moreover, the ESEM images show no significant damage to the surfaces of the PVA fibers disregarding the loading regime. Compared to the PE fibers, more matrix residual are found on the PVA fiber surfaces, indicating a better chemical compatibilty with the GP matrix due to their hydrophilic character. Instead, PE fibers show slightly more pronounced damage in the case of the samples tested under impact, this being in agreement with previous studies on normal-strength PE-SHCC [37].

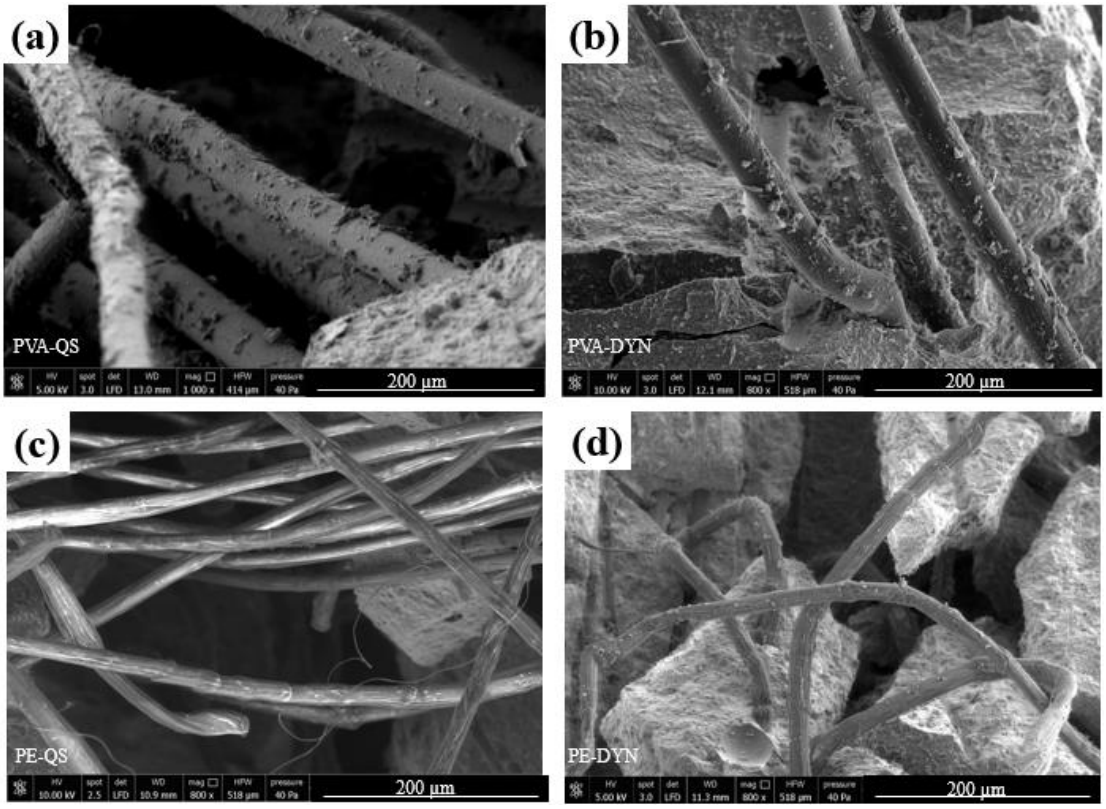

Figure 5.12 – ESEM images of the fracture surfaces of specimens reinforced with PVA fibers under (a) quasi-static and (b) impact loading, and PE fibers under (c) quasi-static and (d) impact loading.

5.3.4. Quasi-static and dynamic pullout tests

Figure 5.13 shows the pullout responses of both types of investigated fibers under two loading rates. Note that as a result of high scattering in single-fiber pullout experiments, only a limited number of representative samples are presented. In these diagrams, the force-slip curves for fibers at high pullout rates are only presented up to 0.5 mm, which is the displacement generated by one wave passage in the miniature split Hopkinson tension bar (see Section 2.2.6). The pullout results are summarized in Table 5.5.

Under quasi-static pullout, the PVA fibers yielded an average bond strength of 0.94 MPa, slightly higher compared to that of PE fibers (0.81 MPa). The bond strength is defined as the peak force over the embedded surface. As opposed to their pullout behavior out of cementitious matrices, the PVA fibers do not yield a slip-hardening behavior out of the NaGP matrix and the bond strength is considerably lower [36]. The curves are thus in agreement with the ESEM images of fracture surfaces of SHGP$_{PVA}$, which show no pronounced surface damage on the fibers.

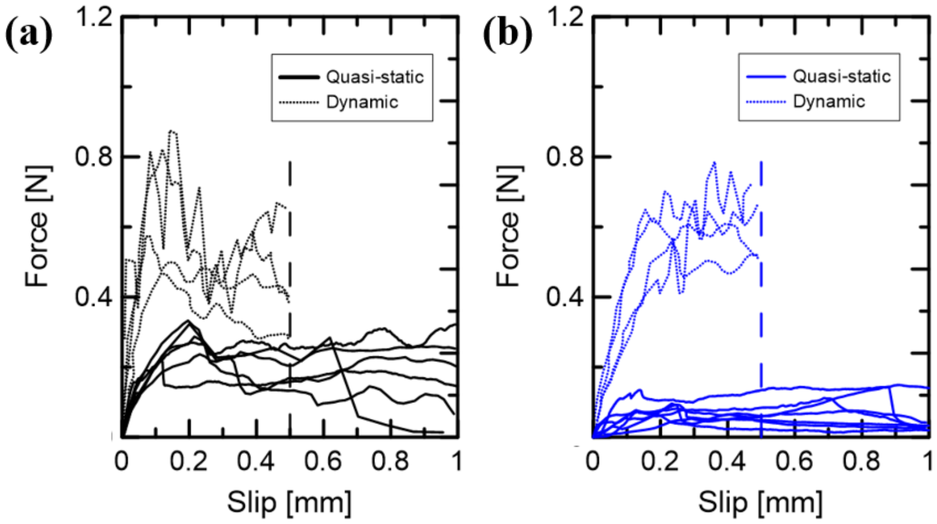

Figure 5.13 – Results of quasi-static and dynamic pullout tests with (a) PVA fiber and (b) PE fiber.

Table 5.5 – Results of quasi-static and dynamic single-fiber pullout tests. Average values with standard deviations given in parentheses.

Fiber type	PVA	PE
Quasi-static peak force [N]	0.23 (0.06)	0.10 (0.03)
Dynamic peak force [N]	0.46 (0.07)	0.59 (0.05)
Quasi-static bond strength [MPa]	0.94 (0.22)	0.81 (0.14)
Dynamic bond strength [MPa]	1.79 (0.28)	4.72 (0.40)
DIF bond strength	1.90	5.82
Quasi-static specific pullout energy [N/mm]	0.07 (0.01)	0.07 (0.01)
Dynamic specific pullout energy [N/mm]	0.15 (0.03)	0.29 (0.05)
DIF of specific pullout energy	2.14	4.14

Under dynamic loading, both PVA and PE showed enhanced bond strength with average values of 1.79 MPa and 4.72 MPa, respectively. This explains also the strong dynamic enhancement of the tensile strength of both composites under impact loading. The specific pullout energy was calculated up to 0.5 mm of slip as the area under the force-slip curves (N·mm) and normalized by the initial embedment area (2πrL). In the quasi-static regime, both PVA and PE fibers yielded a specific pullout energy of 0.07 N/mm on average; see Table 5. Under dynamic loading, an evident increase was observed for both fibers, showing enhanced values in the range of 0.29 N/mm for PE and 0.15 N/mm for PVA. By taking into account the smaller diameter and the higher collective embedment surface of the PE fibers, $\mathrm{SHGC_{PE}}$ could be expected to yield considerably higher tensile strength under impact loading compared to $\mathrm{SHGC_{PVA}}$, as opposed to the results reported in Section 3.2. A possible factor limiting the impact tensile strength (peak crack bridging stress) of $\mathrm{SHGC_{PE}}$ could be the dynamic tensile strength of the PE fibers. However, this will be a matter of interest in upcoming investigations.

5.3.5. Comparison between SHGC and normal-strength SHCC

In a previous study by the authors, normal-strength SHCC made with PVA and PE fibers were tested under tensile impact in a pre-tensioned SHTB [37]. The impact experiments were performed on identical specimen geometries at peak strain rates of 200 s^{-1} [37]. Under impact loading, the PVA-SHCC showed a strain-softening behavior with a pronounced stress drop after initial crack formation, and with a dynamic failure mode marked by complete fiber pullout. Furthermore, compared to the $\mathrm{SHGC_{PVA}}$ in this study, the PVA-SHCC yielded considerably lower tensile strength (i.e. peak crack bridging stress) and work-to-fracture. At the same time, the normal-strength PE-SHCC yielded a considerable rate-dependent enhancement of strain capacity and work-to-fracture, while the fracture mode was balanced in terms of fiber pullout and rupture under both loading regimes.

Based on the previous study [37] and on the results presented in Section 3.2 in the article at hand, it can be concluded the PE fiber is more suitable for impact resistant composites, both cement- and GP-based. For highlighting the main differences between the mechanical performance of $\mathrm{SHGC_{PE}}$ and PE-SHCC under impact loading, a direct comparison of these two composites and their plain constitutive matrices was performed in this study. The mechanical tests were performed in the testing configuration presented in Section 2.2.2.

Both types of plain matrices show similar tensile strength under impact loading; see Figure 5.14a. However, in the case of the geopolymer matrix, tensile strength is reached at a considerably higher strain as a result of its lower stiffness. Also, in the case of fiber-reinforced composites, the initial stress peaks are similar for both matrix types. However, after the initial peaks (first crack formation), SHCC yields a more abrupt stress drop. One reason for this can be the higher Young's modulus of the cementitious matrix and the greater difference between matrix stiffness and the crack-bridging stiffness in SHCC [13]. In the case of the geopolymer composites, the similar matrix stiffness and crack-bridging stiffness, seen as structural stiffnesses, result in lower specimen relaxation at crack formation and, consequently, in a less pronounced stress drop.

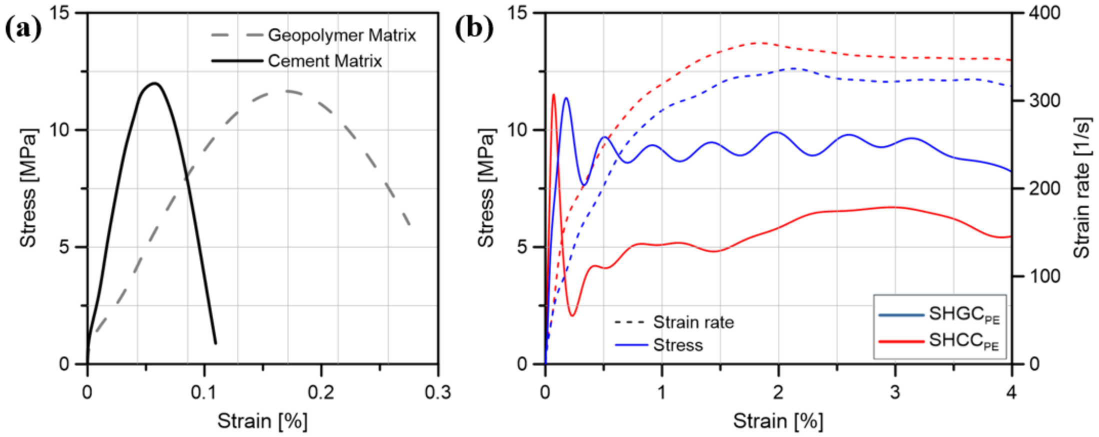

Figure 5.14 – Tensile stress-strain curves of (a) plain cementitious and GP-based matrices and (b) PE-SHCC and SHGC$_{PE}$ under impact tensile loading in the SHTB.

After the initial stress drop, the multiple cracking in SHCC starts into the hardening regime and continues up to a stress level of 6.8 MPa, which is considerably lower than the stress level recorded in the case of SHGC$_{PE}$ of approximately 10 MPa. This could be traced back to a possibly higher dynamic crack-bridging capacity of the PE fibers in the GP matrix. However, because the tensile strength of these composites is not only determined by the fiber-matrix bond strengh, but also by fiber distribution and flaw content, further investigations are needed to confirm this assumption.

5.4. Conclusions

Strain-hardening geopolymer composites (SHGC) were investigated under uniaxial tensile loading in the quasi-static regime as well as under impact loading using a gravity-driven split Hopkinson tension bar. The impact testing setup enabled displacement rates of 7.5 m/s with equivalent peak strain rates of up to 330 s^{-1}. The quantitative assessment of the material response was accompanied by microscopic analysis of the fracture surfaces. The fiber-matrix interaction depending on fiber type was analyzed in single-fiber pullout experiments quasi-statically and under displacement rates of up to 1 m/s. The dynamic pullout tests were performed in a miniature split Hopkinson bar.

Under quasi-static loading, the $SHGC_{PE}$ composites yielded superior tensile strength of 4.7 MPa and strain capacity of 3.6 % in comparison to $SHGC_{PVA}$ with corresponding values of 4.1 MPa and 2.5 %, respectively. Moreover, the work-to-fracture exhibited by the GP composites reinforced with PE fibers was 73% higher in comparison to the composite made of PVA. This is as a consequence of more pronounced multiple cracking in $SHGC_{PE}$ in the first place.

Under dynamic tensile loading, both GP-based composites showed an improvement in all mechanical parameters, except strain capacity, in comparison to the values obtained in the quasi-static experiments. In contrast to $SHGC_{PE}$, $SHGC_{PVA}$ did not yield strain-hardening behavior despite the formation of multiple cracks. Furthermore, $SHGC_{PVA}$ showed a change in failure mode from pronounced fiber rupture under quasi-static loading to pronounced fiber pullout under impact loading; this peculiar phenomenon being similar to that observed for PVA-SHCC. $SHGC_{PE}$ yielded superior mechanical performance and higher deformations as well as 35 % higher work-to-fracture. The fracture surfaces of the $SHGC_{PE}$ specimens showed no significant difference in failure mode depending on loading regime.

In quasi-static single-fiber pullout experiments, PVA fibers yielded 16 % higher bond strength compared to PE fibers, while the specific pullout energy was 0.07 N/mm in both cases. However, under dynamic loading, PE fibers showed superior crack bridging properties compared to PVA: 4.26 MPa vs. 1.79 MPa for bond strength, and 0.29 N/mm vs. 0.15 N/mm for specific pullout energy. This partly clarified the superior quasi-ductility and energy dissipation of $SHGC_{PE}$ under impact loading but could not explain the slightly lower impact tensile strength of the composite compared to $SHGC_{PVA}$.

Given the superior behavior of $SHGC_{PE}$ under impact loading compared to $SHGC_{PVA}$ and the similar findings on equivalent SHCC from previous studies, a direct comparison between $SHGC_{PE}$ and PE-SHCC was performed under tensile impact loading. In contrast to normal-strength PE-SHCC, $SHGC_{PE}$ did not yield a pronounced stress drop after the formation of the first crack in impact experiments, and the subsequent multiple cracking occurred at a considerably higher stress level. This was partly traced back to lower Young's modulus of the GP matrix and a balanced relationship between the matrix stiffness and crack-bridging action.

While the properties of Na-based $SHGC_{PE}$ are highly promising for structural strengthening against dynamic actions, further studies should be performed to clarify the relationship between the micromechanical parameters and the composite behavior. Also, the effect of GP matrix composition on the performance of GP composites at high strain rates will be a matter of future investigations by the authors.

5.5. References

[1] Guruswami, R., & Subhash, G. 1994. Critical Appraisal of Limiting Strain Rates for Compression Testing of Ceramics in a Split Hopkinson Pressure Bar. Journal of the American Ceramic Society 77: 263–267

[2] Deshpande, A. A., Kumar, D., Mourougassamy, A., & Ranade, R. 2017. Development of a Steel-PVA Hybrid Fiber SHCC. In International Conference on Strain-Hardening Cement-Based Composites (pp. 195-202). Springer, Dordrecht.

[3] Paul, S. C., & van Zijl, G.P.A.G. 2013. Mechanically induced cracking behaviour in fine and coarse sand strain hardening cement based composites (SHCC) at different load levels. Journal of Advanced Concrete Technology 11: 301-311.

[4] Mechtcherine, V., de Andrade Silva, F., Müller, S., Jun, P., & Toledo Filho, R.D. 2012. Coupled strain rate and temperature effects on the tensile behavior of strain-hardening cement-based composites (SHCC) with PVA fibers. Cement and Concrete Research 42(11): 1417-1427.

[5] Yun, H.D., Kim, S.W., Lee, Y.O., & Rokugo, K. 2011. Tensile behavior of synthetic fiber-reinforced strain-hardening cement-based composite (SHCC) after freezing and thawing exposure. Cold Regions Science and Technology 67: 49-57.

[6] Curosu, I., Mechtcherine, V., Forni, D., & Cadoni, E. 2017. Performance of various strain-hardening cement-based composites (SHCC) subject to uniaxial impact tensile loading. Cement and Concrete Research 102: 16-28.

[7] Mechtcherine, V. 2013. Novel cement-based composites for the strengthening and repair of concrete structures. Construction and building materials 41: 365-373.

[8] de Andrade Silva, F., Butler, M., Mechtcherine, V., Zhu, D., & Mobasher, B. 2011. Strain rate effect on the tensile behaviour of textile-reinforced concrete under static and dynamic loading. Materials Science and Engineering: A 528: 1727-1734.

[9] Curosu, I., Mechtcherine, V., Millon, O. 2016. Effect of fiber properties and matrix composition on the tensile behavior of strain-hardening cement-based composites (SHCC) subject to impact loading. Cement and Concrete Research 82: 23-35.

[10] Curosu, I., Mechtcherine, V., Hering, M., Curbach, M. (2019). Mineral-bonded composites for enhanced sructural impact safety – overview of the format, goals and achievements of the Research Training Group GRK 2250. In Pijaudier-Cabot et al. (eds.) 10th International Conference on Fracture Mechanics of Concrete and Concrete Structures FraMCoS-X, 23-26 June, 2019, Bayonne, France.

[11] Li, V.C. (2003). On engineered cementitious composites (ECC). Journal of advanced concrete technology 1(3): 215-230.

[12] Curosu, I. (2017). Influence of fiber type and matrix composition on the tensile behavior of strain-hardening cement-based composites (SHCC) under impact loading. Dissertation TU-Dresden, 2017.

[13] Heravi, A. A., Curosu, I., &Mechtcherine, V. (2020). A gravity-driven split Hopkinson tension bar for investigating quasi-ductile and strain-hardening cement-based composites under tensile impact loading. Cement and Concrete Composites 105: 103430.

[14] Li, V.C. (2019). Sustainability of Engineered Cementitious Composites (ECC) Infrastructure. Engineered Cementitious Composites (ECC). Springer, Berlin, Heidelberg: 261-312.

[15] Schneider, M., Romer, M., Tschudin, M., & Bolio, H. (2011). Sustainable cement production—present and future. Cement and concrete research 41(7): 642-650.

[16] Davidovits, J. (1991). Geopolymers: inorganic polymeric new materials. Journal of Thermal Analysis and calorimetry 37(8): 1633-1656.

[17] Temuujin, J., Rickard, W., Lee, M., & van Riessen, A. (2011). Preparation and thermal properties of fire resistant metakaolin-based geopolymer-type coatings. Journal of non-crystalline solids 357(5): 1399-1404.

[18] Musil, S. S., & Kriven, W. M. (2014). In situ mechanical properties of chamotte particulate reinforced, potassium geopolymer. Journal of the American Ceramic Society 97(3): 907-915.

[19] Alcamand, H. A., Borges, P. H., Silva, F. A., & Trindade, A. C. C. (2018). The effect of matrix composition and calcium content on the sulfate durability of metakaolin and metakaolin/slag alkali-activated mortars. Ceramics International, 44(5), 5037-5044.

[20] Nematollahi, B., Sanjayan, J., & Shaikh, F.U.A. (2016). Matrix design of strain hardening fiber reinforced engineered geopolymer composite. Composites Part B: Engineering 89: 253-265.

[21] de Andrade Silva, F., Borges, P.H.R., & Trindade, A.C.C. (2019). Evaluation of Fiber–Matrix Bond in the Mechanical Behavior of Geopolymer Composites Reinforced with Natural Fibers. Advances in Civil Engineering Materials 8(3): 361-375.

[22] Khan, M. Z. N., Hao, Y., Hao, H., & Shaikh, F. U. A. (2018). Experimental evaluation of quasi-static and dynamic compressive properties of ambient-cured high-strength plain and fiber reinforced geopolymer composites. Construction and Building Materials 166: 482-499

[23] Menna, C., Asprone, D., Forni, D., Roviello, G., Ricciotti, L., Ferone, C., & Cadoni, E. (2015). Tensile behaviour of geopolymer-based materials under medium and high strain rates. In EPJ Web of Conferences 94: 01034. EDP Sciences.

[24] Khan, M. Z. N., Hao, Y., & Hao, H. (2019). Mechanical properties and behaviour of high-strength plain and hybrid-fiber reinforced geopolymer composites under dynamic splitting tension. Cement and Concrete Composites: 103343.

[25] Kriven, W. M., Bell, J. L., & Gordon, M. (2003). Microstructure and microchemistry of fully-reacted geopolymers and geopolymer matrix composites. Ceramic Transactions 153:1994.

[26] Heravi, A., & Mechtcherine, V. Mechanical characterization of strain-hardening cement-based composite (SHCC) under dynamic tensile load. 10th International Conference on Fracture Mechanics of Concrete and Concrete Structures, FraMCoS-X, 23-26 June, 2019, Bayonne, France.

[27] Chen, W. W., & Song, B. (2011). Split Hopkinson bar design, testing and applications. Mechanical engineering series, Springer, London, 11-80.

[28] Kolsky, Herbert. (1949). An investigation of the mechanical properties of materials at very high rates of loading. Proceedings of the physical society B62 (11): 676.

[29] Cheng, M., Chen, W., & Weerasooriya, T. (2005). Mechanical properties of Kevlar® KM2 single fiber. Journal of Engineering Materials and Technology 127(2): 197-203.

[30] Sanborn, B., & Weerasooriya, T. (2014). Quantifying damage at multiple loading rates to Kevlar KM2 fibers due to weaving, finishing, and pre-twist. International Journal of Impact Engineering 71: 50-59.

[31] Trindade, A.C.C., Curosu, I., Liebscher, M., Mechtcherine, Silva, F.A. (2020). On the mechanical performance of K-and Na-based strain-hardening geopolymer composites (SHGC) reinforced with PVA fibers. Construction and Building Materials 248: 118558.

[32] Curosu, I., Liebscher, M., Mechtcherine, V., Bellmann, C., & Michel, S.(2017). Tensile behavior of high-strength strain-hardening cement-based composites (HS-SHCC) made with high-performance polyethylene, aramid and PBO fibers. Cement and Concrete Research 98: 71-81.

[33] Reinhardt, H. W., & Weerheijm, J. (1991). Tensile fracture of concrete at high loading rates taking account of inertia and crack velocity effects. International Journal of Fracture 51(1): 31-42.

[34] Lee, S., Kim, K.-M., Park, J., Cho, J.-Y. (2018). Pure rate effect on the concrete compressive strength in the split Hopkinson pressure bar test, International Journal of Impact Engineering 113: 191–202.

[35] Ozbolt, J., Sharma, A., Irhan, B., Sola, E. (2014). Tensile behavior of concrete under high loading rates, International Journal Impact Engineering 69: 55–68.

[36] Mechtcherine, V., Millon, O., Butler, M., & Thoma, K. (2011). Mechanical behaviour of strain hardening cement-based composites under impact loading. Cement and Concrete Composites, 33(1): 1-11.

[37] Curosu, I., Mechtcherine, V., Forni, D., Cadoni, E. (2017). Performance of various strain-hardening cement-based composites (SHCC) subject to uniaxial impact tensile loading. Cement and Concrete Research, 102: 16-28.

[38] Mechtcherine, V., de Andrade Silva, F., Butler, M., Zhu, D., Mobasher, B., Gao, S. L., & Mäder, E. (2011). Behaviour of strain-hardening cement-based composites under high strain rates. Journal of Advanced Concrete Technology, 9(1): 51-62.

[39] Curosu, I., Mechtcherine, V., Millon, O. (2016). Effect of fiber properties and matrix composition on the tensile behavior of strain-hardening cement-based composites (SHCCs) subject to impact loading. Cement and Concrete Research 82: 23-35.

6 Influence of elevated temperatures on the residual and quasi in-situ flexural strength of strain-hardening geopolymer composites (SHGC) reinforced with PVA and PE fibers

6.1. Introduction

Geopolymers (GP) can be described as aluminosilicate binders [1], formed in high pH-based solutions with alkali ions [2]. This material class is a product of the geochemistry that yields the synthesis of metastable zeolites [3,4]. The mineral binders react to nano-porous, impervious products which are capable of withstanding high temperatures and extremely aggressive chemical attacks [2,4,5]. GP show suitable performances when produced with distinct aluminosilicate sources, such as fly ash [6] and metakaolin [6,7], and distinct alkali solutions, such as sodium [7,8] and potassium [8,9]. When compared to traditional cement-based materials, GP demonstrate a faster curing under temperature treatment [2], lower density [5], lower modulus of elasticity [10], and equivalent mechanical response in terms of strength [5,10]. Note that cement production is held responsible for at least 8% of total CO_2 release in the atmosphere [11]. Hardened GP are also inherently fire-resistant [1,4], presenting enhanced thermal stability when compared to materials made of traditional binders [3].

Duxson *et al.* [12,13] studied the thermal behavior of metakaolin-based materials. GPs produced with Si/Al ratios higher than 1.65 demonstrated an increase in densification for various heating rates due to the strengthening of Al-O bonds in the presence of K-based solutions [12]. In contrast, for the Na-based compositions lower densification temperatures were observed, which can be justified by their more pronounced viscous flow, leading to higher extents of thermal dilation [13,14]. A similar trend was found when using fly ash as raw material [15]. Zhao and Sanjayan [16] performed a rapid surface and standard curve fire tests on GP concrete and Portland cement concrete (PCC). Higher sorption, characterized by a higher number of connected pores, was found for GP when compared to PCC at similar strength levels, suggesting an easier vapor escape from the GP, resulting in higher spalling resistance. Therefore, applications as fireproof doors and firewalls [17], fire protection of concrete tunnel linings [18], and coatings as thermal barriers [19] have been widely considered for the use of the GP technology. However, there is still a lack of understanding related to (i) shrinkage deformations due to water loss [20,21]; (ii) damage resulting from sudden temperature changes (thermal shock), e.g. loss in stiffness [22]; and (iii) efficiency of fiber addition for enhanced deformability also at elevated temperatures [10].

Similar to cementitious materials, plain GP yield high brittleness/low deformation capacity [10]. A widely used solution to increase their ductility and energy absorption is the incorporation of appropriate reinforcement. Particulate [9,14,20], steel [23], and textile reinforcements [10,24] have already been used in thermal applications. Trindade *et al.* [10] and Lyon *et al.* [24] demonstrated thermal resistance of MK-based GP with jute textile up to 250 ºC, and carbon and glass fabrics up to 200 ºC and 800 ºC, respectively.

Enhancements in strength, ductility, crack control, and energy absorption in normal environmental conditions can be found in the literature with the incorporation of short polymer micro-fibers, resulting in strain-hardening geopolymer composites (SHGC) [25,26]. This technology presents several advantages when compared to textile reinforcements, such as easy molding processes and lower fabrication costs [25,27]. It corresponds to a type of composite intended for repair applications, made of micro-fibers in volume contents of up to 2 %, resulting in a quasi-ductile and strain-hardening tensile behavior through the formation of multiple fine cracks up to failure localization, i.e., softening [28,29]. By ensuring load bearing capacity at elevated temperatures, the SHGC technology could be successfully used as reinforcement layer in specific elements of: (i) structures exposed to hot arid regions with temperatures in structural elements rising to 80 ºC [30,31]; (ii) early-stage fire occurrences [32,33]; (iii) safe plugging and permanent abandonment (P&A) in oil wells (up to 200 ºC in 3000 m depth ranges) [34,35]; and others.

Given the lack of published reports on SHGC under elevated temperatures, some predictions can be made based on the available knowledge on strain-hardening cementitious composites (SHCC). Reduction in stiffness and strength were found by Magalhães *et al.* [36] when pre- heating polyvinyl alcohol (PVA) based-SHCC. Despite presenting a typical strain-hardening behavior up to 145 ºC, at 190 ºC the composites demonstrated a great reduction in mechanical properties, with dramatic degradation and brittle response at 250 ºC. Mechtcherine *et al.* [37] performed in-situ and residual tensile tests with a similar SHCC up to 150 ºC, evidencing a strain-rate effect coupled with temperature exposure. In comparison with the results of the in-situ tests, the residual SHCC yielded higher tensile strengths, explained by the reduction of the fiber-matrix bond strength at high temperatures. Curosu *et al.* [38] evaluated the influence of fiber type on the in-situ and residual mechanical behavior of high-strength SHCC up to 200 ºC. The use of Aramid and PBO fibers yielded a pronounced degradation in strength and ductility at 105 °C, when compared to the composites containing ultra-high molecular weight polyethylene (UHMWPE) fiber. At 200 °C, all composites (except Aramid) exhibited no multiple cracking and brittle failure. Zhang *et al.* [39] observed an improved PVA-SHCC performance up to 200 ºC by using high fly ash contents in the matrix mix design, maintaining similar cracking and ductility levels compared to the non-heated specimens. Furthermore, Liu *et al.* [40] showed potential applications for this type of matrix in reducing the risk of spalling under fire, since such pozzolanic modification was found capable of increasing the permeability of the SHCC before reaching the matrix melting point. Liu and Tan [41] also found a promising behavior through the partial replacement of PVA by steel fibers. All the previous studies demonstrated the fragility of SHCC under elevated temperatures, presenting room for improvements, such as those by matrix modification.

Therefore, this paper presents an extensive investigation on the influence of elevated temperatures (100 °C and 200 °C) on the mechanical and morphological properties of different types of metakaolin-based SHGC. This temperature range was chosen established per the thermal capacity of the fibers used in the manufacture of SHGC (PVA and PE), with melting points ranging from 150 ºC - 240 ºC, allowing a comparison with typical SHCC responses. Varied formulations (Na- and K-based) and fibers (PVA and PE) were investigated, aiming at defining suitable fiber-matrix combinations. Thermogravimetry and dilatometry results were used to analyze the material behavior. Flexural tests were performed in distinct temperatureregimes (residual and quasi in-situ), with all composites variations before and after temperature exposure. Mercury intrusion porosimetry (MIP), and environmental scannning electron microscopy (ESEM) techniques were used to investigate morphological and microstructural features.

6.2. Experimental program

6.2.1. Materials and composite manufacturing

Both geopolymer (GP) mixtures manufactured in this study were produced through the combination of metakaolin (MK), as the main aluminosilicate source, with an alkali-based solution (sodium or potassium-based) representing the following formulation: $X_2O \cdot Al_2O_3 \cdot 4SiO_2 \cdot 11H_2O$; where X may be replaced by Na or K elements.

Table 6.1 – Geometric and mechanical properties of the fibers.

Fiber type	PVA [37]	UHMWPE [38]
Producer	Kuraray (Japan)	DSM (the Netherlands)
Brand	Kuralon® K-II REC15	Dyneema® SK62
Length [mm]	12	12
Nominal diameter [µm]	40	20
Density [g/cm^3]	1.26	0.97
Tensile strength [MPa]	1600	2500
Young's modulus [GPa]	40	80
Elongation at break [%]	7	3.5
Coef. of thermal exp. [10−6 1/°C]	-1	-12
Melting point [ºC]	240 [30]	150 [38]

Both hydroxide components, obtained from Sigma-Aldrich® with purity higher than 90%, were combined with deionized water, followed by the addition of hydrophilic fumed silica CAB-O-SIL® M-5 from Cabot (Belgium). The solution was mixed for 24 h in a magnetic stirrer, resulting in the stable water-glass (WG) used in each GP formation. High reactivity Metamax® from BASF (Germany), was used as the aluminosilicate product, since it presents a high level of purity and small particle size, with an average diameter of 1.3 µm [26]. The density provided by the manufacturer is 2.6 g/cm^3. PVA and UHMWPE (short: PE) fibers were incorporated into both GP mixtures in volume contents of 2%. The geometric and mechanical properties of the fibers are presented in Table 6.1. Also, their melting points were indicated following the values presented in previous works [30,38]. A general overview of the material combinations (plain matrix and composites) is presented in Table 6.2.

Table 6.2 – Content of incorporated materials for all material variations (considering 1 kg of WG).

GP material	KGP	KGP$_{PVA}$	KGP$_{PE}$	NaGP	NaGP$_{PVA}$	NaGP$_{PE}$
WG/MK ratio	1.85			1.71		
WG [g]	1000.00			1000.00		
MK [g]	538.44			584.01		
PVA [g]		19.35	-		19.35	-
PE [g]	-	-	14.90	-	-	14.90

The composites were prepared in a 10-liter Hobart mixer as follows: (i) mixing of MK and WG in the amounts presented in Table 6.2 for 3 min with an intermediate speed of 198 rpm to guarantee an adequate particle dispersion and degree of geopolymerization [42]; (ii) incorporation of fibers (PVA or UHMWPE); (iii) mixing for 3 min with a higher speed of 365 rpm to ensure a proper fiber dispersion. The fresh GP mixtures were then cast into steel molds with a vibration step for consolidation and air voids removal. A semitransparent adhesive tape was used to cover and protect the steel parts, allowing and facilitating specimen extraction after 24 hours of curing [26]. The molds were sealed in plastic bags to prevent early dehydration, followed by the specimen’s removal and storage inside dry plastic bags for two weeks, following the recommendations presented in earlier studies [5,26]. Prisms with dimensions of 160 mm x 40 mm x 40 mm were produced for all material variations.

6.2.2. Testing configurations

6.2.2.1. Flexural tests

A servo-hydraulic universal testing system with a load capacity of 200 kN was used to perform the three-point flexural tests of all GP configurations. The tests were carried out based on the BS EN 196-1 [43], where three specimens were tested for each material variation under a load-controlled rate of 50 N/s. The span between supports was equal to 100 mm. The heating of the samples consisted of a gradual increase of 10 ºC/min upon reaching the desired elevated temperature of 100 ºC or 200 ºC, followed by 1 hour of heating in an electric furnace from Memmert GmbH + Co. KG (Germany).

The composites were tested after two distinct thermal regimes, and their results distinguished in quasi in-situ and residual responses. For the quasi in-situ regime, the specimens were tested immediately after the 1 h heating process. They were removed from the hot furnace and placed in the testing machine, undergoing a sudden temperature change in the process. Ten minutes were established as the maximum cooling interval for this group of specimens to be tested after extraction from the furnace. As opposed to this, for the residual regime, the specimens were subject to a gradual cooling inside the furnace to room temperature before mechanical testing.

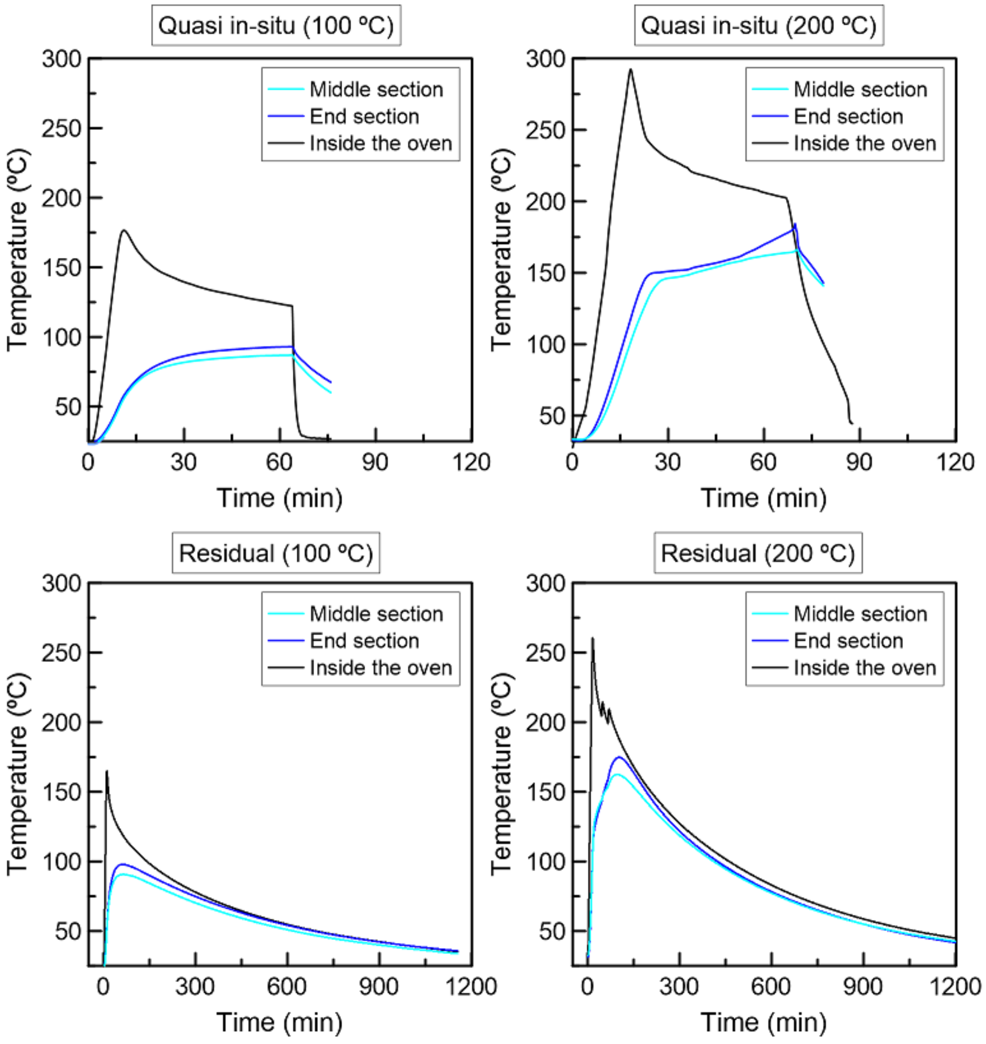

Figure 6.1 – Temperature variation inside the specimens and in the furnace for different heating and cooling regimes (note different horizontal axis limits).

Thermocouples inside selected specimens were used to monitor the internal temperature variation. For this, the specimens were drilled, and three thermocouples were positioned in distinct regions, two inside the specimen (middle and end sections), and one outside to monitor the temperature inside the furnace, verifying also the value presented by the controller. Representative temperature *vs.* time curves are shown in Figure 6.1 for both temperature treatments and cooling regimes. For all variations, the difference between both temperatures measured inside the specimens was not substantial. The one measured at the end section always presented slightly higher values than the one placed in the middle section, with a maximum difference of 8 ºC recorded for residual tested specimens at 200 ºC. Also, the maximum internal temperatures recorded for both heating temperatures were: 93 ºC and 97 ºC, and 174 ºC and 184 ºC, for quasi in-situ and residual tested specimens at 100 ºC and 200 ºC, respectively.

6.2.2.2. Mercury intrusion porosimetry (MIP)

Plain GP and SHGC samples were cut in cubes with 10 mm sides for porosity evaluations. All materials were analyzed at room temperature and after 100 ºC and 200 ºC exposures. The samples were immersed in isopropanol, followed by an Alpha 1-2 LDplus Christ (Germany) vacuum desiccator for 24 h. Finally, a Porotec Porosimeter PASCAL 140/440 (Germany) with a mercury surface tension of 0.48 N/m, a contact angle of 140º, and maximum testing pressure of 400 MPa was used to record the influence of temperature exposure on the porosity of the samples. The tests were performed at increasing rates of 6 to 19 MPa/min and decreasing rates of 28 to 7 MPa/min.

6.2.2.3. Thermogravimetric analysis (TGA)

TGA analyses were performed with a STA 409 DC thermal analyzer from Netzsch (Germany), which conducted simultaneous Differential Thermal Analysis (DTA). Both plain GP mixtures (NaGP and KGP) and fibers (PVA and UHMWPE) were tested. All samples were mill grounded, deposited on a Al_2O_3 crucible, and heated from 20 to 250 ºC at a heating rate of 10 ºC/min using 60 ml/min of nitrogen as environmental gas, for the matrix and fibers, respectively.

6.2.2.4. Dilatometry

To measure the thermal expansion and shrinkage behavior of the plain geopolymers exposed to elevated temperatures, a DIL 402 C dilatometer from Netzsch (Germany), equipped with a contact method and a Labview control system was used. Three cylindrical samples were prepared for each variation, with 8 mm in diameter and 20 mm in length. All measurements occurred according to ASTM E831 [44], in the temperature range of 20 to 500 ºC, with a heating rate of 10 ºC/min, and a nitrogen flow rate of 60 ml/min. A preload of 100 mN was applied to allow the adequacy of the instrument in data recording. Figure 6.2 presents the testing setup.

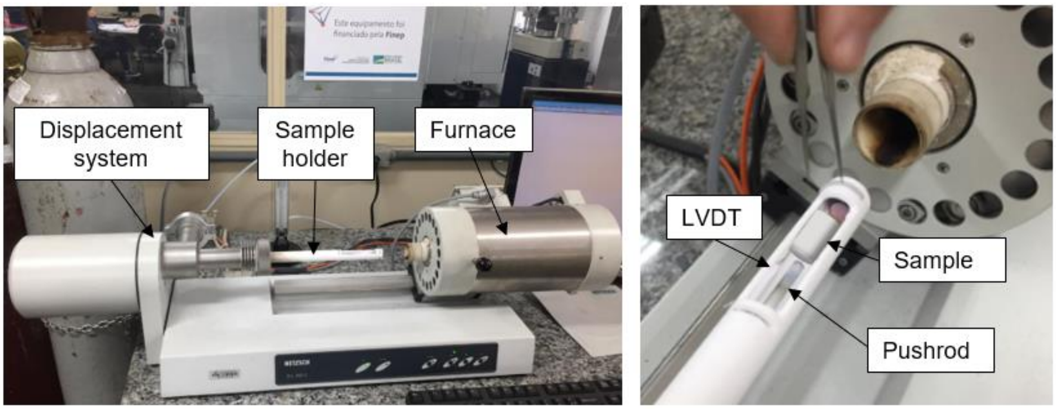

Figure 6.2 – Dilatometry testing setup.

6.2.2.5. Microscopy analysis

Microscopic analysis was conducted on an ESEM Quanta 250 FEG of FEI (the Netherlands) to evaluate the microstructure of the samples and to study the state of the fracture surfaces of the fibers after exposure to high temperatures.

6.3. Results and discussion

6.3.1. Mechanical testing

Initially, the flexural properties of both NaGP and KGP matrices were evaluated. Figure 6.3 shows the residual flexural strength comparison between these matrices after exposure to 100 ºC and 200 ºC, and their unheated references.

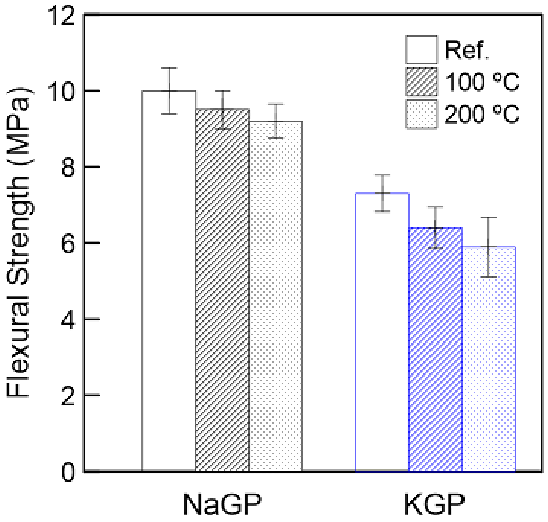

Figure 6.3 – Influence of temperature exposure on the residual flexural strength of NaGP and KGP.

NaGP materials showed higher flexural strength in all temperature variations, reaching average values of 9.8, 9.5 and 8.9 MPa, at room temperature, 100 ºC and 200 ºC, respectively. Opposed to that, KGP demonstrated slightly lower strength, reaching average values of 7.6, 6.4 and 5.9 MPa, at similar conditions. This may be associated to differences in reactivity of the GP matrices as well as damage caused by the sudden loss of water at elevated temperatures, further evidenced by the porosimetry (Section 3.2) and thermogravimetry analysis (Section 3.3).

Figure 6.4 and Table 6.3 present the flexural responses without temperature exposure of both NaGP and KGP reinforced with PVA and PE fibers. All composites presented first crack stresses similar to the flexural strength of the corresponding plain matrices, as shown in Figure 6.3, with slightly higher values of SHGC containing PE fiber. This phenomenon could be justified by an increased microcrack bridging due to a smaller fiber diameter compared to PVA, as discussed in a previous study [27]. $NaGP_{PVA}$ and KGP_{PVA} composites yielded an average flexural strength of 19.7 and 13.7 MPa, respectively. This remarkable response found for $NaGP_{PVA}$ can be attributed to: (i) an enhanced mechanical performance of the plain NaGP matrix, as evidenced in Figure 6.3; (ii) the limited fluidity of this matrix in fresh state, that enables a higher internal friction in the mixed materials and consequently a superior fiber dispersion, and (iii) an improved fiber-matrix interaction with controlled debonding and pullout [28].

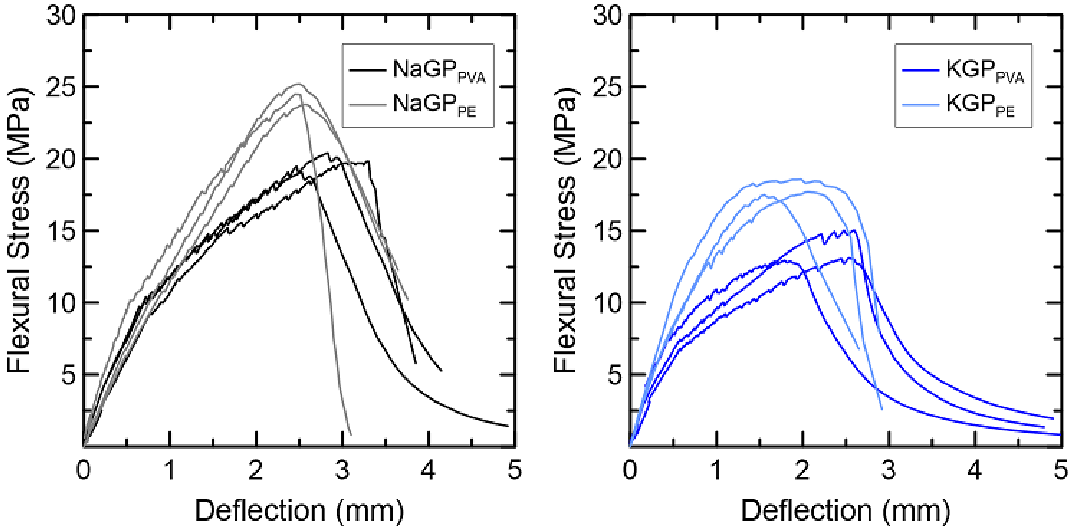

Figure 6.4 – Flexural behavior of NaGP and KGP reinforced with PVA and PE fibers at room temperature.

Table 6.3 – Results of flexural tests on NaGP and KGP reinforced with PVA and PE fibers at room temperature.

Composite	NaGP_{PVA}	NaGP_{PE}	KGP_{PVA}	KGP_{PE}
First-crack stress [MPa]	9.6 (0.3)	10.7 (0.6)	7.4 (0.4)	8.3 (0.2)
Flexural strength [MPa]	19.7 (0.7)	23.5 (0.7)	13.7 (1.4)	17.9 (0.4)
Displacement at peak load [mm]	2.6 (0.3)	2.5 (0.1)	2.4 (0.5)	1.9 (0.4)
Work-to-fracture [N/mm]	36.8 (3.2)	36.4 (1.6)	22.6 (2.8)	23.2 (3.4)
Number of cracks [un]	18 (2)	32 (4)	15 (2)	25 (3)

The incorporation of PE fibers in both NaGP and KGP matrices resulted in even higher flexural strengths, reaching average 23.5 MPa and 17.9 MPa, respectively. This enhancement occurs mostly due to increases in crack-bridging capacity, due to the superior physical and mechanical properties and lower diameter of the PE fiber (Table 6.1), when compared to PVA [45,46]. This statement is supported by the average number of cracks developed by the loaded specimens of each variation. The counting made with PVA-based composites resulted in 18 (NaGP) and 15 (KGP) cracks, while the same variations with PE showed 32 and 25 cracks, respectively. The average values of work-to-fracture, as calculated using the area under the stress-displacement curves up to peak load, are also presented in Table 6.3. The results demonstrate the superiority of NaGP in terms of mechanical behavior, reaching work-to-fracture of 36.8 N/mm and 36.4 N/mm when reinforced with PVA and PE fibers, respectively. In similar conditions, only 22.6 N/mm and 23.2 N/mm were derived for KGP. Once again, this is due to differences in dispersion, fiber, and fiber-matrix bond properties [45].

The residual and quasi in-situ NaGP flexural results are shown in Table 6.4 and Figure 6.5. The continuous curves represent the residual, while the dashed curves represent the quasi in-situ tested specimens. The gray curves were added for comparison purposes, representing the average reference responses at room temperature, as shown in Figure 6.3. Table 6.4 presents the average values found for first-crack stress, flexural strength, displacement at peak load, and work-to-fracture. It also presents a temperature reduction factor (k_d). This factor was obtained for each parameter by dividing the result found after temperature exposure by the same result as obtained at room temperature (Table 6.3).

Regarding first-crack stresses it is possible to observe a small decrease of all residual values with temperature increase, following the behavior presented by both matrices in Figure 6.3. Furthermore, the occurrence of strength reductions for all NaGP composites is noticeable, when exposed to 100 ºC, yielding maximum flexural strengths of 18.6 MPa and 18.8 MPa (residual), and 12.7 MPa and 18.2 MPa (quasi in-situ), for PVA and PE fiber, respectively. Except for the displacement at peak load, the quasi in-situ (QIS) tested specimens yielded stronger reductions in mechanical properties when compared to the residual (R) testing conditions. The increase in deformation at maximum strength results from the reduced stiffness of the matrix and larger crack widths.

The greater stress and stiffness losses (50% of the reference values) of the quasi in-situ tested specimens can be explained by (i) the elongation and shape modification of the fibers during the load application on hot specimens [46], since the mechanical behavior is more viscous at elevated temperatures [48], consequently affecting the fiber-matrix interface mechanisms [49]. A distinct behavior occurs for the residual tests since the gradual cooling to room temperature allows fibers to partly regain their stiffness [48]. This is more evident for PE reinforcements, with greater losses in stiffness, when compared to PVA, as later discussed in more detail in Section 3.3. The PE reduction in modulus and tenacity above 100 ºC was also shown by Liu and Yu [50]. It is also worth noticing that the quasi in-situ tested specimens suffered a more drastic temperature variation during the oven's removal process. The temperature on the surface dropped faster than that of the inner of the specimen, creating residual thermal stresses and non-uniform fiber performance throughout the cross-section [47], as shown by the color difference between the outermost and inner surfaces of the material in Figure 6.6.

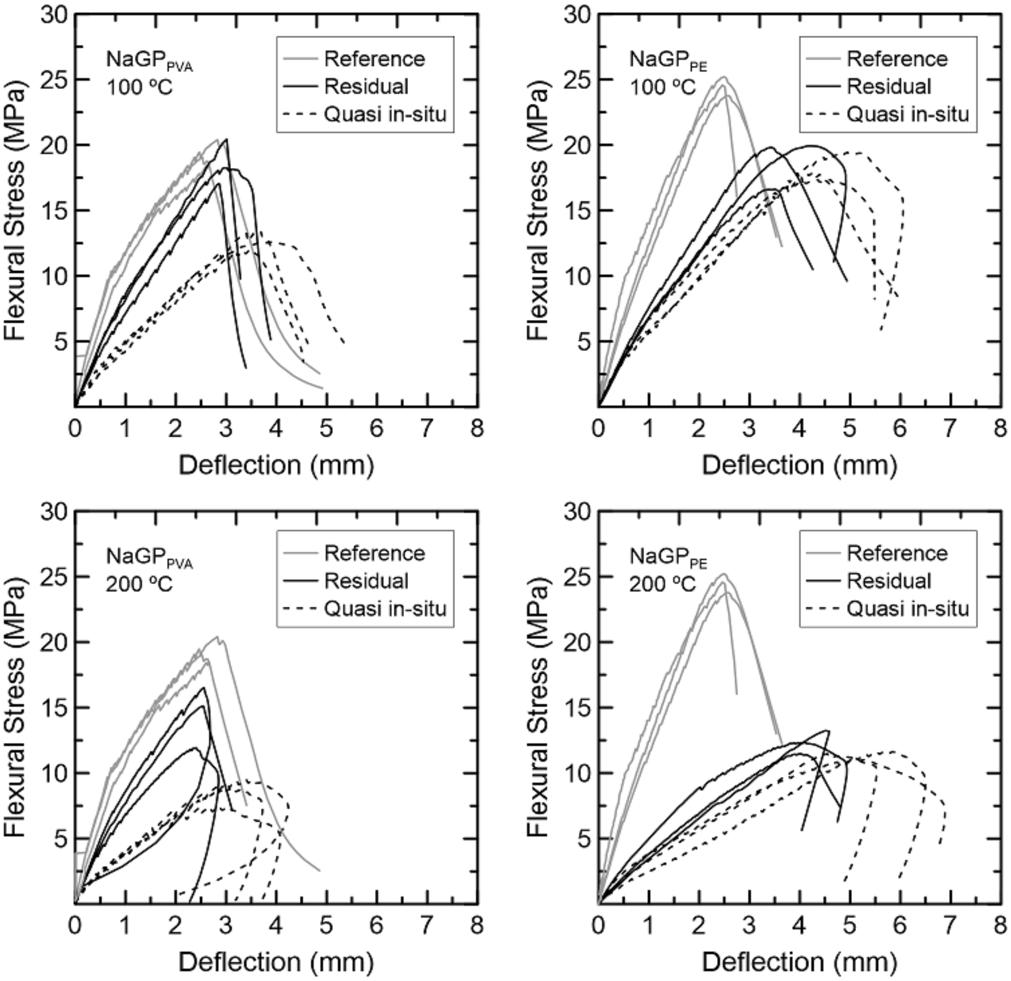

Figure 6.5 – Residual and quasi in-situ flexural behavior of NaGP reinforced with PVA and PE fibers.

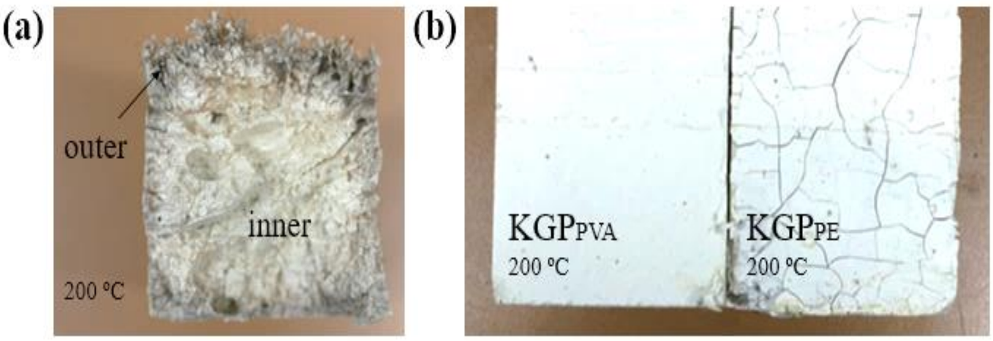

Figure 6.6 – (a) Quasi in-situ tested specimen; and (b) early micro-cracking prior to flexural testing.

Table 6.4 – Results of flexural tests on NaGP-based composites for both various temperature regimes.

Testing temperature	100 °C				200 ºC			
Composite	NaGP$_{PVA}$		NaGP$_{PE}$		NaGP$_{PVA}$		NaGP$_{PE}$	
	R	QIS	R	QIS	R	QIS	R	QIS
First-crack stress [MPa]	7.6 (0.7)	5.1 (0.2)	8.4 (0.5)	4.9 (0.3)	7.0 (0.4)	4.8 (0.3)	-	-
First-crack stress k$_d$	0.79	0.53	0.78	0.45	0.73	0.50	-	-
Flexural strength [MPa]	18.6 (1.5)	12.7 (0.7)	18.8 (1.0)	18.2 (1.2)	14.5 (2.6)	9.6 (0.9)	12.1 (1.2)	10.2 (0.5)
Flexural strength k$_d$	0.94	0.64	0.80	0.77	0.73	0.44	0.51	0.43
Displacement at peak load [mm]	2.7 (0.1)	3.6 (0.3)	3.6 (0.3)	4.5 (0.3)	2.2 (0.2)	3.2 (0.5)	4.2 (0.3)	5.0 (0.3)
Displacement at peak load k$_d$	1.03	1.38	1.44	1.80	0.84	1.23	1.68	2.00
Work-to-fracture [N/mm]	29.6 (3.6)	26.6 (2.2)	38.3 (5.6)	51.8 (7.4)	19.5 (2.5)	15.3 (1.8)	30.2 (2.7)	35.6 (1.9)
Work-to-fracture k$_d$	0.80	0.72	1.05	1.42	0.53	0.42	0.83	0.98
Number of cracks	16 (3)	12 (2)	25 (3)	19 (2)	11 (3)	8 (2)	14 (4)	9 (2)
Number of cracks k$_d$	0.89	0.67	0.78	0.59	0.61	0.44	0.43	0.28
R = residual strength; QIS = quasi in-situ strength; k$_d$ = temperature reduction factor								

When exposed to 200 ºC, both NaGP$_{PVA}$ and NaGP$_{PE}$ demonstrated additional strength losses, reaching merely 14.5 MPa and 12.1 MPa (residual), and 9.6 MPa and 10.2 MPa (quasi in-situ), respectively, with pronouncedly diminished values found for quasi in-situ tested specimens. At 200 ºC the NaGP$_{PE}$ composites yielded a strongly reduced initial stiffness under both regimes, possibly due to early micro-cracking caused by the PE fiber melting and followed longitudinal contraction and radial expansion. Opposed to that, the PVA-based residually tested composites were not significantly affected with regard to stiffness and displacement at peak load. In this sense, it is possible to assume that at this temperature range, composites containing PE fibers had their capacity reduced due to their diminished melting point, displayed in Table 2 (150 ºC [30]), not presenting their regular fibrous form anymore, opposed to a higher PVA limit (240 ºC [38]), allowing a softening to occur at 200 ºC for this reinforcement. This is also confirmed by the reduced crack formation in the composites, which are further confirmed through thermal analysis and ESEM evaluations, in Sections 3.3 and 3.4, respectively. The substantially more pronounced degradation of the PE fibers compared to PVA can be also judged by the insignificant recovery in stiffness and strength of $NaGP_{PE}$ when comparing residual to quasi in-situ tested specimens in Figure 5. On contrary the composites with PVA fibers yielded a considerable recovery of these mechanical features.

Similar comparisons were made for KGP-based composites as shown in Table 6.5 and Figure 6.7, where similar gradual losses in strength were recorded under both regimes up to 200 ºC, with a more evident reduction in mechanical performance at 200 ºC occurring for quasi in-situ tested specimens and those containing PE.

Increases in displacement at peak stress also occurred at both temperatures. When comparing the responses obtained previously for NaGP with the ones found for both KGP composites, it is possible to observe an increased drop in stress at first crack, as also evidenced by the matrix values found in Figure 6.3, suggesting a diminished mechanical capacity of KGP at such temperatures. At 200 ºC, the KGP_{PE} composites yielded a pronouncedly reduced initial stiffness due to melting of the PE fibers, which yielded a significant decrease in strength and stiffness as well as geometry changes. This further result to pronounced micro-cracking when compared to the composites containing PVA fibers (Figure 6.6b). As shown in Table 6.1, PE fibers present greater degradation with temperature rise, in addition to a higher coefficient of thermal radial expansion, when compared to PVA fibers. Thus, it can be assumed that the expansion of this polymeric component embedded in weaker matrices (as is the case of KGP) results in the formation of greater extents of damage by the fiber’s longitudinal contraction and radial expansion, consequently affecting the composites’ mechanical properties. Also, greater flexural strength and stiffness losses occurred for all KGP composites, also affecting the work-to-fracture more evidently when reinforced with PE fibers. This is mainly justified by complete melting of the PE fibers and related shape loss, dramatically limiting the influence of fiber-matrix bond on the mechanical behavior of the composites.

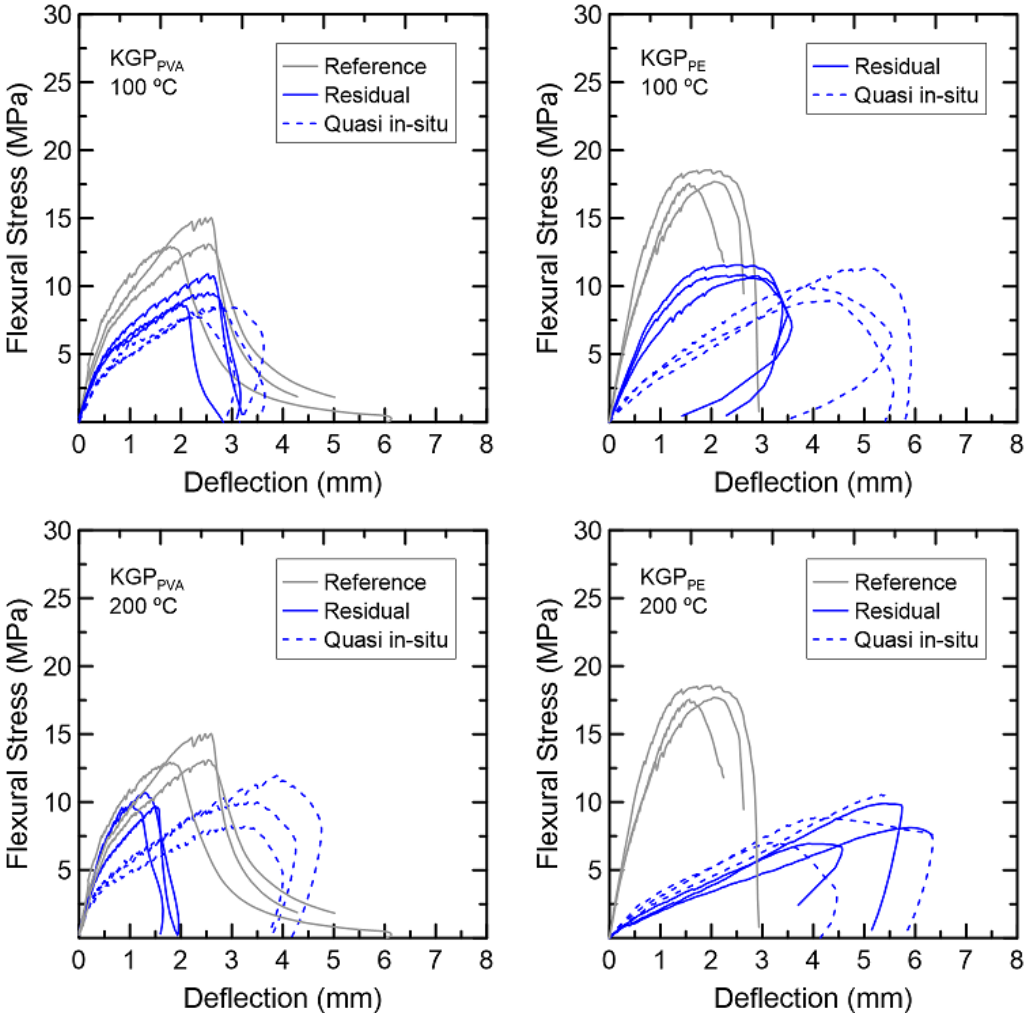

Figure 6.7 – Residual and quasi in-situ flexural behavior of KGP reinforced with PVA and PE.

Table 6.5 – Results of flexural tests on KGP-based composites for various temperature regimes.

Testing temperature	100 °C				200 ºC			
Composite	KGP$_{\text{PVA}}$		KGP$_{\text{PE}}$		KGP$_{\text{PVA}}$		KGP$_{\text{PE}}$	
	R	QIS	R	QIS	R	QIS	R	QIS
First-crack stress [MPa]	5.2 (0.2)	4.7 (0.4)	6.4 (0.2)	5.1 (0.5)	5.5 (0.3)	4.3 (0.1)	-	-
First-crack stress k$_d$	0.70	0.63	0.77	0.61	0.74	0.52	-	-
Flexural strength [MPa]	9.6 (1.5)	8.5 (0.5)	11.9 (0.6)	9.9 (1.1)	9.1 (0.3)	8.1 (1.7)	8.4 (0.5)	8.0 (0.3)
Flexural strength k$_d$	0.70	0.63	0.66	0.55	0.61	0.53	0.46	0.44
Displacement at peak stress[mm]	2.4 (0.3)	2.8 (0.3)	2.8 (0.4)	4.6 (0.5)	1.3 (0.2)	3.6 (0.1)	5.4 (1.0)	4.3 (0.8)
Displacement at peak stress k$_d$	1.00	1.17	1.47	2.42	0.54	1.50	2.84	2.26
Work-to-fracture [N/mm]	16.8 (2.8)	15.7 (1.7)	23.2 (4.4)	29.5 (4.5)	8.2 (1.0)	25.4 (4.1)	26.6 (3.8)	26.0 (5.5)
Work-to-fracture k$_d$	0.74	0.69	1.0	1.27	0.35	1.12	1.14	1.12
Number of cracks	12	11	19	14	9	9	12	8
Number of cracks k$_d$	0.80	0.73	0.76	0.56	0.60	0.60	0.48	0.32
R = residual strength; QIS = quasi in-situ strength; k$_d$ = temperature reduction factor								

6.3.2. Mercury intrusion porosimetry (MIP)

The MIP responses of the plain GPs and SHGC at room temperature and those exposed to 100 ºC and 200 ºC are presented in Figure 6.8 and Table 6.7. Throughout the analysis, the pore sizes are hereby classified into four categories: nanopores (3–10 nm), mesopores (10–50 nm), macropores (50–200 nm), and pores larger than 200 nm, following the methodology adopted by Zhao *et al.* [51], where nanopores are related to the intrinsic geopolymer microstructure, while mesopores are associated to dehydration, and macro and larger pores to the fibers deterioration and microstructural damages. From the curves, the low cumulative porosity of both GP samples is noticeable at room temperature with 16.0% for NaGP and 15.5% for KGP. Moreover, both materials exhibited a predominantly nanoporous structure, due to selective leaching out the tetrahedral layers of the metakaolin source [4,28]. After exposure to elevated temperatures, both NaGP and KGP showed significant increases in specific volume of mesopores and larger pores, associated to dehydration, thus justifying the small reduction in strength found in the previous section (Figure 6.3).

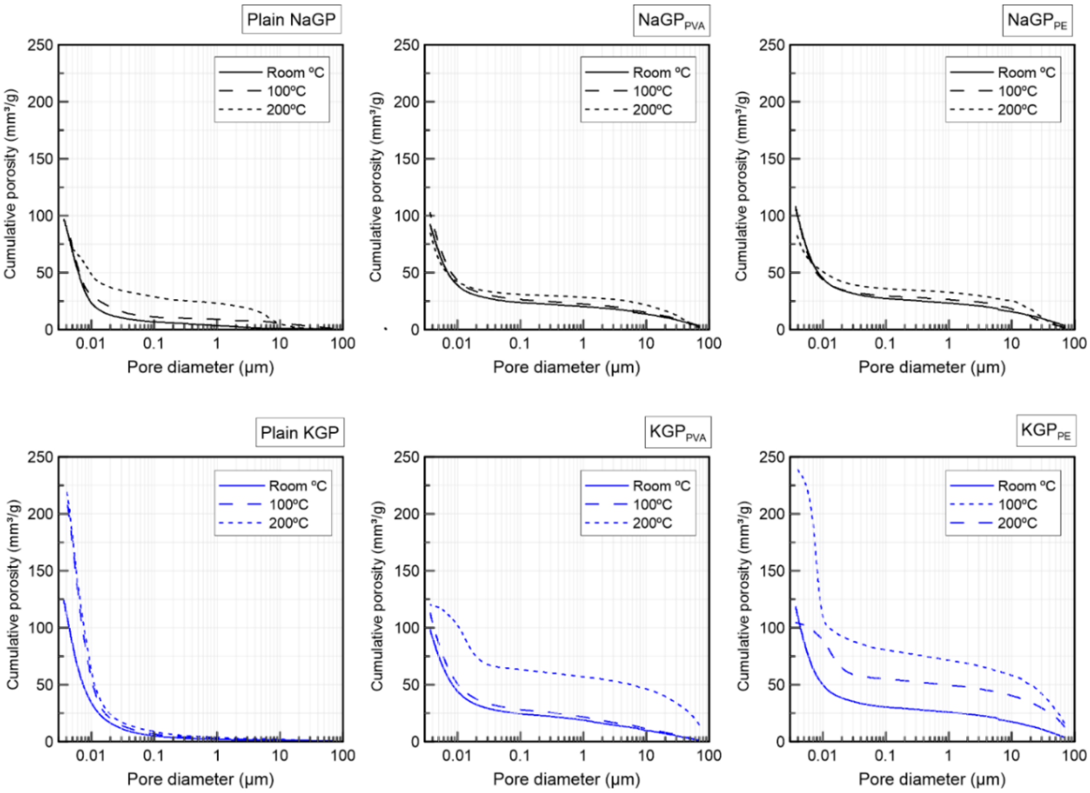

Figure 6.8 – Cumulative porosity of NaGP and KGP plain and reinforced samples (PVA and PE fibers) at room temperature and after exposure to 100 ºC and 200 ºC.

When containing fibers, at room temperature, both matrices presented increases in macroporosity and more significantly in larger pores. For NaGP_{PVA} and NaGP_{PE} larger pores were 4.1% and 5.5% in volume, respectively, while the same variations recorded for KGP were 4.2% and 5.7%. This is due to the higher aspect ratio of the PE filaments [26], leading to more pronounced air entrapment. Also, the greater fluidity of the KGP fresh mix [26] when in contact with a greater number of smaller filaments (in diameter), such as PE, does not create enough friction to properly disperse the fibers, aggravating the processing issues mentioned previously.

Table 6.6 – Results of MIP analysis.

NaGP [vol%]	Plain NaGP			$NaGP_{PVA}$			$NaGP_{PE}$		
	RT	100 ºC	200 ºC	RT	100 ºC	200 ºC	RT	100 ºC	200 ºC
Nanopores (3-10 nm)	12.2	9.4	9.6	8.6	8.2	7.8	8.9	7.8	5.2
Mesopores (10-50 nm)	2.5	4.7	5.8	3.2	4.5	6.0	3.8	5.6	8.2
Macropores (50-200 nm)	0.4	0.5	0.5	0.5	0.6	0.6	0.7	0.7	0.8
Larger pores (>200 nm)	0.9	2.3	2.9	4.1	4.6	4.4	5.5	7.3	8.1
Total porosity [%]	16.0	16.9	18.8	16.4	17.9	18.7	18.9	21.4	22.3
KGP	Plain KGP			KGP_{PVA}			KGP_{PE}		
	RT	100 ºC	200 ºC	RT	100 ºC	200 ºC	RT	100 ºC	200 ºC
Nanopores (3-10 nm)	11.2	7.5	7.1	9.9	8.8	8.1	8.8	7.5	3.2
Mesopores (10-50 nm)	3.3	5.5	5.9	3.2	4.3	7.5	3.4	5.8	8.4
Macropores (50-200 nm)	0.5	0.5	0.4	0.7	0.7	0.8	2.2	0.7	0.8
Larger pores (>200 nm)	0.5	2.1	2.2	4.2	4.4	4.4	5.7	9.6	13.8
Total porosity [%]	15.5	15.6	15.6	18.0	18.2	20.8	20.1	23.6	26.2

After temperature exposure, it was possible to perceive a gradual increment in cumulative porosity, pore size, and more evidently meso-sized porosity, for all composites at 100 ºC and 200 ºC. This effect is assumed to be associated to further H_2O loss and dehydroxylation. However, when incorporating PE fibers, a dramatic change in larger pores content occurred, reaching 8.1% and 13.8%, for both $NaGP_{PE}$ and KGP_{PE}. This behavior is mainly attributed to: (i) melting of the PE fibers when compared to softer, but still in fibrous shape PVA, supported by the ESEM investigations in Figure 12; (ii) a reduced micromechanical capacity of the hardened KGP material, not preventing early micro-cracking, consequently reducing the KGP_{PE} composite's stiffness and strength. Such effects will be further investigated through thermogravimetry and ESEM in the following sections.

6.3.3. Thermal analysis of matrix and fibers

Figure 6.9 presents the TG responses of both NaGP and KGP materials. It is known from previous research [52,53], that within the investigated temperature range the weight loss of hardened GP materials comprises three types of processes during heating: removal of (i) physically bonded water; (ii) chemically bonded water; and (iii) hydroxyl groups. The initial part of the dehydration process (up to 100 ºC) is dominated by the loss of physically bonded water. Thereon, the loss of chemically bonded water dominates up to 250 ºC [53]. It is worth noticing that this type of water may also be referenced as zeolitic water [52,53], since it corresponds to a part of the reaction water generated during polycondensation, thus remaining within the 3D GP framework. The TG curves indicate 17.5% and 12.5% H_2O weight reductions up to 250 ºC, for NaGP and KGP materials, respectively. Hence, for the NaGP matrix a more reacted network can be concluded, explaining also the superior mechanical properties. Note, the occurred water loss processes are also associated with shrinking behavior of the matrices, since they leave empty spaces inside the matrices and increase porosity. The higher increase in porosity for NaGP measured via MIP confirms the pronounced dehydration of the NaGP matrix.

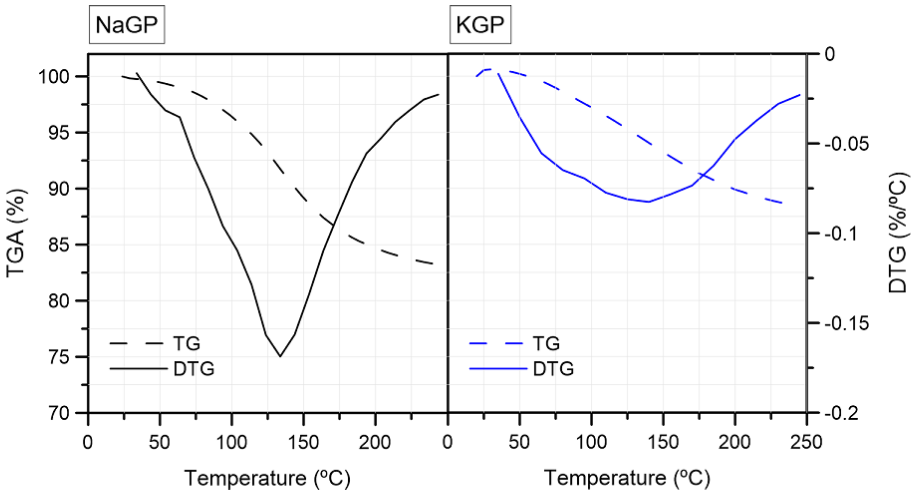

Figure 6.9 – TG curves of plain NaGP and KGP in N_2 environment.

The dilatometry technique was used to further investigate the shrinking behavior of both matrices and corroborate the previous measurements. Figure 6.10 presents the dilatometry curves of the plain NaGP and KGP under investigation.

From the obtained curves it is possible to affirm that the loss of physically bonded water upon reaching 100 ºC did not present any dimensional instability for either matrix. However, with further increase in temperature, significant modifications were recorded, as expected from the chemically bonded water loss, being more visible in the derivative dashed curves. Both samples yielded length variations between 150 and 300 ºC, which is in the same temperature range recorded for the maximum water loss rate in the thermogravimetric analysis. It is worth noting that DTG peaks regarding to maximum weight loss and shrinkage appear clearly earlier than the correspondent dilatometry peaks. This is explained by the significantly different sample sizes and corresponding specimen surfaces. Moreover, the NaGP samples presented clearly a more pronounced increased thermally induced shrinkage behavior, which is in line with the observations made via TGA.

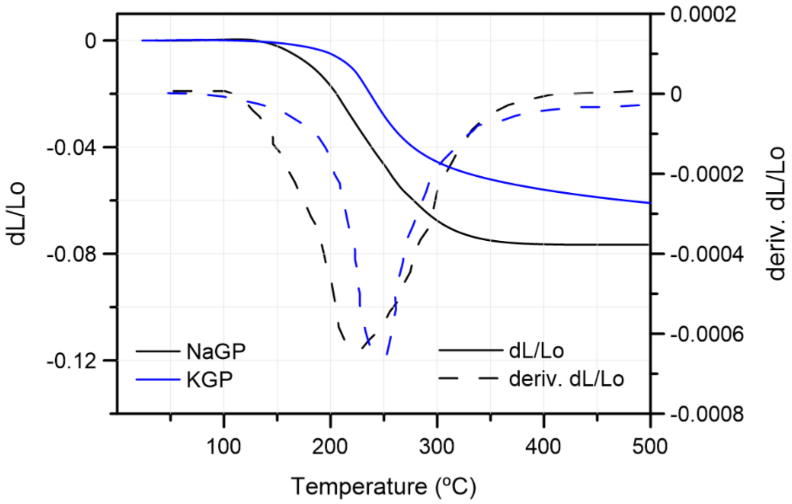

Figure 6.10 – Dilatometer curves of NaGP and KGP plain samples.

The thermal response of the polymeric fibers under TGA analysis is essential to provide insights into the thermomechanical evaluation presented in Section 3.1. Thus, both PVA and PE fibers were exposed to heating processes, and their TGA and DTA responses are presented in Figure 6.11. From the TGA curves it is possible to observe distinctions on both fibers' thermal behaviors, especially regarding onset decomposition temperatures. PE fibers start to decompose around 300 °C with a significant weight loss at 450 °C. In contrast, the PVA fibers start to decompose already between 200 and 250 °C with a significant weight loss around 360 °C. However, thereby also the applied oiling agent need to be considered, since the PVA fiber’s surfaces are coated with an unknown hydrophobic product to reduce their strong chemical bonding to fresh matrices, allowing the occurrence of adequate pullout mechanisms for SHGC [26,30].

DTA provides more insights, in particular to related exo- and endothermal processes. For PE a clear endothermic point occurs already at 160 ºC, representing the melting process of the fibers. The PVA show instead a slight increase at this particular temperature. Whether this is associated to the applied oil coating, as assumed in [37], cannot be clarified here and needs further studies in future. Between 225 °C and 450 °C several slight changes can be observed, which are associated to a partial melting and a decomposition of the PVA fibers. In contrast to that, the PE fibers show a sharper thermal decomposition around 450 °C. Based on both analyses it can be concluded that despite the PVA fibers decompose earlier at higher temperatures, they are more appropriate to use up to 200 °C due to the pronounced melting behavior of the crystalline part in the PE fibers at 160 °C.

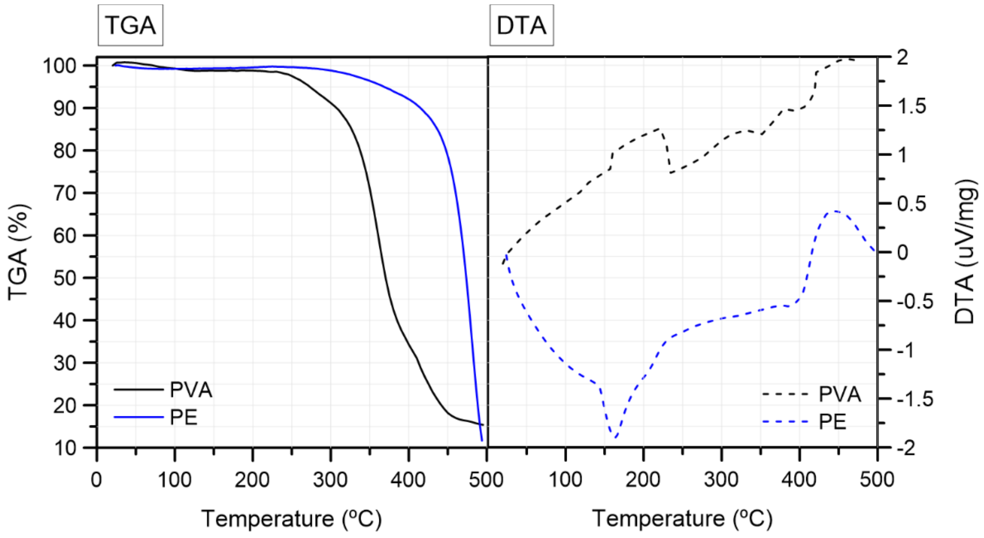

Figure 6.11 – TGA and DTA curves of as-received PVA and PE fibers in a nitrogen environment.

6.3.4. Microscopy analysis

Figure 6.12 presents the ESEM images of the fracture surfaces of NaGP composites reinforced with PVA fibers after their testing under distinct temperature regimes.

The first two images referring to the composites exposed to 100 ºC after cooling (residual) do not show significant degradation of PVA fibers or clear signs of interface issues. This statement is possible due to the existence of empty fiber-shaped channels, and the homogeneous surface of the pulled-out fibers, thus representing an adequate fiber debonding. When exposed to 200 ºC it is possible to distinguish the occurrence of damages to the fibers, such as partial dismemberment of the filaments. Additionally, the quasi in-situ material presents more drastic plastic deformations with a longer debonding length and elongation, which is due to reduced strength and stiffness of fibers at higher temperatures. This behavior is in accordance with the mechanical responses presented in Section 3.1, where all quasi in-situ tested composites resulted in higher values of displacement at peak stress. All NaGP composites demonstrated a predominance of fiber pullout rather than fiber rupture.

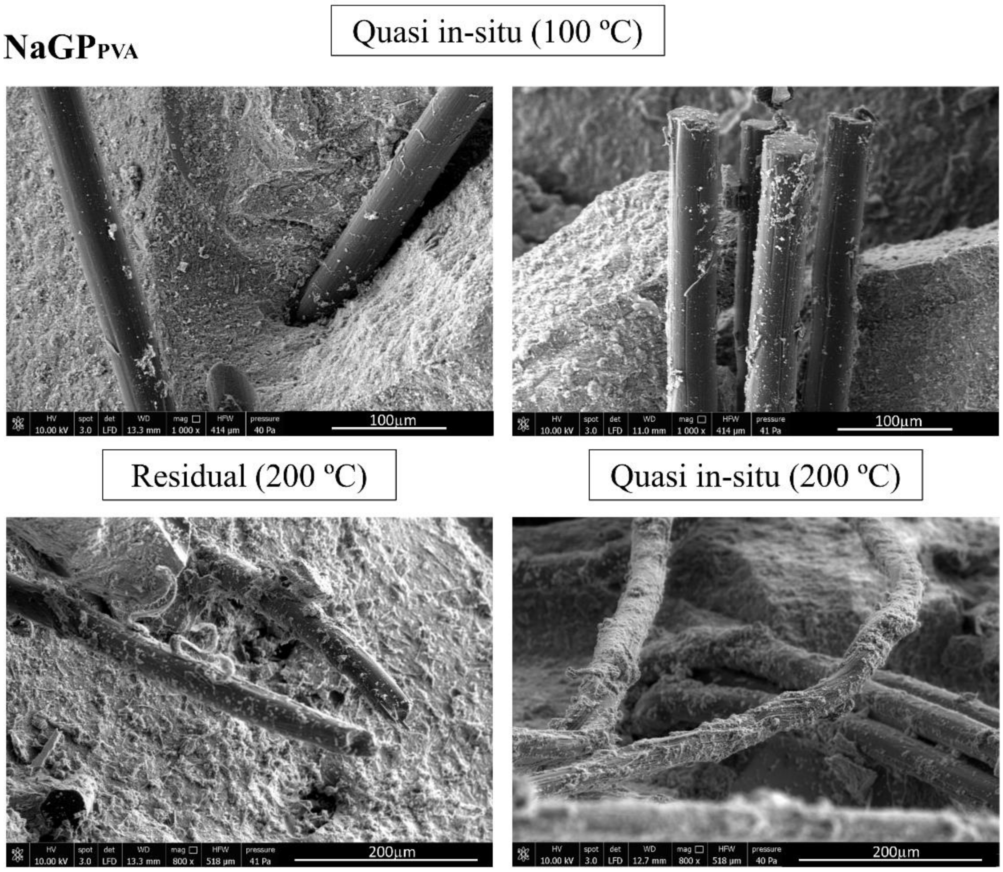

Figure 6.12 – ESEM images of the fracture surfaces of residual and quasi in-situ tested NaGP$_{PVA}$.

Figure 6.13 presents a comparison between the ESEM images of NaGP residual and quasi in-situ composites reinforced with PE after exposure to 200 ºC. It is distinguishable that in both cases the fibers suffered damages characterized by plastic deformations, resulting in shape loss from melting. It can be clearly seen that after melting in the quasi in-situ regime the PE fibers left empty interconnected channels and get clumped as polymeric aggregates. However, a distinct effect can be seen for the residual regime, where not only empty channels and grinded fibers residuals were found, but also fiber rupture occurred as a result of the gradual cooling to room temperature prior to testing. Hence the severely degraded PE fibers present in the matrix cannot ensure a proper crack-bridging action, explaining the reduced mechanical properties of the composites.

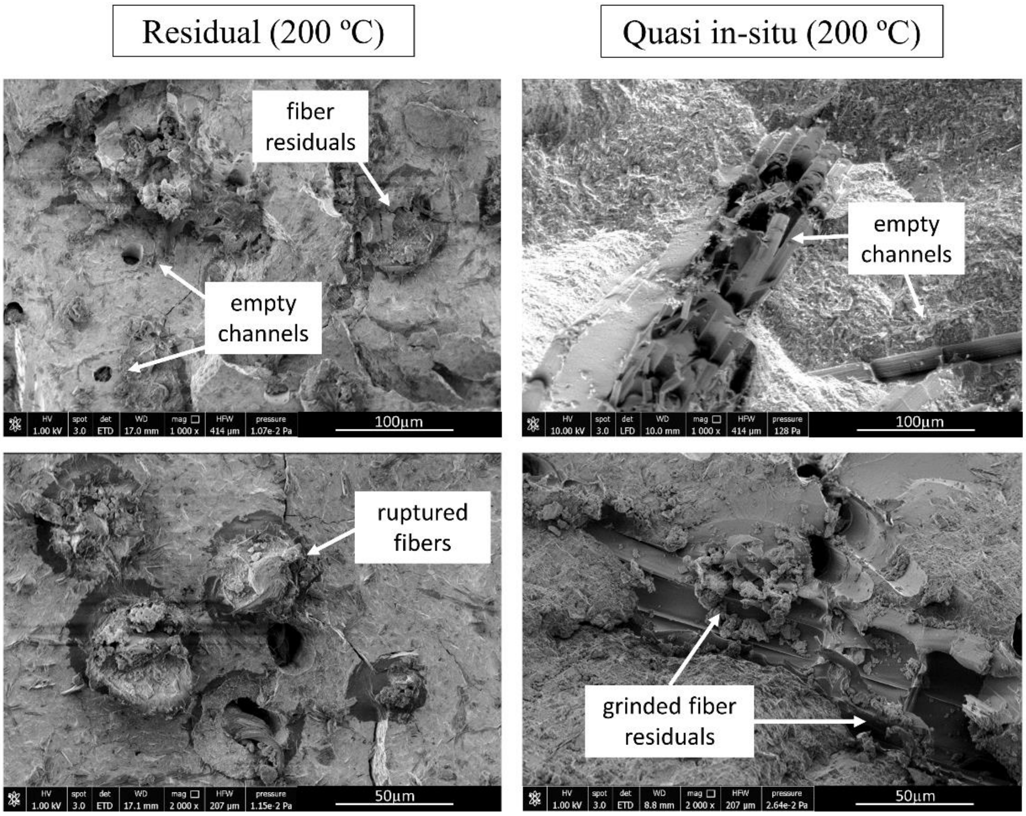

Figure 6.13 – ESEM images of the fracture surfaces of quasi in-situ and residual NaGP$_{PE}$, after exposure to 200 ºC.

Therefore, from the results obtained throughout this study, it can be stated that SHGC reinforced with PVA fibers present advantages in uses up to 200 ºC, due to PVA fibers increased thermomechanical properties, as opposed to the inferior performance of PE. As for the matrix, NaGP demonstrates mechanical superiority and comparable thermal properties to KGP, thus being more suitable for applications that require greater loads. The NaGP with PVA fibers is a material capable of moderately resisting mechanical loading at elevated temperatures, demonstrating apparently superior thermal residual resistance compared to SHCC reinforced and tested in similar conditions, as shown in Figure 6.14 [59,56,57]. As occurs for the SHGC, SHCC do not presents significant modifications on ultimate residual strengths up to 145 ºC, since at this level of exposure the fiber has not suffered major physical damages. The clear distinction related to the diminishment in the multiple cracking behavior seems to be related to the alterations in the fiber-matrix interface due to water loss, in higher extensions than that of the SHGC. In exposures up to 250 ºC, both materials showed increased degradation, despite the SHGC enhanced residual strength and deformability, possibly due to its greater stability at micro and macro levels already stated along this study.

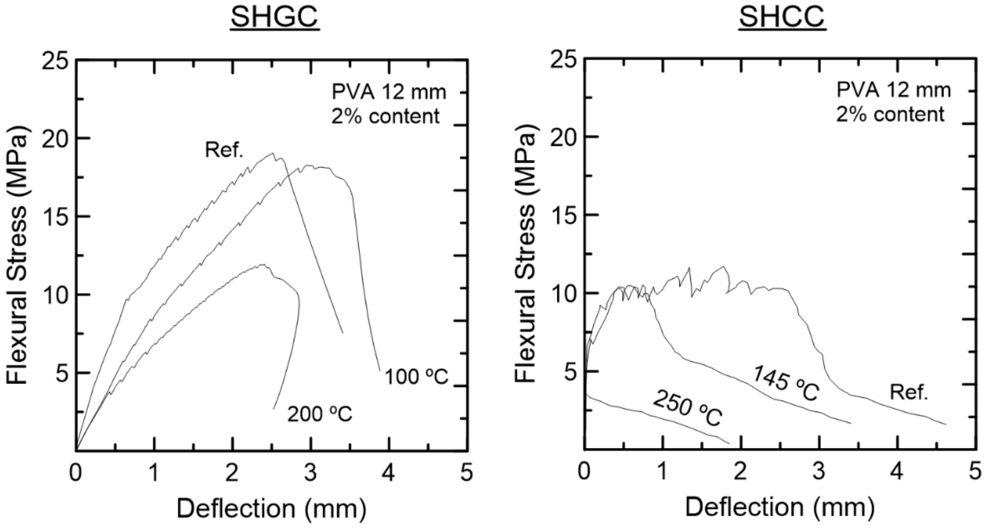

Figure 6.14 – SHGC *versus* SHCC thermomechanical performance [59].

Applications such as protective layers for existing structures exposed to elevated temperatures would be advantageous. A good example would be their use on the repair of specific local areas of massive structures exposed to hot arid regions, possibly combining thermal and dynamic potential, as previously suggested by Trindade *et al.* [45]. SHGC would also be useful in delaying the degradation of structures in the early stages of fire, replacing foam systems, while achieving considerable load-bearing capacity and deformability. Also, safe plugging and permanent abandonment (P&A) in oil wells (up to 200 ºC in 3000 m depth ranges) [41] appear as promising technologies.

6.4. Conclusions

By comparing all the residual and quasi in-situ responses of NaGP and KGP matrices reinforced with PVA and PE fibers, exposed to 100 ºC and 200 ºC, it was possible to conclude the following:

(a) At room temperature the plain samples made of NaGP and KGP matrices presented 9.8 MPa and 7.6 MPa of flexural strength, respectively. When exposed to 100 °C and 200 ºC, reductions of up to 10% and 23% were found for both materials. This was traced back to shrinkage occurrences due water loss and distinct degrees of reactivity, as confirmed by the TG and dilatometry results.

(b) The composites performances at room temperature showed that NaGP_{PVA} and KGP_{PVA} reached flexural strength of 19.7 MPa and 13.7 MPa, while composites containing PE fibers reached the values of 23.5 MPa and 17.9 MPa, respectively. The enhanced flexural strength found for both NaGP variations can be attributed to a higher strength of the NaGP matrix (enhanced reactivity), and to improvements in fiber dispersion and interaction, due to its higher viscosity, enabling higher internal friction to occur during mixing. The use of PE resulted in greater flexural strength due to distinctions in its density, Young's modulus, smaller diameter and mechanical properties.

(c) All composites exhibited strength losses after temperature exposure. This was due to loss of physically and chemically bonded water as well as due to fiber degradation, as evidenced by the TG results. However, greater losses were recorded for quasi in-situ tested specimens, when compared to residual ones. This finding is attributed to the rapid cooling process and to increases in fiber elongation and reduced fiber stiffness when heated, consequently affecting the fiber-matrix interfaces and their work-to-fracture performance. The use of PE fibers was found to be more susceptible to thermal degradation and stiffness losses due to their lower temperature resistance. The KGP_{PE} composite under investigation yielded dramatically reduced initial stiffness at 200 ºC due to early cracking caused by the melting of the fibers, which consequently reduces the load bearing capacity of the composite.

(d) MIP results demonstrated an intrinsic regular nano-porosity for both NaGP and KGP plain samples. After exposure to elevated temperatures, both showed significant increases in mesopores and larger pores, while the incorporation of fibers resulted in a higher amount of macro- and more significantly larger pores.

(e) The ESEM images demonstrated that the PVA fibers did not suffer significant apparent degradation when exposed to a temperature of 100 ºC. Only at 200 ºC it was possible to perceive occurrence of damages, such as partial dismemberment of the filaments. However, PE fibers at 200 ºC left empty interconnected channels and got clumped as polymeric aggregates in the quasi in-situ and residual regimes, respectively, explaining the reduced crack-bridging.

In general, NaGP composites exhibited superior residual and quasi in-situ strength capacities up to 200 ºC when compared to the same KGP variations and traditional cementitious materials (SHCC) under temperature exposures. SHGC materials can be potentially used in applications that may not require outstanding mechanical capacities but may demand stricter safety conditions during elevated temperature exposures, especially in NaGP matrices reinforced by PVA fibers.

6.5. References

[1] Duxson, P., Provis, J.L., Lukey, G.C., Mallicoat, S.W., Kriven, W.M., & Van Deventer, J.S. Understanding the relationship between geopolymer composition, microstructure and mechanical properties. Colloids and Surfaces A: Physicochemical and Engineering Aspects. 269 (2005) (1-3) 47-58. https://doi.org/10.1016/j.colsurfa.2005.06.060

[2] Kriven, W.M., Gordon, M., & Bell, J.L. Geopolymers: nanoparticulate, nanoporous ceramics made under ambient conditions. Microscopy and microanalysis. 10(2004) 404-405. https://doi.org/10.1017/S1431927604886719

[3] Davidovits, J. Years of successes and failures in geopolymer applications. Market trends and potential breakthroughs. In Geopolymer 2002 Conference. Saint-Quentin, France; Melbourne, Australia: Geopolymer Institute. 28(2002) 29.

[4] Davidovits, J. Geopolymers: inorganic polymeric new materials. Journal of Thermal Analysis and calorimetry. 1991; 37(8) 1633-1656. https://doi.org/10.1007/BF01912193

[5] Kriven, W.M., Bell, J.L., Gordon, M. Microstructure and microchemistry of fully-reacted geopolymers and geopolymer matrix composites. Ceramic Transactions. 153(2006) 1994. https://doi.org/10.1002/9781118406892.ch15

[6] Kong, D.L., Sanjayan, J.G., & Sagoe-Crentsil, K. Comparative performance of geopolymers made with metakaolin and fly ash after exposure to elevated temperatures. Cement and concrete research. 37(2007) 1583-1589. https://doi.org/10.1016/j.cemconres.2007.08.021

[7] Duxson, P.S., Mallicoat, S.W., Lukey, G.C., Kriven, W.M., & van Deventer, J.S. The effect of alkali and Si/Al ratio on the development of mechanical properties of metakaolin-based geopolymers. Colloids and Surfaces A: Physicochemical and Engineering Aspects. 292(2007) 8-20. https://doi.org/10.1016/j.colsurfa.2006.05.044

[8] Kriven, W.M., & Bell, J.L. Effect of alkali choice on geopolymer properties. In 28th International Conference on Advanced Ceramics and Composites B: Ceramic Engineering and Science Proceedings. 25(2008) 99-104. https://doi.org/10.1002/9780470291191.ch16

[9] Trindade, A.C.C., de Andrade Silva, F., & Kriven, W.M. Mechanical behavior of K-geopolymers reinforced with silane-coated basalt fibers. Journal of the American Ceramic Society. 104(2021) 437-447. https://doi.org/10.1111/jace.17446

[10] Trindade A.C.C., Alcamand, H.A., Ribeiro Borges, P.H., & de Andrade Silva, F. Influence of elevated temperatures on the mechanical behavior of jute-textile-reinforced geopolymers. Journal of Ceramic Science and Technology. 8(2017) 389-398. https://doi.org/10.4416/jcst2017-00045

[11] Cook, G., & Ponssard, J.P. A proposal for the renewal of sectoral approaches building on the Cement Sustainability Initiative. Climate Policy. 11(2011) 1246-1256. https://doi.org/10.1080/14693062.2011.602552

[12] Duxson, P., Lukey, G.C., & van Deventer, J.S. Thermal evolution of metakaolin geopolymers: Part 1–Physical evolution. Journal of Non-Crystalline Solids. 352(2006) 5541-5555. https://doi.org/10.1016/j.jnoncrysol.2006.09.019

[13] Duxson, P., Lukey, G.C., & van Deventer, J.S. The thermal evolution of metakaolin geopolymers: Part 2–Phase stability and structural development. Journal of Non-Crystalline solids. 353(2007) 2186-2200. https://doi.org/10.1016/j.jnoncrysol.2007.02.050

[14] Barbosa, V.F., & MacKenzie, K.J. Thermal behaviour of inorganic geopolymers and composites derived from sodium polysialate. Materials research bulletin. 38(2003) 319-331. https://doi.org/10.1016/S0025-5408(02)01022-X

[15] Bakharev, T. Thermal behaviour of geopolymers prepared using class F fly ash and elevated temperature curing. Cement and Concrete Research. 36(2006) 1134-1147. https://doi.org/10.1016/j.cemconres.2006.03.022

[16] Zhao, R., & Sanjayan, J.G. Geopolymer and Portland cement concretes in simulated fire. Magazine of Concrete research. 63(2011) 163-173. https://doi.org/10.1680/macr.9.00110

[17] Luna-Galiano, Y., Cornejo, A., Leiva, C., Vilches, L.F., & Fernández-Pereira, C. Properties of fly ash and metakaolín based geopolymer panels under fire resistance tests. Materiales de Construcción, 65(2015) 059. http://dx.doi.org/10.3989/mc.2015.06114

[18] Sakkas, K., Panias, D., Nomikos, P.P., & Sofianos, A.I. Potassium based geopolymer for passive fire protection of concrete tunnels linings. Tunnelling and underground space technology. 43(2014) 148-156. https://doi.org/10.1016/j.tust.2014.05.003

[19] Temuujin, J., Minjigmaa, A., Rickard, W., Lee, M., Williams, I., & Van Riessen, A. Preparation of metakaolin based geopolymer coatings on metal substrates as thermal barriers. Applied clay science. 46(2009) 265-270. https://doi.org/10.1016/j.clay.2009.08.015

[20] Rickard, W.D., Riessen, A.V., & Walls, P. Thermal character of geopolymers synthesized from class F fly ash containing high concentrations of iron and α-quartz. International Journal of Applied Ceramic Technology. 7(2010) 81-88. https://doi.org/10.1111/j.1744-7402.2008.02328.x

[21] Subauer, A., Van Riessen, A. Thermo-mechanical and microstructural characterisation of sodium-poly (sialate-siloxo)(Na-PSS) geopolymers. Journal of Materials Science. 42(2007) 3117-3123. https://doi.org/10.1007/s10853-006-0522-9

[22] Pan, Z., & Sanjayan, J.G. Stress–strain behaviour and abrupt loss of stiffness of geopolymer at elevated temperatures. Cement and Concrete Composites. 32(2010) 657-664. https://doi.org/10.1016/j.cemconcomp.2010.07.010

[23] Sarker, P.K., & Mcbeath, S. Fire endurance of steel reinforced fly ash geopolymer concrete elements. Construction and Building Materials. 90(2015) 91-98. https://doi.org/10.1016/j.conbuildmat.2015.04.054

[24] Lyon, R.E., Balaguru, P.N., Foden, A., Sorathia, U., Davidovits, J., & Davidovics, M. Fire-resistant aluminosilicate composites. Fire and materials. 21(1997) 67-73. https://doi.org/10.1002/(SICI)1099-1018(199703)21:2

[25] Nematollahi, B., Sanjayan, J., Qiu, J., & Yang, E.H. Micromechanics-based investigation of a sustainable ambient temperature cured one-part strain hardening geopolymer composite. Construction and Building Materials. 131 (2017) 552-563. https://doi.org/10.1016/j.conbuildmat.2016.11.117

[26] Trindade, A.C.C., Curosu, I., Liebscher, M., Mechtcherine, V., Silva, F.A. On the mechanical performance of K- and Na-based strain-hardening geopolymer composites (SHGC) reinforced with PVA fibers. Construction and Building Materials. 248 (2020) 118558. https://doi.org/10.1016/j.conbuildmat.2020.118558

[27] Trindade, A.C.C., Heravi, A.A., Curosu, I., Liebscher, M., de Andrade Silva, F., & Mechtcherine, V. Tensile behavior of strain-hardening geopolymer composites (SHGC) under impact loading. Cement and Concrete Composites. 113 (2020) 103703. https://doi.org/10.1016/j.cemconcomp.2020.103703

[28] Curosu, I., Liebscher, M., Mechtcherine, V., Bellmann, C., & Michel, S. Tensile behavior of high-strength strain-hardening cement-based composites (HS-SHCC) made with high-performance polyethylene, aramid and PBO fibers. Cement and Concrete Research. 98(2017) 71-81. https://doi.org/10.1016/j.cemconres.2017.04.004

[29] Curosu, I., Mechtcherine, V., & Millon, O. Effect of fiber properties and matrix composition on the tensile behavior of strain-hardening cement-based composites (SHCCs) subject to impact loading. Cement and Concrete Research. 82(2016) 23-35. https://doi.org/10.1016/j.cemconres.2015.12.008

[30] Magalhães, M.S., Toledo Filho, R.D., & Fairbairn, E.D.M.R. Thermal stability of PVA fiber strain hardening cement-based composites. Construction and Building Materials. 94(2015) 437-447. https://doi.org/10.1016/j.conbuildmat.2015.07.039

[31] Briffaut, M., Benboudjema, F., Torrenti, J.M., & Nahas, G. A thermal active restrained shrinkage ring test to study the early age concrete behaviour of massive structures. Cement and concrete research. 41(2011) 56-63. https://doi.org/10.1016/j.cemconres.2010.09.006

[32] Abdullah, A., Said, I.B., & Ossen, D.R. A sustainable bio-inspired cooling unit for hot arid regions: Integrated evaporative cooling system in wind tower. Applied Thermal Engineering. 161(2019) 114201. https://doi.org/10.1016/j.applthermaleng.2019.114201

[33] Al-Jabri, K.S., Hago, A.W., Al-Nuaimi, A.S., & Al-Saidy, A.H. Concrete blocks for thermal insulation in hot climate. Cement and Concrete Research. 35(2005) 1472-1479. https://doi.org/10.1016/j.cemconres.2004.08.018

[34] Sakkas, K., Sofianos, A., Nomikos, P., & Panias, D. Behaviour of passive fire protection K-geopolymer under successive severe fire incidents. Materials. 8(2015) 6096-6104. https://doi.org/10.3390/ma8095294

[35] da Silva Araujo, R.G., da Silva, F.P.F., de Sena Costa, B.L., Moreira, P.H.S.S., Rodrigues, M.A.F., & de Oliveira Freitas, J.C. Study of cement blend containing rice husk ash for oil well plug and abandonment operations. Construction and Building Materials. 254(2020) 119217. https://doi.org/10.1016/j.conbuildmat.2020.119217

[36] Khalifeh, M., Saasen, A., Vralstad, T., & Hodne, H. Potential utilization of class C fly ash-based geopolymer in oil well cementing operations. Cement and Concrete Composites. 53(2014): 10-17. https://doi.org/10.1016/j.cemconcomp.2014.06.014

[37] Mechtcherine, V., de Andrade Silva, F., Müller, S., Jun, P., & Toledo Filho, R.D. Coupled strain rate and temperature effects on the tensile behavior of strain-hardening cement-based composites (SHCC) with PVA fibers. Cement and Concrete Research. 42(2012) 1417-1427. https://doi.org/10.1016/j.cemconres.2012.08.011

[38] Curosu, I., Liebscher, M., Burk, S., Li, H., Hempel, S., Raak, N., Rohm, H., & Mechtcherine, V. Influence of fiber type on the tensile behavior of high-strength strain-hardening cement-based composites (SHCC) at elevated temperatures. Materials & Design. 198(2020) 109397. https://doi.org/10.1016/j.matdes.2020.109397

[39] Zhang, Z., Liu, J.C., Xu, X., & Yuan, L. Effect of sub-elevated temperature on mechanical properties of ECC with different fly ash contents. Construction and Building Materials. 262(2020) 120096. https://doi.org/10.1016/j.conbuildmat.2020.120096

[40] Liu, J.C., Tan, K.H., & Fan, S. Residual mechanical properties and spalling resistance of strain-hardening cementitious composite with Class C fly ash. Construction and Building Materials. 181 (2018) 253-265. https://doi.org/10.1016/j.conbuildmat.2018.06.009

[41] Liu, J.C., & Tan, K.H. Fire resistance of strain hardening cementitious composite with hybrid PVA and steel fibers. Construction and Building Materials. 135(2017) 600-611. https://doi.org/10.1016/j.conbuildmat.2016.12.204

[42] Sá Ribeiro, R.A., Sá Ribeiro, M.G., Kutyla, G.P., & Kriven, W.M. Amazonian metakaolin reactivity for geopolymer synthesis. Advances in Materials Science and Engineering. 2019(2019). https://doi.org/10.1155/2019/8950764

[43] BSI. 2005. BS EN 196-1: 2005: Methods of testing cement. Determination of strength.

[44] ASTM E831-19, Standard Test Method for Linear Thermal Expansion of Solid Materials by Thermomechanical Analysis, ASTM International, West Conshohocken, PA, 2019, www.astm.org

[45] Curosu, I., Mechtcherine, V., Forni, D., & Cadoni, E. Performance of various strain-hardening cement-based composites (SHCC) subject to uniaxial impact tensile loading. Cement and Concrete Research. 102(2017) 16-28. https://doi.org/10.1016/j.cemconres.2017.08.008

[46] Serafini, R., Dantas, S.R., Salvador, R.P., Agra, R.R., Rambo, D.A., Berto, A.F., & de Figueiredo, A.D. Influence of fire on temperature gradient and physical-mechanical properties of macro-synthetic fiber reinforced concrete for tunnel linings. Construction and Building Materials. 214(2019) 254-268. https://doi.org/10.1016/j.conbuildmat.2019.04.133

[47] He, R., Qu, Z., & Liang, D. Rapid heating thermal shock study of ultra high temperature ceramics using an in situ testing method. Journal of Advanced Ceramics. 6(2017) 279-287. https://doi.org/10.1007/s40145-017-0240-6

[48] de Andrade Silva, F., Butler, M., Hempel, S., Toledo Filho, R.D., & Mechtcherine, V. Effects of elevated temperatures on the interface properties of carbon textile-reinforced concrete. Cement and Concrete Composites. 48(2014) 26-34. https://doi.org/10.1016/j.cemconcomp.2014.01.007

[49] Bhutta, A., Farooq, M., Borges, P.H., & Banthia, N. Influence of fiber inclination angle on bond-slip behavior of different alkali-activated composites

under dynamic and quasi-static loadings. Cement and Concrete Research. 107(2018): 236-246. https://doi.org/10.1016/j.cemconres.2018.02.026

[50] Liu, X., & Yu, W. Evaluation of the tensile properties and thermal stability of ultrahigh-molecular-weight polyethylene fibers. Journal of applied polymer science. 97(2005) 310-315. https://doi.org/10.1002/app.21720

[51] Zhao, J., Liebscher, M., Michel, A., Junger, D., Trindade, A.C.C., de Andrade Silva, F., & Mechtcherine, V. Development and testing of fast curing, mineral-impregnated carbon-fiber (MCF) reinforcements based on metakaolin-made geopolymers. Cement and Concrete Composites. 116(2021) 103898. https://doi.org/10.1016/j.cemconcomp.2020.103898

[52] He, P., Wang, M., Fu, S., Jia, D., Yan, S., Yuan, J., & Zhou, Y. Effects of Si/Al ratio on the structure and properties of metakaolin based geopolymer. Ceramics International. 42(2016) 14416-14422. https://doi.org/10.1016/j.ceramint.2016.06.033

[53] Barbosa, V.F., & MacKenzie, K.J. Thermal behaviour of inorganic geopolymers and composites derived from sodium polysialate. Materials research bulletin. 38(2003) 319-331. https://doi.org/10.1016/S0025-5408(02)01022-X

[54] Gilman, J.W., VanderHart, D.L., & Kashiwagi, T. Thermal Decomposition Chemistry of Poly (Vinyl Alcohol) Char Characterization and Reactions with Bismaleimides. 1995; 161-185.

[55] Liu, X., & Yu, W. Evaluating the thermal stability of high performance fibers by TGA. Journal of applied polymer science. 99(2006) 937-944. https://doi.org/10.1002/app.22305

[56] Huang, H., Wang, R., & Gao, X. Improvement effect of fiber alignment on resistance to elevated temperature of ultra-high performance concrete. Composites Part B: Engineering. 177(2019) 107454. doi:10.1016/j.compositesb.2019.107454

[57] Deshpande, A. A., Kumar, D., & Ranade, R. Influence of high temperatures on the residual mechanical properties of a hybrid fiber-reinforced strain-hardening cementitious composite. Construction and Building Materials. 208(2019) 283-295. 2019. https://doi.org/10.1016/j.conbuildmat.2019.02.129

[58] Deshpande, A. A., Kumar, D., & Ranade, R. Temperature effects on the bond behavior between deformed steel reinforcing bars and hybrid fiber-reinforced strain-hardening cementitious composite. Construction and Building Materials. 233 (2020) 117337. https://doi.org/10.1016/j.conbuildmat.2019.117337

[59] Magalhães, M. S., Toledo Filho, R. D., & Fairbairn, E. M. R. (2011). Thermal properties and resistance to thermal shock of strain hardening cement-based composites. In Proceedings of 2nd International RILEM Conference on SHCC (pp. 189-198).

7 Conclusions and suggestions

7.1. Conclusions

Throughout this study, several evaluations were carried out with geopolymer materials in different combinations. Initially, a literature review was prepared, disseminating the modern geopolymer concepts, pointing out the scientific gaps regarding its use as a composite material, more precisely SHGC-type, with little or no information on its mechanical potential in impact loading and thermal extreme conditions.

For this reason, an initial experimental characterization on varied matrices in their fresh state was conducted, regarding their rheological and thermo-chemo-mechanical properties, being thus used as parameter in the selection of suitable precursors to be incorporated with short polymeric fibers. After that, the quasi-static mechanical characterization of SHGCs reinforced with PVA was presented, varying the alkaline solution (sodium or potassium) and the content of natural aggregates, corroborating its effectiveness through experimental data used in well-known analytical formulations previously established as requirements in literature. Next, a comparative study on the dynamic behavior of such SHGCs reinforced with PVA and PE fibers was carried out, using Hopkinson bars adapted for tensile (in the composite level), and pullout tests (fiber level), pointing out the similarities and advantages when compared to similar traditional Portland cement-based materials (SHCCs). Finally, the residual strength of SHGCs was evaluated under different conditions of exposure to high temperatures, evidencing an enhanced performance of Na-based composites reinforced with PVA fibers up to 200 ºC.

The rheological and thermo-chemo-mechanical evaluation made from various precursor materials showed that the use of high-reactivity metakaolin in pre-established proportions of $SiO_2/Al_2O_3 = 4$, despite demonstrating a slow strength development, showed the most adequate viscosity, with reduced losses of mechanical strength when hardened and exposed to high temperatures, being then used as the main binder in the manufacture of SHGC composites in the following experimental studies.

The quasi-static mechanical evaluations made with SHGCs reinforced with 2% PVA fiber containing high reactivity metakaolin showed a higher effectivity by using sodium as alkaline solution, compared to the use of potassium, reaching higher values in tensile, compression, flexural strength, and Young's moduli. Despite decreasing the workability of both matrices, the use of fine aggregates showed adequate compatibility in 50% by mass of MK, being still possible to easily incorporate the predetermined fiber volume, improving the fiber anchorage in pullout during cracking. The behavior of sodium-based composites and aggregates yielded strain capacities of up to 4.7%, exhibiting crack saturation with widths of only 60 µm and crack spacing of 1.4 mm, showing thus an improved multiple cracking formation compared to traditional SHCC materials, also verified through DIC analysis.

The dynamic evaluation of SHGCs reinforced with PVA and PE fibers at rates of 7.5 m/s resulted in increases in all mechanical parameters when compared to the quasi-static results, with the exception with the deformation capacity. In the case of composites reinforced with PVA fibers, there was a change in the failure mode of the composite, where the fiber is pulled at high rates, instead of being ruptured in the quasi-static mode. $SHGC_{PE}$ did not present changes in their failure mode, being also responsible for the higher values of strength, deformation and work-to-fracture found, due to a better crack bridging performance of this reinforcement. When compared to traditional SHCC responses, $SHGC_{PE}$ did not yield the expected pronounced stress drop after the formation of the first crack in dynamic loading, with subsequent multiple cracking occurring at a considerably higher stress level. This was partly traced back to lower Young’s modulus of the GP matrix and a balanced relationship between the matrix stiffness and crack-bridging action, thus showing a promising path for this material in structural strengthening against dynamic actions.

When exposed to 200 ºC, both sodium and potassium based geopolymer matrices showed mechanical reductions, due to water loss and consequent shrinkage, being more degrading for less viscous matrices such as potassium-based, due to its increased porosity and water loss. Composites reinforced with PVA and PE fibers also showed gradual strength losses in such conditions, being more significant in sudden cooling processes with PE fibers, due to the combination of effects between the volumetric change of the fibers and the loss of stiffness when heated, which in PE case underwent total melting at 200°C, leaving interconnected channels empty in the composite, resulting in larger ductility losses. In comparison, PVA fibers did not undergo apparent degradation at 100°C, with partial damage occurring at 200°C, thus being a safer design under temperature exposure conditions.

In general, this research was successful in manufacturing varied SHGC, reaching suitable stress gain and multiple cracking formation by mixing a high reactivity MK with a Na-based alkaline solution, with polymer short fiber incorporation in 2% by volume. The use of fine aggregates did not present reductions in the SHGC mechanical capacity, being therefore feasible to be handled with both PVA and PE fibers. The latter showed greater effectiveness, mainly due to their low density, achieving hitherto unprecedented results in impact loading, with more stable performance than conventional SHCC. However, the opposite was evidenced through the thermal exposure of these composites, where the use of PVA fibers resulted in greater residual resistance, due to its higher melting point, being more effective up to 200 ºC, thus demonstrating the importance of a comparative investigation to be used as main parameters in designing SHGC to varied applications.

7.2. Suggestions for future works

Although this study has presented novel results regarding the dynamic and thermal potential of SHGC materials, it is evident that, in parallel, it demonstrates new demands for specific investigations that may be explored in future works, such as:

- In the case of geopolymeric matrices, the evaluation of rheological parameters focused on the mixture appears to be necessary, with testing methods and typical theoretical models extensively used for cementitious mixtures, thus creating a parameterized database on chemical variations, possibly being a tool to further tailor the fiber-matrix interface of SHGC composites.
- In the case of geopolymer matrices and possibly composites, triaxial tests coupled with temperature can be performed aiming at applications in oil wells.

- The use of hybrid reinforcements, using carbon fabrics and short fibers, seems to be a promising way to be used as a reinforcement layer in structural elements exposed to dynamic loadings, being potentially beneficial with the use of geopolymer matrices, due to its enhanced performance evidenced in chapter 5.
- To further improve the thermal performance, new fiber replacements such as PBO and ceramic-made fibers could be tested, since they present elevated mechanical and thermal performance.
- And finally, shrinkage and creep behavior seem to be an undiscovered area on the geopolymer composites technology, which still needs to be assessed.